Reconstruction of local and global marine paleoredox conditions for the northeast-Panthalassan (British Columbia, Canada) expression of the Toarcian Oceanic Anoxic Event using a multi-proxy approach

by

Alexandra Kunert

A thesis

presented to the University of Waterloo

in fulfilment of the

thesis requirement for the degree of

Master of Science

in

Earth Sciences

Waterloo, Ontario, Canada, 2020

Author’s Declaration

I hereby declare that I am the sole author of this thesis. This is a true copy of the thesis, including any required final revisions, as accepted by my examiners.

I understand that my thesis may be made electronically available to the public.

Statement of Contributions

The content of this thesis is my own work. Preliminary data (2018 sample set XRD, major & some trace elements, and carbon content) from this thesis was published in a Summary of Activities technical paper for Geoscience British Columbia (Kunert, et al., 2019) with my supervisor Dr. Brian Kendall, and collaborators at Petronas Canada (Dr. Tom Moslow, Gerry Nyberg, Bernadette Pedersen) and Sasol Canada (Craig Smith). No portion of the technical paper has been used in the writing of this thesis.

Abstract

The Toarcian Oceanic Anoxic Event (T-OAE) of the Early Jurassic is one of several Mesozoic instances of expanded ocean anoxia, coupled with feedbacks and perturbations in Earth's systems. The drivers for these feedbacks are debated, but the general consensus is that the event is initially rooted in the emplacement of the Karoo–Ferrar large igneous province. The T-OAE is also linked to a second-order mass extinction in the marine and terrestrial realms. Study of the T-OAE aims to provide insight into the causes and consequences of the environmental changes, which may be applicable at present given that some of the characteristics of the T-OAE (e.g. carbon inputs leading to global warming) are reflected in the modern environment. The purpose of this study, which focused on an Early Jurassic section containing the T-OAE in northeastern British Columbia, was to provide extensive insight into the local depositional environment, as well as a glimpse at the global ocean paleoredox conditions across the duration of the event.

In northeastern British Columbia, the Early Jurassic is divided into the Gordondale Member and Poker Chip Shale of the lower Fernie Formation. The studied drill core contains both members; the Gordondale is the basal member composed of organic-rich, calcareous mudstone, whereas the overlying Poker Chip shale is a siliceous mudstone to siltstone unit. To provide context for the T-OAE in the study core, organic carbon isotope compositions were profiled in search of a telltale negative carbon isotope excursion (N-CIE) which signals the event zenith. The event was identified by an N-CIE in the uppermost 7 meters of the Gordondale Member below the contact with the Poker Chip Shale.

Local paleoenvironmental reconstruction was accomplished using elemental redox sensitive trace metal geochemistry to determine the redox regimes (oxic, suboxic, anoxic or euxinic) and hydrography (open versus restricted) of the depositional basin. The Gordondale Member was characterised as anoxic to euxinic. Elevated Mo and V (up to 370 µg/g and 2757 µg/g, respectively) suggested some intervals were deposited in an euxinic environment. The U and Re concentrations are also elevated in the euxinic intervals (up to 36 µg/g and 878 ng/g, respectively). Intervals with lower Mo and V concentrations (< 53 µg/g and < 289 µg/g, respectively) but elevated U and Re content (up to 33 µg/g and 287 ng/g, respectively) indicated anoxic (non-sulfidic) conditions. The Poker Chip Shale was characterised by suboxic

conditions (moderate Mo, V, U, and Re concentrations; < 21 µg/g, < 248 µg/g, < 6.3 µg/g, 86 ng/g, respectively). The cored interval was characterised as having been deposited in an open marine upwelling zone environment. This interpretation is based on an Mo–U covariation trend similar to the modern North and South American Pacific coastal basins (e.g. California, Mexico, Peru), and a Cd–Mo covariation trend indicating substantial primary productivity as a result of upwelling nutrient-rich deep waters.

The T-OAE was a period where seafloor anoxia and/or euxinia is thought to have expanded across the global oceans. An estimate of the global area of seafloor anoxia and euxinia can be obtained from recently-developed mass balance models for elemental Re and Mo. Samples deemed anoxic (enrichment factors of U > 3.6 and Re > 100) or euxinic (anoxic, and enrichment factor of V > 3, S/Fe > 1.15) were grouped stratigraphically by those which occurred before the N-CIE ("Pre-N-CIE"), and during the N-CIE (two groups, "lower N-CIE" and "upper N-CIE"). The results of the mass balance model illustrated an expansion of anoxic and euxinic seafloor areas at the onset of the N-CIE (Pre-N-CIE to lower N-CIE) from ~1% to 6% of the total seafloor area. This was followed by a contraction of the anoxic and euxinic seafloor areas from ~6% to 4% of the total seafloor area from the lower to upper portion of the N-CIE.

An attempt to link the expansion of anoxic and euxinic seafloor areas to Karoo–Ferrar large igneous province activity was made using a sedimentary Hg proxy. Previous study indicated that the utility of the proxy may decrease with increasingly distal (deeper waters, farther offshore) marine deposition. No distinctive Hg signature was associated with the N-CIE in the study core. As the study core was interpreted as having been deposited in a deep water/offshore environment, the lack of a Hg signal for volcanic activity was possibly affected by distal deposition. Thus, no conclusions were drawn from sedimentary evidence of enhanced volcanic activity.

While no direct link to the Karoo–Ferrar province was made within the core, the mass balance models suggest that the T-OAE was indeed a period of expanded anoxic/euxinic seafloor area, at least in part. The maximum 6% total seafloor area covered by anoxia/euxinia was most likely located along the continental margins, thus the deep waters of the abyssal plains and central ocean likely remained oxygenated. These findings have demonstrated that

the T-OAE was a minor event relative to the well-known “Big 5” mass extinctions, yet it was still associated with biodiversity loss. By monitoring modern anoxic/euxinic seafloor area, it may become possible to track the changes in Earth’s systems through comparison with these ancient OAE events.

Acknowledgements

This project was supported by a Mitacs Accelerate Internship and partner organisations, Petronas Canada and Sasol Canada. Through the collaboration, I received enthusiastic support from Gerry Nyberg, Bernadette Pedersen, Dr. Tom Moslow, Wayne Hovdebo, Audrey Whitlock and Stav Michailides at Petronas, and Craig Smith at Sasol.

While in Calgary for the 2 two-month Mitacs internships, not only did I get to sit in a very luxurious cubicle at Petronas (with a panoramic view of the Rockies), I also got to play with my rocks (i.e. "the study core") at Weatherford Labs and the AER Core Research Facility. I want to thank Jing Chen at Weatherford for her hospitality and providing me with all the tools necessary to perform my work (including a fresh-baked plate of chocolate chip cookies).

Geoscience BC supported this project through their Geoscience BC Graduate Scholarship program. This ensured the publication of a technical report (Kunert, et al., 2019) in their annual *Summary of Activities: Water and Energy*, and presentation of early results at GeoConvention 2019 in Calgary.

Technical support for carbon isotopes was provided by Bill Marks at the EIL, who helped me out with sample prep and analysed the samples. Dr. Teddy Them at the GAMES Lab is also thanked for his analysis of sediment mercury to enable comparison with outcrop and core he previously studied on the Alberta side of the basin.

NSERC Discovery Grants to my supervisor Dr. Brian Kendall (RGPIN-2013-435930 and RGPIN-2019-04090), and funding from the Canada Foundation for Innovation and the Ontario Research Fund supported activities at the Metal Isotope Geochemistry Lab, and travel to conferences.

My committee members, Drs. Chris Yakymchuk and Thai Phan, are thanked for their time and input on my research. I always appreciate critical feedback on my work and was given great advice and suggestions for improvement.

Dr. Jen Parks is thanked for guiding me into more involved teaching roles in the petrography lab, and for her curiosity surrounding my project.

I want to profoundly thank my supervisor, Brian, for his unwavering support through the project, both technically and personally. I am grateful that he saw a bit of potential in me when we first worked together on my Honours thesis. His discussions always provide clarity on aspects of trace metal redox geochemistry, the world of academia, and they often helped to steer me towards (or away from) some of the ideas that popped into my head during the project. I know that clicking with a supervisor does not happen for every grad student, so I appreciate how fortunate I am to work with Brian. I look forward to continuing as his PhD student, and undoubtedly in future collaborations.

Finally, to my parents and little sister, Micheal, Debbie and Emma: thank you for supporting me always, in whatever I choose to pursue.

Table of Contents

List of Figures

List of Tables

List of Abbreviations

AFL	Agriculture and Food Laboratory (University of Guelph)
CCD	Carbonate compensation depth
CIE	Carbon isotope excursion
C_{inorg}	Inorganic carbon
C_{org}	Organic carbon
C_{tot}	Total carbon
DF	Dilution factor
EIL	Environmental Isotope Laboratory (UW)
Fm	Formation
g	Grams
GAMES	Geochemistry of Ancient and Modern Environmental Systems Laboratory (College of Charleston)
HCl	Hydrochloric acid
HF	Hydrofluoric acid
HNO_3	Nitric acid
HREE	Heavy rare earth elements
HRL	Hard Rock Laboratory (UW)
LDPE	Low-density polyethylene
LREE	Light rare earth elements
Ma	Million years ago (age)
Mb	Member
µg/g	Micrograms per gram (ppm w/w)
MIGL	Metal Isotope Geochemistry Laboratory (UW)

ml	Millilitres
Myr	Million years (value)
N-CIE	Negative carbon isotope excursion
ng/g	Nanograms per gram (ppb w/w)
OAE	Oceanic Anoxic Event
P-CIE	Positive carbon isotope excursion
PCS	Poker Chip Shale
PDB	PeeDee Belemnite standard
Pl–To	Pliensbachian–Toarcian (ref. to boundary)
ppb	Parts-per-billion
ppm	Parts-per-million
QQQ-ICP-MS	Triple-quadrupole inductively-coupled plasma mass spectrometer
REE	Rare earth elements
RSD	Relative standard deviation
SBC-1	USGS Brush Creek Shale standard
SD, s	Sample standard deviation (also ‘σ’, if cited from literature)
SDO-1	USGS Devonian Ohio Shale standard
SGR-1b	USGS Green River Shale standard
T-OAE	Toarcian OAE
USGS	United States Geological Survey
UW	University of Waterloo
WCSB	Western Canada Sedimentary Basin
wt%	Weight percent
XRD	X-ray diffraction

List of Symbols

A_i	Seafloor area of a given sink, *i* (% total area)
b_i	Trace metal burial rate of a given sink area, *i* (g cm^{-2} yr^{-1})
BMAR	Bulk mass accumulation rate (g cm^{-2} yr^{-1})
C_c	Certified standard concentrations (wt%, µg/g, ng/g)
C_f	Final, converted element concentrations (wt%, µg/g)
C_m	Measured element concentrations (ng/g)
C_t	True element concentrations (ng/g)
DF_d	Desired dilution factor
DF_t	True dilution factor
E	Element atomic mass (g/mol)
F_{in}	Input flux (mol/yr)
m_a	Aliquot mass (g)
m_f	Analyte solution mass (g)
m_s	Stock solution mass (g)
m_{wr}	Whole rock sample mass (g)
Δt	Duration (yr)
V_a	Estimated aliquot volume (ml)
$\overline{x}$	Mean
Δz	Vertical interval length (cm)
ρ_b	Bulk density (g cm^{-3})

1. Introduction

Transient episodes of expanded ocean anoxia (low to no oxygen) are observed in the Phanerozoic geological record as coeval, globally distributed organic-rich black shales (Sageman, 2009). Major Mesozoic instances of these conditions, termed "Oceanic Anoxic Events" (OAEs), are distinguished by high organic carbon (C_{org}) content, organic and inorganic carbon isotope excursions (CIEs), and enrichments of redox-sensitive trace metals in black shales (Jenkyns, 2010). Further study of OAEs is necessary to understand major changes in Earth's climate, ocean and biological systems through time; many are accompanied by mass extinctions that decimated marine and/or terrestrial life (Pálfy & Smith, 2000). Current anthropogenic activities may be contributing to similar changes in these Earth systems, including a rise in atmospheric and ocean temperatures, ocean acidification, ocean deoxygenation, and aquatic nutrient loading (Breitburg, et al., 2018). Some of the scientific community postulates that these changes are leading to an Anthropocene extinction event (e.g. Keller, et al., 2018; Bacon & Swindles, 2016; Ceballos, et al., 2015), which may have similar features to past OAEs.

Early Jurassic rocks host the globally-identified Toarcian OAE (T-OAE). The T-OAE is identified over an estimated 300 to 500 kyr period (Sell, et al., 2014; Boulila, et al., 2014) in Early Jurassic organic-rich black shales by negative CIEs (N-CIEs) in inorganic (up to –4‰ from baseline values; e.g. Hesselbo, et al., 2000) and organic (–4 to –8‰ from baseline values; e.g. Them II, et al., 2017a) carbon fractions, embedded within a broader positive CIE (P-CIE). Input of isotopically-light carbon (^{12}C) causes the negative excursion in the carbon isotope signature ($\delta^{13}C$), and may be a result of one or all of the following mechanisms: methane hydrate destabilization and injection into the shallow ocean–atmosphere system (Hesselbo, et al., 2007), volcanic emissions (Kuroda, et al., 2007), thermogenic methane release during igneous intrusions interacting with coal or black shales (McElwain, et al., 2005), recycling of dissolved inorganic carbon from bottom waters to the upper water column during upwelling or seasonal overturn ('Küspert Model'; van de Schootbrugge, et al., 2005), or continental weathering of organic-rich soils and rocks (Higgins & Schrag, 2006). The P-CIE is driven by high primary productivity levels and subsequent organic carbon burial. The T-OAE was

accompanied by a marine extinction (5% fossil family loss) and continental extinction (2-12% fossil family loss) (Pálfy & Smith, 2000).

To fulfil the definition of an OAE, the event must have occurred globally. Much evidence of the T-OAE is found in Europe (e.g. United Kingdom, Germany, Italy, Switzerland, Portugal) where Jurassic outcrop and subsurface sections are present and preserved (Jenkyns, 2010). The European sections represent deposition along the margins of the Tethys sea (precursor to Atlantic and Indian oceans), thus sections from the Panthalassa (Proto-Pacific) ocean must also contain the T-OAE (N-CIE) for the event to be classified as an OAE (**Figure 1**). The N-CIE has been documented in Panthalassan sections from Japan (Gröcke, et al., 2011), Canada (Them, et al., 2017a; Caruthers, et al., 2011), Argentina (Al-Suwaidi, et al., 2010) and Chile (Fantasia, et al., 2018).

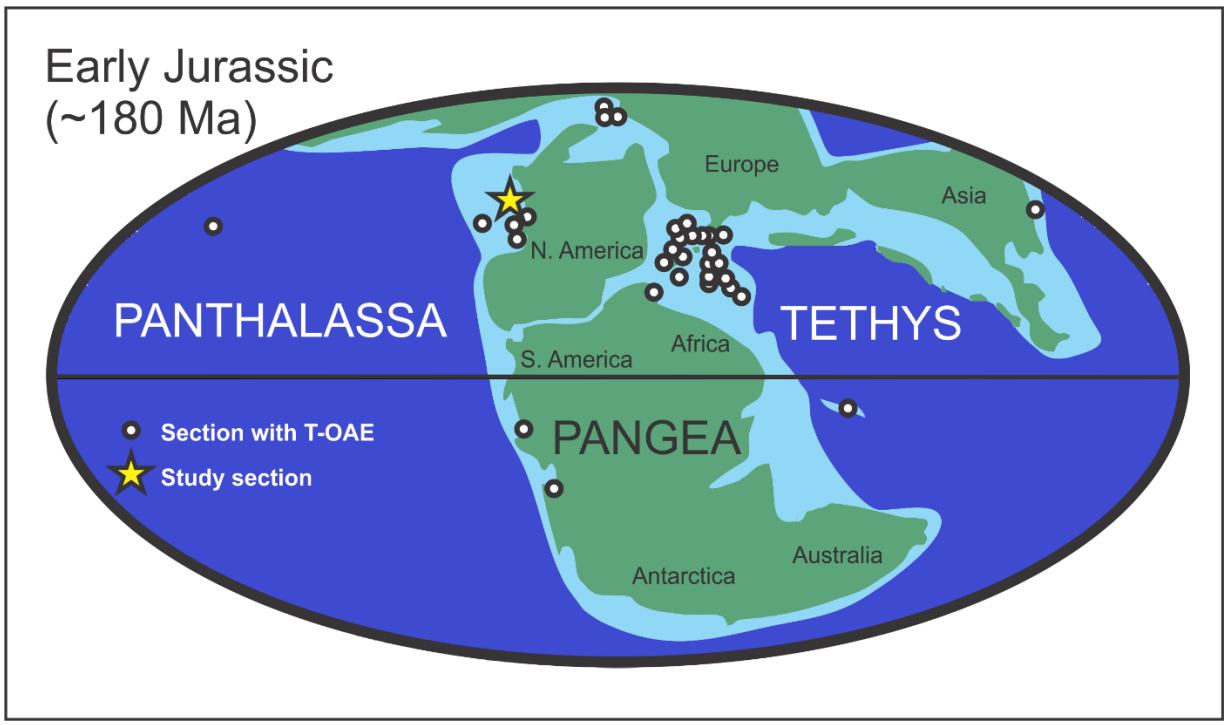

Figure 1. **Global Early Jurassic paleogeography and locations with the T-OAE identified.** The T-OAE has been identified in sections by a negative carbon isotope excursion (CIE) embedded within a positive CIE (white dots). The study section (yellow star) is located in British Columbia and was deposited on the northeast margin of Panthalassa (Proto-Pacific). Modified from Them et al. (2017a).

The Early Jurassic in North America is relatively unexplored with respect to the T-OAE, with the N-CIE identified in three Alberta sections (Them II, et al., 2019; Them II, et al., 2017a; Them II, 2016) and one coastal British Columbian (Haida Gwaii) section (Them II, et

al., 2017a; Caruthers, et al., 2011). In the Western Canada Sedimentary Basin (WCSB), the Early Jurassic is represented by the lower Fernie Formation; in northeastern British Columbia (NEBC) this includes the organic-rich black shales of the Gordondale Member and Poker Chip Shale (PCS). This study includes $\delta^{13}C_{org}$ signatures of the Gordondale Member and PCS from a drill core located 75 km west of Fort St. John, NEBC to confirm the presence of the N-CIE and allow for further examination of the T-OAE in the North American context.

With the T-OAE identified in the core, major element, redox-sensitive trace metal and carbon geochemistry were employed to observe depositional conditions and changes before, during, and after the event. Mercury (Hg) and sulfur (S) analysis were conducted to establish a possible link to volcanism (i.e. emplacement of the Karoo–Ferrar large igneous province and related activity; Pálfy & Smith, 2000) as the initial driver of the T-OAE. It has recently been demonstrated that with increasingly distal marine deposition, the Hg paleoproxy may be less effective (Them II, et al., 2019). Because the study core is more distal than the sections studied in Them II et al. (2019), a comparison can be made to confirm this trend. Rock-Eval pyrolysis provides kerogen type and thermal maturity—parameters for organic matter source (marine or terrestrial) and extent of post-depositional processes (e.g. diagenesis, burial, hydrocarbon production). X-ray diffraction depicts mineralogical trends, with implications for paleolatitude and detrital input (e.g. carbonate versus siliciclastic deposition). Major and minor element and redox-sensitive trace metal concentrations and covariations are used to identify local paleoredox (e.g. Mo, Re, V, U, Re/Mo) and paleohydrographic (e.g. Mo/U, Cd/Mo) conditions. If the depositional basin was open to water mass exchange with the global ocean, and reducing conditions are indicated through local redox proxy analysis (e.g. anoxia or euxinia by elevated Re or Mo concentrations, respectively) the cored section is a valid candidate to investigate global paleo-ocean conditions. This combination of redox-sensitive geochemical analyses has yet to be performed on any of the North American T-OAE sections.

Recently developed mass balance models for rhenium (Re) and molybdenum (Mo) are used to approximate the relative area of ancient global seafloor covered by anoxic or euxinic conditions, respectively (Sheen, et al., 2018; Reinhard, et al., 2013). Mass balance models are used for the T-OAE section in the core to provide an estimated area of bottom water anoxia and euxinia before and during the event. Because these models were developed to observe long-term temporal changes in anoxia and/or euxinia (through the entire geological record),

rather than short temporal scales as discussed in the context of the T-OAE, the models are adjusted to the best-estimated local and temporal conditions. Other estimates of global seafloor anoxia and/or euxinia over the T-OAE have been made using stable Tl and Mo isotopes (Them II, et al., 2018; Pearce, et al., 2008), but the elemental Mo and Re mass balance models have not been applied to the T-OAE. The expansion of anoxic and/or euxinic bottom waters may have exacerbated changes to the climate system and/or promoted large-scale die-off of marine species. By quantifying the expansion, we can learn how even minor changes may affect the modern marine environment.

1.1. Study Objectives

This thesis is centred around two main objectives, and several subobjectives, which combine geochemical results obtained from the study core samples:

(1) Characterise the local depositional environment over the period covered in the core;
   (1.1) Determine bottom-water paleoredox conditions using redox-sensitive trace metal concentrations and ratios;
   (1.2) Identify the paleohydrographic regime using Mo–U and Cd–Mo covariation diagrams, and answer the following questions:
      (1.2.1) Was the basin connected to, or restricted from global ocean water mass exchange?
      (1.2.2) Were organic-richness and trace metal enrichment controlled by enhanced productivity in an open ocean upwelling zone, or by enhanced preservation in a restricted, highly anoxic basin?

(2) If the findings from subobjective 1.1 show deposition under anoxic/euxinic bottom-waters, and subobjective 1.2 implies open ocean conditions, then an estimation of the area of anoxic/euxinic seafloor will be attempted using Re and Mo mass balance models. This will answer the following questions regarding the T-OAE:
   (2.1) What was the extent of anoxic/euxinic seafloor expansion?
   (2.2) Did euxinic conditions prevail over non-sulfidic (ferruginous) conditions?
   (2.3) Within the T-OAE itself, was there an expansion, contraction or no change in the area of seafloor anoxia/euxinia?

From the completion of these objectives, a greater understanding of the temporal and spatial extent of anoxia and/or euxinia through the T-OAE will be accomplished. Additionally, because the study core is a new section containing the T-OAE in an underrepresented area (North America; versus Europe) the geochemical analyses and findings will allow for further verification of the T-OAE's global nature. This will also allow for direct comparison to the sections studied in Alberta (Them II, et al., 2019; 2018; 2017b; 2017a).

2. Oceanic Anoxic Events

2.1. Oceanic Anoxic Events

Schlanger and Jenkyns (1976) first proposed the term “Oceanic Anoxic Events” (OAEs) to describe coeval, globally-distributed Cretaceous marine black shales. The term has since been extended to include multiple events through the Mesozoic stratigraphic record. Schlanger and Jenkyns (1976) suggested that an increase in the area of warm, shallow marine environments led to an increase in primary productivity and thus export of organic matter to bottom waters. As organic matter respiration and decomposition depletes the oxygen supply, bottom waters become more anoxic allowing preservation of organic matter to become more efficient. Therefore, a large quantity of organic matter is preserved in a laterally and vertically expansive oxygen-minimum zone from ocean depths ranging from less than 300 m to over 1200 m.

Strata deposited during OAEs share many similar geochemical characteristics. Typically, these strata are organic-rich, exhibit carbon isotope excursions (CIEs), and have high phosphorus (P) content at their onset which indicate enhanced burial and/or preservation of organic matter (Jenkyns, 2010). Additionally, redox-sensitive trace metal enrichments, shifts to lighter Mo and heavier thallium (Tl) isotope signatures, and photic zone sulfur-reducing bacteria biomarker signatures reflect expanded bottom-water anoxia and/or euxinia (Them II, et al., 2018; Jenkyns, 2010; Cohen, et al., 2008). Oxygen isotope minimums and Mg/Ca ratio maximums in bulk carbonates imply temperature increases and/or greenhouse-Earth periods (Jenkyns, 2010). Strontium (Sr), osmium (Os) and calcium (Ca) isotope signatures also reveal an increase in continental weathering leading up to, or during many OAEs (Them II, et al., 2017b; Brazier, et al., 2015; Jenkyns, 2010; Jones & Jenkyns, 2001).

Several OAEs have been identified, the most prominent events being the Toarcian (T-OAE; Posidonienschiefer Event; Early Jurassic), Early Aptian (OAE 1a; Selli Event; Early Cretaceous), and the Cenomanian–Turonian (C/T OAE or OAE 2; Bonarelli Event; Late Cretaceous) (Jenkyns, 2010). Less significant OAEs include the Late Valanginian Weissert Event, Late Hauterivian Faraoni Event, Early Albian Paquier Event (OAE 1b), Late Albian

Breistroffer Event (OAE 1d), Coniacian–Santonian Event (OAE 3) of the Cretaceous, and the Paleocene–Eocene Thermal Maximum (PETM) of the Paleogene (Jenkyns, 2010).

2.2. Potential Triggers of OAEs

The main drivers increasing global anoxic bottom waters during OAEs may include climate feedback mechanisms such as warmer global temperatures (e.g. Suan, et al., 2008), increased nutrient availability from continental runoff (e.g. Them II, et al., 2017b), and reduced ocean circulation (Dera & Donnadieu, 2012). However, debate remains on the initiating mechanism behind the observed changes. One suggestion is the emplacement of large igneous provinces (LIPs), which have been synchronously linked with most major OAEs; e.g. the Karoo–Ferrar LIP and the T-OAE at ~183 Ma (Burgess, et al. 2015; Sell, et al., 2014; Pálfy & Smith, 2000). Elevated Hg concentrations and Hg/TOC ratios in T-OAE sediments suggest periods of enhanced atmospheric Hg input from volcanic outgassing during LIP events (Them II, et al., 2019; Percival, et al., 2015). Extrusive igneous (volcanic) activity emits greenhouse gases such as methane, carbon dioxide and water vapour during eruptions, as will interactions of intrusive igneous bodies with organic-rich strata (e.g. coal, black shales) (Wignall, et al., 2009; Retallack & Jahren, 2008; Kuroda, et al., 2007; McElwain, et al., 2005). These emission processes result in global warming conditions akin to those anticipated during OAEs. Contributing factors to OAEs spurred by environmental changes may include decreasing oxygen solubility with increasing ocean temperatures (Meyer & Kump, 2008), destabilisation or decomposition of methane hydrates from sediments that exacerbate greenhouse warming effects (Them II, et al., 2017a; Hesselbo, et al., 2007; 2000) and increased continental weathering that elevates nutrients in runoff and thus primary productivity where nutrients become available (Pogge von Strandmann, et al., 2013; Jenkyns, 2010).

2.3. Expansion of Anoxia/Euxinia during the T-OAE

Redox sensitive trace metals (e.g. Mo, Re) are typically enriched in anoxic and/or euxinic sediments, but these types of sediments within the N-CIE of the T-OAE show muted enrichments (Them II, et al., 2017a; Them II, 2016; Jenkyns, 2010; Pearce, et al., 2008). The muted concentrations may be a result of enhanced global trace metal drawdown from seawater

into an increased area of anoxic/euxinic seafloor (Pearce, et al., 2008), rather than a shift to less anoxic conditions in the local depositional environment.

Stable Tl isotope (ε^{205}Tl) and Mo isotope (δ^{98}Mo) compositions can also be used to infer expanded ocean anoxia and euxinia (Them II, et al., 2018; Pearce, et al., 2008). Thallium isotope fractionation occurs when Tl adsorbs to Mn particulates, where the particulate is enriched in heavier ^{205}Tl ($\uparrow\varepsilon^{205}$Tl) and the surrounding seawater retains lighter ^{203}Tl ($\downarrow\varepsilon^{205}$Tl). Fractionation does not occur when Tl is removed from seawater into euxinic sediments. Since Mn particulates are preserved under well-oxygenated bottom waters (where pore water is also oxic), a decrease in oxic conditions—and thus an increase in anoxic conditions—will lead to heavier seawater ε^{205}Tl which is then recorded in organic-rich sediments. Them II et al. (2018) measured ε^{205}Tl in the Bighorn Creek (Alberta) and Dotternhausen Quarry (Germany) T-OAE sections. They found that ε^{205}Tl peaked at the N-CIE onset, followed by a minor decrease in the central N-CIE and a moderate increase towards the conclusion of the N-CIE in both sections. These signatures indicated two expansion events (at the onset and conclusion of the N-CIE) which they estimate to have required a decrease in oxic Mn burial area of ~25 to 50%, and therefore an equivalent increase in non-oxic (suboxic and/or anoxic) seafloor area to replace the lost oxic area.

Euxinic sediments record seawater δ^{98}Mo, which is controlled by preferential removal of the lighter Mo isotopes into oxic sediments and seawater enrichment of the heavier Mo isotopes. When areas of oxic seafloor decrease (and by inference the area of euxinic seafloor expands), the resulting seawater δ^{98}Mo also decreases, thus euxinic sediment δ^{98}Mo will decrease. Pearce et al. (2008) note pulsed δ^{98}Mo excursions to lighter compositions through the N-CIE of the T-OAE, coupled with pulses of isotopically-light carbon injections. These are inferred to capture expansion of euxinic seafloor by a minimum tenfold areal increase.

3. Geological Setting

The studied section (*c-B6-A/94-B-8*; 56°15′N, 122°04′W) is a 46 m drill core through Early Jurassic strata in the Western Canada Sedimentary Basin (WCSB), approximately 75 km west of Fort St John, British Columbia (**Figure 2**). The following section pertains to the local- to basin-scale geology of the stratigraphic units deposited during the Early Jurassic of the WCSB.

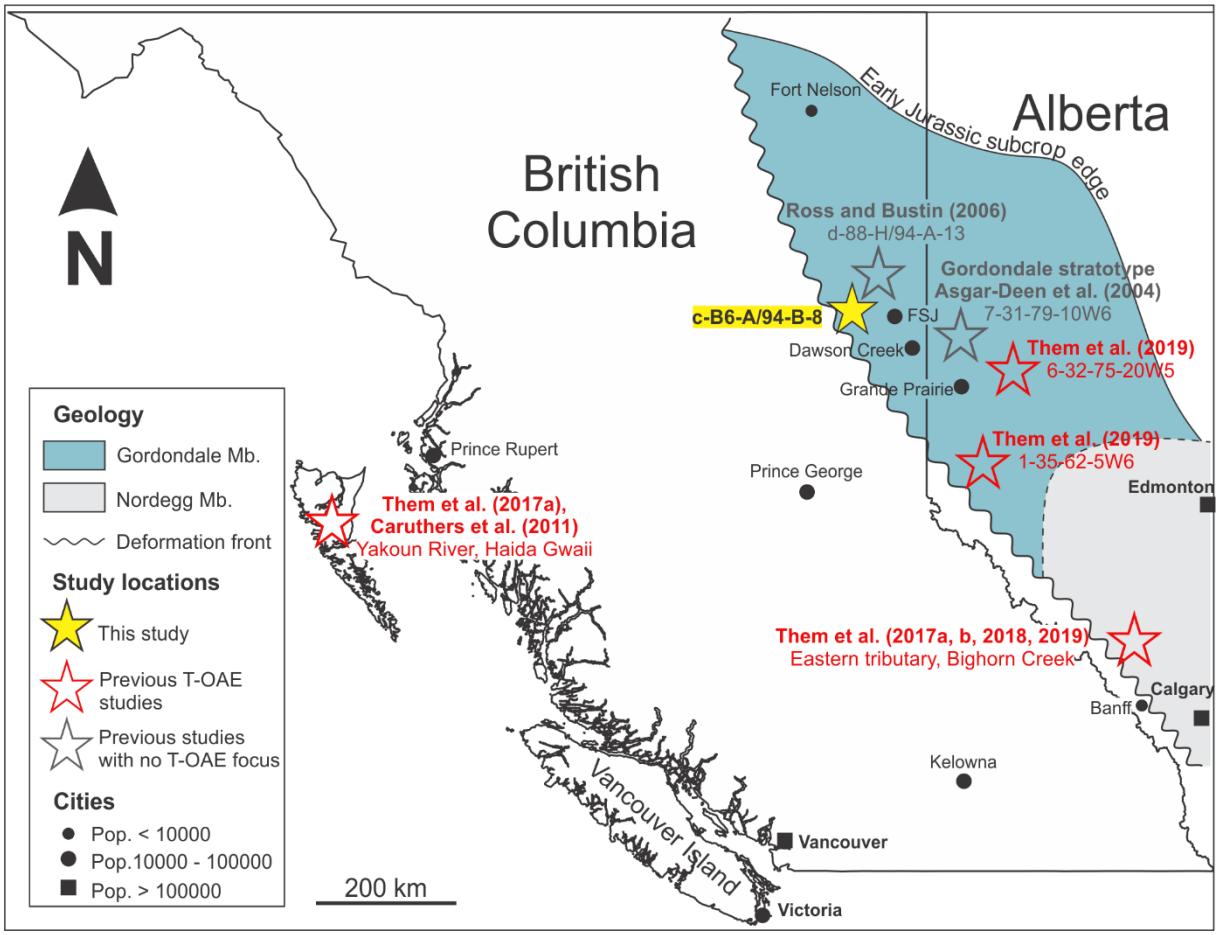

***Figure 2*. Study Area.** The cored section (*c-B6-A/94-B-8*; yellow star) cuts through Early Jurassic strata of the Western Canada Sedimentary Basin (WCSB) ~75 km west of Fort St John (FSJ), British Columbia. The Early Jurassic of the WCSB includes the Gordondale Member (Mb; blue shading), its southern Alberta equivalent (Nordegg Mb; grey shading) and the Poker Chip Shale (over most of the areas shaded blue or grey). Known T-OAE studies (with N-CIE identified) are indicated by red stars. A selection of non-T-OAE focused sections are included (grey stars); these do not have carbon isotope data to identify the N-CIE of the T-OAE. Modified from Kunert et al. (2019).

3.1. Stratigraphy of the Lower Fernie Formation

In the WCSB, the Fernie Formation comprises all Jurassic strata and is divided into several members across the basin. The lower Fernie Formation includes the Hettangian to Pliensbachian Gordondale Member and Toarcian Poker Chip Shale (PCS) in northeastern British Columbia (**Figure 3**), and the Sinemurian to Pliensbachian Nordegg and Red Deer members, and Toarcian Poker Chip Shale in central to southern Alberta.

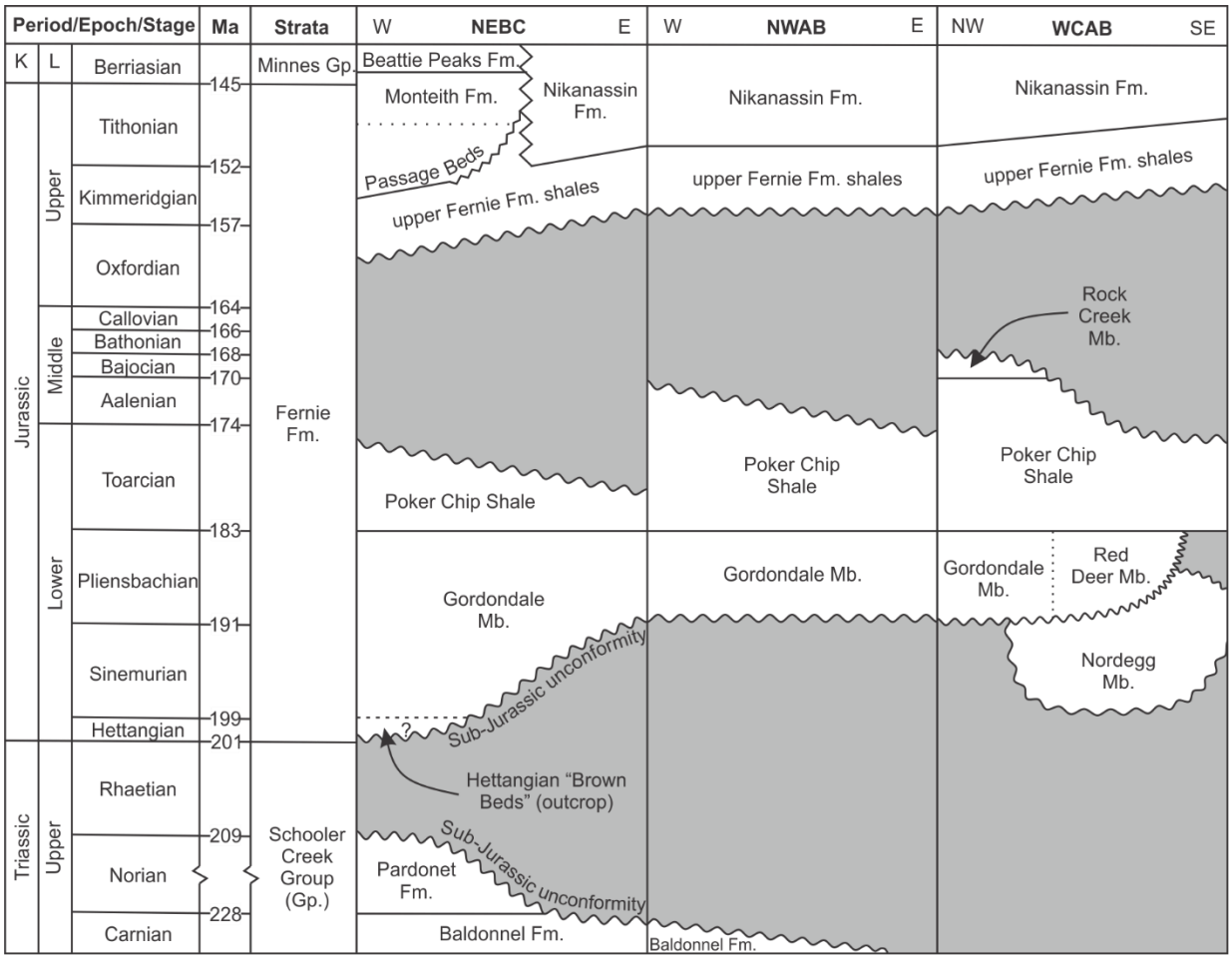

Figure 3. **Jurassic Stratigraphy of the Western Canada Sedimentary Basin (WCSB).** Upper Triassic, Jurassic and Lower (L) Cretaceous (K) stratigraphic units in northeastern British Columbia (NEBC), northwestern Alberta (NWAB), and west-central Alberta (WCAB) after Poulton et al. (1994; 1990) and Asgar-Deen et al. (2004). The Jurassic of the WCSB is complex owing to erosional or non-depositional hiatuses (grey areas). This study focuses on the Lower Jurassic Gordondale Member (Mb.) and Poker Chip Shale of the lower Fernie Formation (Fm.) in NEBC. The Poker Chip Shale extends into central and southern Alberta, however, the deeper-marine Gordondale Mb transitions to the shallower-marine facies of the Red Deer and Nordegg members in Alberta.

3.1.1. Gordondale Member

The Gordondale Member of the Fernie Formation is the basal Jurassic unit extending from NEBC to west-central Alberta (57°N to 54°N) in the subsurface and from NEBC to southern Alberta (57°N to 51°N) in Rocky Mountain outcrops (**Figure 2**; after Asgar-Deen, et al., 2004). The Gordondale Member unconformably overlies the Upper Triassic Pardonet and Baldonnel formations in NEBC and progressively overlies older strata towards the eastern extent of the basin due to pre-Jurassic subaerial erosion (Poulton, et al., 1994). Overlying the Gordondale Member is the Early Jurassic PCS, also of the Fernie Formation, either conformably or unconformably depending on the area (Asgar-Deen, et al., 2004; Riediger, 2002). The Gordondale Member varies in thickness and is a lens-shaped stratigraphic unit when viewed in a northeast–southwest cross-section. The member reaches a maximum thickness of 40 m along a north–northwest trending depocenter parallel to the Rocky Mountains (and paleo-shoreline) and thins both westward and eastward (Poulton, et al., 1994). To the west, the unit thins depositionally and is found outcropping with a thickness of ~15 m in NEBC (Asgar-Deen, et al., 2004), while eastward thinning and subcropping is related to subaerial erosion prior to Cretaceous deposition (Poulton, et al., 1994).

The Gordondale Member is a fine-grained marine mudstone and is typically dark grey to black from its high C_{org} content (2–28%; Kondla, et al., 2017; Ross & Bustin, 2006; Riediger & Bloch, 1995; Riediger, 1991). The Gordondale Member is calcareous and variably phosphatic, exhibiting fibrous calcite veins (Riediger & Coniglio, 1992) and phosphate nodules (Riediger & Bloch, 1995). The type section is located in the subsurface in northwestern Alberta (*7-31-79-10W6*; 55°53′N, 119°33′W; Asgar-Deen, et al., 2004).

Several informal subunits have been defined within the Gordondale Member in previous works; although nomenclature varies, these units are more-or-less equivalent. The Lower Unit—"Lower Radioactive Unit" (Kondla, et al., 2017; Asgar-Deen, et al., 2004), "Unit B" (Ross & Bustin, 2006), "Unit 1" (Asgar-Deen, et al., 2003), "lower unit" (Riediger & Bloch, 1995; Riediger & Coniglio, 1992), or "Lower Member" (Riediger, 1991) (see **Table 1**)—is the most organic-rich interval with reported C_{org} values of up to 28% (Riediger, 1991). It is recognisable on gamma-ray petrophysical logs with values greater than 500 American Petroleum Institute (API) units (Kondla, et al., 2017). The Lower Unit ranges from 8 to 25 m in

thickness (Asgar-Deen, et al., 2004) and averages approximately 9 m (Riediger & Bloch, 1995). Riediger and Bloch (1995) and Asgar-Deen et al. (2004) report interbedded green, non-calcareous siltstones, shrinkage cracks, parallel laminations and barite nodules within this subunit. It hosts the highest carbonate (calcite and dolomite) and phosphate (fluorapatite) contents, intermediate pyrite and clay (illite and kaolinite) contents, and the lowest detrital content (proxied by quartz) of the three subunits (**Table 2**; Ross & Bustin, 2006; Riediger & Bloch, 1995). Correspondingly, this subunit has the highest elemental calcium (as CaO) and phosphorus (as P_2O_5) contents and intermediate contents of pyrite-forming elements iron (as FeO) and sulfur (S_{TOT}), and clay-forming aluminium (as Al_2O_3) (Ross & Bustin, 2006; Riediger & Bloch, 1995). Redox-sensitive trace metals vanadium (V) and chromium (Cr) have elevated concentrations compared to other subunits; however, barium (Ba) content is lowest in this subunit (Ross & Bustin, 2006).

Table 1. **Comparison of Lower Jurassic stratigraphic nomenclature from the literature.** No consensus on subunit or member naming conventions has been reached for the Lower Fernie Fm. strata in the WCSB. Various names are applied to each subunit throughout the published history on the units (1990 to 2017 here).

<table>
<tr><th colspan="2">This Paper</th><th colspan="2">Kondla et al. (2017), Asgar-Deen et al. (2004)</th><th colspan="2">Ross & Bustin (2006)</th><th colspan="2">Asgar-Deen et al. (2003), Asgar-Deen (2003)</th><th colspan="2">Riediger (2002)</th><th colspan="2">Riediger & Bloch (1995), Riediger & Coniglio (1992)</th><th>Poulton et al. (1990)</th></tr>
<tr><td colspan="2">PCS</td><td colspan="2">PCS</td><td colspan="2">PCS</td><td colspan="2">PCS</td><td rowspan="2">PCS</td><td>B</td><td colspan="2">PCS</td><td>PCS</td></tr>
<tr><td rowspan="3">Gordonale Member</td><td>Upper Unit</td><td rowspan="3">Gordonale Member</td><td>Upper Radioactive Unit</td><td rowspan="3">Gordonale Member</td><td>Unit D</td><td rowspan="3">“ Nordegg Member”</td><td>Unit 3A</td><td>A</td><td rowspan="3">“ Nordegg Member”</td><td>upper unit</td><td rowspan="3">“ Nordegg Member”</td><td rowspan="3">Lower Fernie Limestones & Shales</td></tr>
<tr><td>Middle Unit</td><td>Middle Silty Unit</td><td>Unit C</td><td>Unit 2</td><td>middle unit</td><td>middle unit</td></tr>
<tr><td>Lower Unit</td><td>Lower Radioactive Unit</td><td>Unit B</td><td>Unit 1</td><td>lower unit</td><td>lower unit</td></tr>
</table>

Table 2. **Select geochemical compositions of Gordondale Member subunits.** Compilation means from several geochemical studies of the Gordondale Member which have reported values for the subunits. Reported with ± 1 standard deviation (1s). Abbreviations: C_{org} = organic carbon, ICP-MS = inductively coupled plasma mass spectrometry, NA = not available, PCS = Poker Chip Shale, S_{TOT} = total sulfur.

Component	Lower[1,3,5,6]	Middle[2,3,6]	Upper[1,2,3,4,5,6]	PCS[4,5]	Analyses	Source(s)
C_{org} (%)	7.5 ± 3.6	7.7 ± 3.7	5.4 ± 2.3	0.3 ± 0.3	Rock-Eval	2,3,4,5,6,7
S_{TOT} (%)	2.4 ± 1.0	1.7 ± 1.3	3.0 ± 1.8	5.0 ± 1.8	Combustion	3,4,5
Carbonates* (%)	36 ± 22	22 ± 17	23 ± 24	NA	X-ray diffraction or calculation	
Quartz (%)	26 ± 13	74 ± 22	31 ± 14			
Clays** (%)	11 ± 12	2.7 ± 3.2	27 ± 23			
Fluorapatite (%)	7.6 ± 9.2	0.1 ± 0.2	3.6 ± 5.9			
Pyrite (%)	3.1 ± 1.6	0.3 ± 0.2	5.5 ± 3.6			
CaO (%)	23 ± 12	16 ± 6.5	16 ± 15	1.6 ± 1.0	X-ray fluorescence	
Al_2O_3 (%)	6.0 ± 3.0	4.4 ± 2.3	9.3 ± 4.2	15.2 ± 1.6		
P_2O_5 (%)	3.5 ± 4.1	0.9 ± 0.5	3.2 ± 4.3	0.5 ± 0.6		
Fe_2O_3 (%)	2.1 ± 0.9	1.7 ± 1.7	4.0 ± 2.0	6.4 ± 1.1		
V (µg/g)	2200 ± 560	300 ± 320	290 ± 170	66 ± 16		3
Re (ng/g)	200 ± 91	NA	300 ± 69	130 ± 38	ICP-MS	1

*calcite + dolomite
**illite + kaolinite
[1]Pană et al. (2018)
[2]Kondla et al. (2017)
[3]Ross and Bustin (2006)
[4]Ross (2004)
[5]Riediger (2002)
[6]Riediger and Bloch (1995)
[7]Riediger et al. (1994)

The Middle Unit—"Middle Silty Unit" (Kondla, et al., 2017; Asgar-Deen, et al., 2004), "Unit C" (Ross & Bustin, 2006), "Unit 2" (Asgar-Deen, et al., 2003), "middle unit" (Riediger & Bloch, 1995; Riediger & Coniglio, 1992), or "Middle Member" (Riediger, 1991) (see **Table 1**)—is the thinnest and least radioactive of the three subunits, with thicknesses from 2 to 12 m when present and gamma ray values from 75 to 135 API (Kondla, et al., 2017; Ross & Bustin, 2006; Asgar-Deen, et al., 2004). The Middle Unit is light grey-beige to brown, and is similar to the Nordegg Member platformal cherty carbonates of central to southern Alberta (Asgar-Deen, et al., 2004). The organic content in the Middle Unit is less than the underlying Lower Unit. However, reported C_{org} of up to 20% occurs in intervals associated with fractured zones (Ross & Bustin, 2006) which may indicate hydrocarbon migration into this subunit rather than depositional organic matter. Mineralogy (**Table 2**) indicates a high detrital (quartz) component, and low phosphate, pyrite and clay contents for the Middle Unit (Ross & Bustin, 2006). Carbonate content is also high (Ross & Bustin, 2006), but less than the carbonate content in the Lower Unit. As in the Lower Unit, major element contents correlate closely with XRD mineralogy: CaO in carbonates, P_2O_5 in phosphates, Fe_2O_3 and S_{TOT} in pyrite, and Al_2O_3 in clays are lowest in the Middle Unit (Ross & Bustin, 2006). The Middle Unit has intermediate V and Ba contents, and the lowest concentrations of Cr (Ross & Bustin, 2006).

The Upper Unit—"Upper Moderately Radioactive Unit" (Kondla, et al., 2017; Asgar-Deen, et al., 2004), "Unit D" (Ross & Bustin, 2006), "Unit 3A" (Asgar-Deen, et al., 2003), "Poker Chip Shale A" (Riediger, 2002), "upper unit" (Riediger & Bloch, 1995; Riediger & Coniglio, 1992), or "Upper Member" (Riediger, 1991) (see **Table 1**)—has gamma ray values ranging from approximately 150 to 250 API and thus is more radioactive than the underlying Middle Unit, but less radioactive than the Lower Unit (Asgar-Deen, et al., 2004). Maximum reported C_{org} in the Upper Unit is 20% (Riediger & Bloch, 1995), therefore it is organic-rich but not to the degree reported for the Lower Unit. The Upper Unit contains similar carbonate concentrations to the Middle Unit and similar quartz content to the Lower Unit. Clay and pyrite contents are much greater in this unit than in the Lower and Middle units, and the phosphate content is intermediate (**Table 2**; Ross & Bustin, 2006; Riediger & Bloch, 1995). Hence, the Upper Unit has similar CaO content to the Middle Unit, higher Fe_2O_3, S_{TOT} and Al_2O_3 than the Lower and Middle Units, and moderate P_2O_5 concentrations (Ross & Bustin, 2006; Riediger & Bloch, 1995). The Upper Unit has the lowest V, intermediate Cr and the highest Ba concentrations (Ross & Bustin, 2006).

3.1.2. Red Deer and Nordegg members

The Red Deer Member is a western- to southern-Alberta age-equivalent unit to the Gordondale Member and is similar in lithology—mainly black shales and platy limestones (Asgar-Deen, et al., 2003; Frebold, 1969). The type locality outcrops along Bighorn Creek in the Alberta foothills west of the city of Red Deer (Asgar-Deen, et al., 2003). Recent studies by Them II et al. (2019; 2018; 2017a; 2017b) and Them II (2016) on the East Tributary of Bighorn Creek (**Figure 2**) correlated the Red Deer Member at this locality with the Gordondale Member in the subsurface to the northwest.

Much of the lowermost Early Jurassic strata of the WCSB was originally assigned to the Nordegg Member of Spivak (1949). The true Nordegg Member of central to southern Alberta is composed of massive, platformal, cherty carbonates with blocky gamma ray signatures and is of hydrocarbon reservoir quality in some areas (e.g. Gilby and Pine Creek oil and gas fields; Poulton, et al., 1994). The chert/limestone facies grades into radioactive black shales to the north, and early studies of the shale facies in northwestern Alberta and NEBC began referring to them as "Nordegg Member" (in quotations; e.g. Riediger & Bloch, 1995;

Poulton, et al., 1994; Riediger, 1990). More recently, however, the black shale facies have been re-assigned to the Gordondale Member (Asgar-Deen, et al., 2004).

3.1.3. Poker Chip Shale

The Poker Chip Shale is found in central to southwestern Alberta overlying the Nordegg/Red Deer members, and in central to northwestern Alberta and NEBC overlying the Gordondale Member (Riediger, 2002). The type sections of the PCS are located in the subsurface from Turner Valley (50 km west-northwest of Calgary) to Wildcat Hills (50 km southwest of Calgary) and are composed of organic-rich (C_{org} > 1%), calcareous, black shales (Spivak, 1949). Riediger (2002) defines the type PCS interval as "Poker Chip Shale A" (PCS-A); the interval has also been defined as "Gordondale Member Upper Moderately Radioactive Unit" (Kondla, et al., 2017; Asgar-Deen, et al., 2004), "Gordondale Member Unit D" (Ross & Bustin, 2006), and/or " 'Nordegg Member' Unit 3A" (Asgar-Deen, et al., 2003) as described above. Riediger (2002) described a second PCS interval ("Poker Chip Shale B", PCS-B) which unconformably overlies the Gordondale Member Upper Unit. Poker Chip Shale B is an organic-poor (C_{org} < 1%), non-calcareous, grey-green shale containing pyrite and several ash beds (Riediger, 2002). In this work, the PCS-A is called the "Gordondale Member Upper Unit" because its calcareous/carbonate geochemistry more closely resembles the Gordondale Member mudstones, versus the non-calcareous/pyritic PCS-B which is herein referred to simply as the "Poker Chip Shale" (PCS).

3.2. Biostratigraphy and Geochronology

Many of the original correlations and ages of the Early Jurassic in the WCSB are derived from ammonite biostratigraphy. Recent geochronology techniques such as uranium–lead (U–Pb) dating of ash bed zircons and detrital zircons, and rhenium–osmium (Re–Os) dating of black shales provide absolute age constraints on Lower Jurassic strata that corroborate ages from biostratigraphy.

3.2.1. Ammonite Ages

The Gordondale Member, extending from the west-central Alberta (WCAB) subsurface to NEBC subsurface and outcrop, contains ammonite genera dating from the Hettangian to Toarcian stages. Hettangian *Psiloceras*, *Discamphiceras*, *Waehneroceras*, *Kammerkarites*,

Schlotheimia, Sunrisites, Laqueoceras, Badouxia, Pseudaetomoceras and *Vermiceras* are found in NEBC outcrop (Hall & Pitaru, 2004; Poulton, et al., 1990). Upper Hettangian *Discamphiceras* (Hall, et al., 2000) and Hettangian *Alsatites* (Lower Unit; Asgar-Deen, et al., 2003) are found in subsurface sections in the WCAB subsurface. The Upper Hettangian *Discamphiceras* reported in the lower Gordondale Member in northwest Alberta was found with Upper Hettangian to Lower Sinemurian coccoliths, indicating an age as young as Lower Sinemurian in that section (Hall, et al., 2000). Lower Pliensbachian ammonite genera *Prodactylioceras, Lytoceras*, and acanthopleuroceratid are found in NEBC outcrops (Poulton, et al., 1990). The acanthopleuroceratid ammonites are known to occur regionally in the member (Pană, et al., 2018). Early Toarcian ammonite genus *Orthodactylioceras* and Middle Toarcian ammonite species *Harpoceras* cf. *subplanatum* were reported at the top of the Lower Unit (Unit 1b in their study) in one subsurface section (*6-32-78-5W6*; Asgar-Deen, et al., 2003). This finding by Asgar-Deen et al. (2003) is problematic in that their "Unit 1b" is herein referred to as the Lower Unit, however it is possible that the nomenclature is mismatched. No other studies are known to report Toarcian ages for the Gordondale Member Lower Unit, however the Upper Unit may be of Toarcian age given that it is correlative with the Early to Late Toarcian PCS-A of Riediger (2002). Ammonite biostratigraphy has therefore placed the Gordondale Member in the Hettangian (outcrop strata and lowermost Lower Unit) to Toarcian stages (potentially Lower Unit [Asgar-Deen, et al., 2003], but most likely Upper Unit only).

Through the WCAB foothills, the Gordondale Member grades into the Red Deer Member, which has recently reported biostratigraphy from the East Tributary of Bighorn Creek, Alberta (Them II, 2016). Ammonite species *Amaltheus stokesi* and *Protogrammoceras kurrianum* (Upper Pliensbachian), *Tiltoniceras* cf. *antiquum* and *P. paltum* (Pliensbachian to Toarcian), and *Clericeras exaratum* and *Hildaites* cf. *murleyi* (Lower Toarcian) are described, making the Red Deer Member age-correlative with portions of the Gordondale Member.

The Nordegg Member contains the Pliensbachian ammonite genus *Amaltheus* at Limestone Mountain in WCAB (Asgar-Deen, et al., 2003). Additionally, the member contains *Oxytoma* bivalve beds dated generally from the Early Jurassic, similar to those found in the Gordondale Member (Asgar-Deen, et al., 2003). The presence of the Pliensbachian ammonite makes the Nordegg Member age-correlative with portions of the Gordondale and Red Deer members.

In addition to the Red Deer Member ammonites, Them II (2016) describes specimens from the PCS in the same section on the East Tributary of Bighorn Creek. The lowermost PCS at the East Tributary outcrop contains Lower Toarcian ammonite species *Clericeras exaratum*, *Hildaites* cf. *murleyi*, *Dactylioceras* cf. *semicelatum*, and *Harpoceras* cf. *falciferum*, Lower to Middle Toarcian ammonite species *Dactylioceras commune* and *D. athleticum*, and Middle Toarcian ammonite species *Harpoceras* cf. *subplanatum*, *Pseudolioceras* cf. *lythense* and genera *Zugodactylites*, *Peronoceras*, and *Phymatoceras*. Asgar-Deen et al. (2003) report the Upper Toarcian ammonite genus *Yakounia* in "'Nordegg' Member Unit 3B" (also called the PCS-B in Riediger, 2002; and PCS in this work) in northwestern Alberta, and Poulton et al. (1990) note Upper Pliensbachian or Toarcian to Aalenian palynomorph (pollen) assemblages, Lower Toarcian ammonite genera *Harpoceras* and *Dactylioceras*, and Aalenian dinocyst *Jansonia jurassica* in NEBC PCS outcrops.

3.2.2. U–Pb and Re–Os Ages

Uranium–lead (U–Pb) dating of zircons from ash beds interbedded in sedimentary successions is used to determine the absolute crystallization ages of those zircons and, by the law of superposition, the approximate depositional ages of the sedimentary units immediately overlying and underlying the ash beds.

Some Jurassic units of the WCSB contain interbedded ash or weathered ash (bentonite) layers, which have provided U–Pb ages consistent with reported biostratigraphic ages. The Red Deer Member from the East Tributary of Bighorn Creek (Alberta) has a reported bentonite U–Pb age of 188.3 +1.5/–1.0 million years (Ma; 2σ; $n = 5$) approximately 1 m above the sub-Jurassic unconformity (Hall, et al., 2004). Them et al. (2017b) report ages for two bentonites in a 13.5 m section of the Red Deer Member on the East Tributary section. The first bentonite is situated approximately 1 m above the sub-Jurassic unconformity and has an age of 188.58 ± 0.17 Ma (2σ; $n = 5$) that agrees with the age of Hall et al. (2004). The second bentonite is approximately 5 m above the unconformity and gave an age of 185.49 ± 0.16 Ma (2σ; $n = 5$). All three ages place the lower portion of the Red Deer Member within the Pliensbachian stage, consistent with the biostratigraphic age from *Amaltheus* ammonites found in the unit (Them II, 2016).

Recent U–Pb dating of Nordegg Member ash beds in three sections (McLeod River, Prairie Creek Quarry, Shunda Creek bridge) of the western Alberta foothills by Pană et al. (2018b) yielded ages of 187.21 ± 0.48 Ma (2σ; *n* = 2), 185.25 ± 0.66 Ma (95% confidence interval, CI; *n* = 2) and 186.8 ± 1.5 Ma (95% CI; *n* = 23). These ages place the Nordegg Member in the Pliensbachian stage, and overlap the Red Deer Member ages of Them II (2016) and Hall et al. (2004) within analytical uncertainties.

The PCS has incorporated detrital zircons with a U–Pb youngest peak age of 186.5 ± 5.3 Ma (*n* = 10) and a youngest single-grain age of 176 ± 7 Ma, giving the member a maximum depositional age in the Pliensbachian to Toarcian stages (Pană, et al., 2017).

No U–Pb ages for the Gordondale Member are known to have been reported; however, the rhenium–osmium (Re–Os) isochron method to directly date the deposition of organic-rich black shales has been applied to the member. Pană et al. (2018a) report a Re–Os isochron age near the base of a northwestern Alberta Gordondale Member subsurface section (*13-28-73-21W5*; 55°21′N, 117°10′W) of 192.0 ± 1.4 Ma (2σ), placing it in the Sinemurian stage. The PCS has a Toarcian Re–Os isochron age of 182.0 ± 2.5 Ma (2σ; *13-28-73-21W5*) at the contact between the Gordondale Member and PCS (Pană, et al., 2018a). These reported ages agree well with U–Pb zircon and biostratigraphic ammonite ages of equivalent members. The Re–Os isochron ages in the *13-28-73-21W5* section for the bases of the Gordondale Member and PCS provide an approximate Gordondale Member depositional period of at least 10.0 ± 3.9 million years (2σ).

3.3. Paleotectonics

The WCSB experienced a change in tectonic regime during the Jurassic Period, moving from a stable/passive margin to an orogenic/active subducting margin along the western coast of ancient North America. These changes resulted in the complex Cordilleran geology currently observed: easternmost Rocky Mountains (Alberta and British Columbia), multiple westerly-derived allochthonous magmatic terranes through British Columbia, and westernmost Coast Mountains (British Columbia). Upper Jurassic sedimentary units in western Alberta and NEBC contain western-sourced orogenic clastic material, making them the youngest, most obvious indication of orogenic initiation; however, much of the tectonic evidence for determining a more precise timeline of initiation has been lost to erosion (Poulton, et al., 1994).

Other lines of evidence have been used to argue for an earlier initiation of orogenic activity. Oxygen isotope signatures indicate meteoric water runoff from western terranes into the depositional basin of the Early to Middle Jurassic (Riediger & Coniglio, 1992). Detrital zircons found in Lower and Middle Jurassic WCSB strata are nearly euhedral (i.e. minimal transport) and produce U–Pb youngest peak ages similar to the ages of their host sedimentary units (Pană, et al., 2017). The findings in Pană et al. (2017) imply orogenic initiation by at least the Early Jurassic as the Cordilleran magmatic arc to the west of the depositional basin began to supply the syn-depositional zircons.

3.4. Paleogeography and Paleohydrography

Early Jurassic deposition in the WCSB occurred on the western edge of the rifting supercontinent Pangea in the northwestern corner of Laurasia (early North America) where it met the Panthalassa (Proto-Pacific) ocean (Scotese, 2013; **Figure 4**). At that time the region straddled ~36°N to 50°N latitude (van Hindsbergen, et al., 2015), as evidenced by the presence of a carbonate platform (Nordegg Member) which typically develops in tropical to sub-tropical regions (Wilson, 1975). Deeper-water, finer-grained marine units of the Early Jurassic in the basin (Gordondale Member, Red Deer Member, PCS) show characteristics of anoxic (oxygen-free) deposition, e.g. high C_{35}/C_{34} hopane (biomarker) ratios (Riediger & Coniglio, 1992) and abundant preserved organic matter (Riediger & Bloch, 1995). Oscillating laminations of apatite-bearing intervals (suboxic to oxic conditions) with pyrite-bearing intervals (anoxic) (Riediger & Bloch, 1995) suggest intermittent periods of less anoxic deposition or post-depositional oxygenation. Riediger and Bloch (1995) also note the presence of excess sulfur associated with organic matter; this is likely the result of euxinic bottom water conditions (anoxic and sulfidic) caused by bacterial sulfate reduction. Anoxia is suggested to be a result of two mechanisms: (1) basin sills (submarine ridges oriented parallel to the shoreline) and (2) a hypersaline pycnocline limiting water mass exchange (Riediger & Bloch, 1995; Riediger & Coniglio, 1992).

The Gordondale Member was likely deposited in an open ocean environment and may have been separated from the more restricted Red Deer and Nordegg members by a sill (Poulton, 1991). Thus, while all three members exhibit anoxic traits, the mechanism responsible for those anoxic conditions may be different for each member.

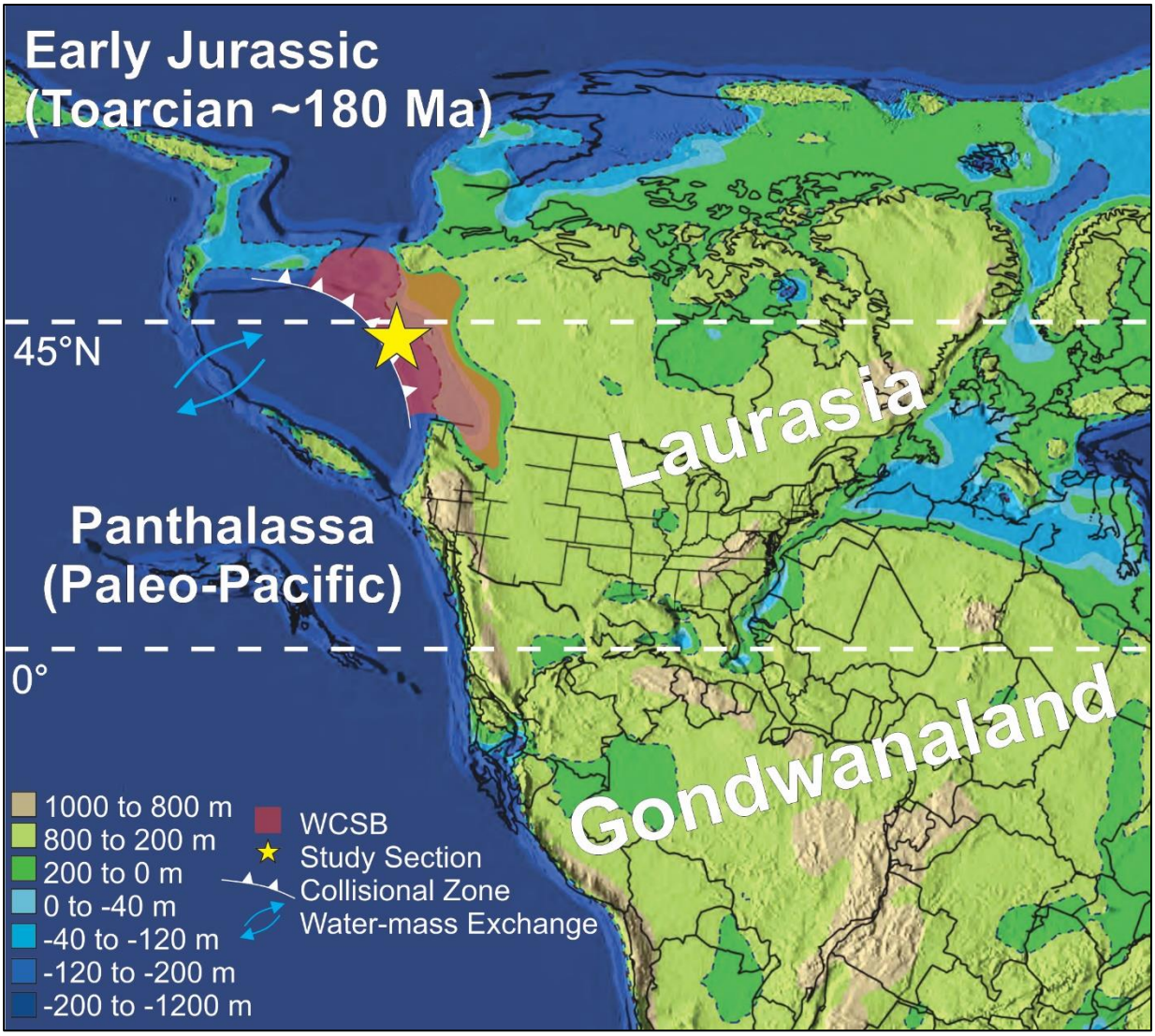

Figure 4. **Early Jurassic Paleogeography.** Paleogeography of the Early Jurassic Period approximately 180 million years ago (Ma) of the area around and covered by modern North America; modified from Scotese (2013). The Western Canada Sedimentary Basin (WCSB) depositional area is highlighted (red), as is the study section (yellow star) within the basin. Paleolatitudes were approximated using the model of van Hinsbergen et al. (2015). Sea level is set at 0 m, with coloured areas representing altitudes above (greens and browns; assumed sub-aerial) and below (blues; assumed sub-marine) sea level. Sub-marine depths greater than –200 m are situated on the continental shelf, while those less than –200 m are continental slope and abyssal plain.

3.5. Carbon Geochemistry and Thermal Maturity

The Gordondale Member is an excellent source rock with up to 28 wt% C_{org} (Riediger, 1991; Creaney & Allan, 1990). Riediger (2002) described the PCS-A (equivalent to the Upper Unit of the Gordondale Member) with excellent source potential from its elevated C_{org} of up to 18.5 wt%, while the PCS-B (or simply "PCS") is not a source rock (C_{org} < 1 wt%). Kerogen (a

precursor to hydrocarbons) in the Gordondale Member is Type II-S, indicating a marine origin ("Type II") and incorporation of excess sulfur ("-S") into the organic matter (Riediger & Bloch, 1995). Programmed pyrolysis Tmax values, a proxy for thermal maturity, increase from northeast to southwest across the basin; therefore, the overmature areas are closest to the Rocky Mountain deformation front, while the immature areas lie along the easternmost extent of the basin (Riediger, 2002; Riediger, 1990).

Organic carbon isotope signatures ($\delta^{13}C_{org}$) of the Early Jurassic in the WCSB show baseline values averaging approximately –28‰ in outcrop (East Tributary, Bighorn Creek) and subsurface (northwestern Alberta) sections (Them II, et al., 2019), indicating a marine phytoplankton source (Boutton, 1991). The overall trend is that of a broad positive carbon isotope excursion (P-CIE) of approximately +2‰ beginning in the mid-Pliensbachian and ending in the Upper Toarcian (Them II, et al., 2019). However, in the earliest Toarcian, the uppermost Gordondale and Red Deer members, and lowermost PCS strata exhibit an abrupt negative carbon isotope excursion (N-CIE) of up to –4‰ from baseline values (Them II, et al., 2019; 2017a). The N-CIE may be recording a global phenomenon rather than local variations, as the trend is reflected in coeval sections through North America, Europe and Japan (e.g. Them II, et al., 2017a; Gröcke, et al. 2011; Schouten, et al., 2000; Jenkyns, 1988).

4. Marine Geochemistry

4.1. Carbon Geochemistry

4.1.1. Global Carbon Cycle

The global carbon cycle is an important biogeochemical cycle due to its major role in biological, geological, hydrological and atmospheric processes (Faure, 1991). These components of the Earth system outline the major reservoirs for carbon in its various forms. Biological components include terrestrial plants and animals, and aquatic (riverine or marine) plants, animals and plankton. Geological components include carbon-bearing rocks and sediments (e.g. carbonates), organic matter buried within sediments, and hydrocarbons (e.g. coal, oil, gas) stored in sedimentary basins. The hydrological domain is a transient reservoir; particulate or dissolved carbon transfer to and from the aqueous environment occurs quickly relative to other reservoirs.

4.1.2. Forms of Carbon

Earth's carbon can be divided into C_{org} and inorganic carbon (C_{inorg}). Organic carbon is a product of biological processes and is therefore found in the biological reservoir as living biomass. However, the hydrological and geological reservoirs also contain the remains of past biomass as particulate organic matter, organic matter buried in sediments, and kerogen or hydrocarbons in rocks. "Organic carbon" is a catch-all term to describe a collection of complex carbon-bearing molecules which make up organic matter; these molecules also include other essential elements for life like phosphorus (P) and nitrogen (N). The Redfield Ratio (Redfield, 1934) is the typical stoichiometry used to describe average organic matter composition where the ratio of C:N:P is 106:16:1 denoted by the chemical formula $(CH_2O)_{106}(NH_3)_{16}H_3PO_4$.

Inorganic carbon is found in mineralogical, dissolved or gaseous compounds and is produced through abiotic processes. Carbon dioxide (CO_2) is the most abundant gaseous form of carbon in Earth's atmosphere, followed by methane (CH_4); both gases are radiative and contribute to the greenhouse effect. In solid and dissolved forms, the carbonate anion (CO_3^{2-}) is the main inorganic carbon phase, often precipitating to form the minerals calcite ($CaCO_3$) and dolomite ($CaMg(CO_3)_2$).

4.1.3. Stable Carbon Isotopes

Elemental carbon in the natural environment is composed predominantly of two stable isotopes (a third isotope, carbon-14, is radioactive and will not be discussed). The lighter carbon-12 (^{12}C) isotope is the more abundant of the two, averaging 98.89% of stable carbon on Earth; the remaining 1.11% is represented by the heavier carbon-13 (^{13}C) isotope (West, et al., 2006). This ratio is not constant due to mass-dependent fractionation processes that vary the proportion of ^{12}C and ^{13}C by up to 10% (Faure, 1991). Fluctuations in the stable carbon isotope ratio ($\delta^{13}C$) of sedimentary material can be measured and reported using **Equation 1**.

(1)
$$\delta^{13}C(‰) = \left(\frac{\left(\frac{^{13}C}{^{12}C}\right)_{sample}}{\left(\frac{^{13}C}{^{12}C}\right)_{standard}} - 1 \right) \times 1000$$

In **Equation 1**, the *sample* is the material for which the isotope composition is sought, the *standard* is an internationally accepted reference material with a known isotopic composition. For the stable carbon isotope system, Pee Dee Belemnite (PDB) was the original reference standard used in analysis. However, no PDB material remains so a new standard, Vienna PDB (VPBD), has been calibrated to the PDB reference scale and is used internationally (Werner & Brand, 2001).

Mass-dependent fractionation of carbon isotopes in nature is controlled by kinetic and equilibrium fractionation effects (Faure, 1991). Kinetic fractionation effects are those which are controlled by the energy requirements of a reaction process (e.g. in biological processes, the lighter isotope is favoured due to lower energy requirements). Equilibrium fractionation effects are those which are controlled by the isotope bonding strength, where the heavier isotope typically forms a stronger bond which is thus less likely to break during reaction processes (Faure, 1991). Photosynthesis is the primary kinetic fractionation process for carbon isotopes in nature and occurs when carbon dioxide is converted to organic compounds in primary producers (plants, phytoplankton). Photosynthetic mechanisms (e.g. CO_2 diffusion from atmosphere to cells, internal Calvin or Hatch–Slack cycles, organosynthesis) preferentially use the lighter ^{12}C isotope, so primary producers are enriched in ^{12}C and depleted in ^{13}C resulting in a more-negative $\delta^{13}C$ composition (Faure, 1991). Subsequent heterotrophic

consumption of primary producers transfers the isotopically-light carbon up the food chain, so all biological material has low-negative $\delta^{13}C$ compositions.

The ^{13}C depletions are preserved in hydrocarbons (coal, oil, gas) due to their biological origins as organic matter buried in sediments. However, post-depositional processes like thermogenic hydrocarbon "cracking" (reduction of complex hydrocarbons to simpler compounds during burial and maturation) can redistribute the lighter and heavier isotopes between partitioned hydrocarbon phases. Thermogenic methane (CH_4) attains the most negative $\delta^{13}C$ composition (–60 to –40 ‰), whereas heavier gases (e.g. ethane, propane, butane), oils and coal range between –45 to –20 ‰ (Fuex, 1977). Biogenic methane produced during methanogenesis (disproportionation) of organic matter by decomposers in soils records the lowest $\delta^{13}C$ compositions of known material to a minimum of –80‰ (Fuex, 1977).

Equilibrium fractionation effects occur more often in abiotic processes, such as the carbonate buffer system. Precipitated carbonate minerals (e.g. calcite, $CaCO_3$) are typically enriched in the heavier ^{13}C isotope compared to atmospheric CO_2 and aqueous H_2CO_3, HCO_3^- and CO_3^{2-} phases (Faure, 1991). Marine limestones typically have $\delta^{13}C$ compositions near 0‰ because the PDB standard was itself a marine limestone, but this can vary by ± 4‰ (Fuex, 1977).

4.1.4. Carbon Isotope Excursions

Global-scale carbon isotope excursions (CIEs) recorded in the carbonate and organic matter of marine sedimentary rocks represent major disturbances to the carbon cycle and are caused by global environmental perturbation(s). Positive CIEs (P-CIEs) are those where $\delta^{13}C$ compositions increase to a maximum through a stratigraphic section, followed by a return to lower baseline levels. These types of CIEs capture globally elevated levels of organic carbon burial—i.e. where isotopically-light biological carbon is sequestered into the inaccessible sedimentary carbon bank (Jenkyns, 2010). Biological processes such as photosynthesis make preferential use of ^{12}C, so inorganic carbon remaining in the environment shifts to heavier $\delta^{13}C$. As the removal of lighter ^{12}C from the biosphere continues, photosynthetic organisms begin to incorporate more isotopically-heavy ^{13}C, which is subsequently buried and records higher $\delta^{13}C$ compositions. Once the external disturbance ceases and the rate of organic burial slows, the carbon system re-equilibrates and $\delta^{13}C$ shifts back to lighter values.

In contrast, negative CIEs (N-CIEs) are those where $\delta^{13}C$ compositions decrease (become more negative), followed by a return to higher baseline levels. These events are less straightforward to interpret as they are not controlled by the organic carbon burial rate, but rather by injections of lighter carbon attributed to a pulsed release of gas hydrates or methane clathrates (Them II et al., 2017; Hesselbo et al., 2007; Kemp et al., 2005; Jahren et al., 2001; Hesselbo et al., 2000), emission of light volcanic CO_2 (Kuroda, et al., 2007), magmatic intrusion of coals and black shales (Wignall, et al., 2009; Retallack & Jahren, 2008; McElwain, et al., 2005), and/or upwelling of isotopically-light deep ocean waters (van de Schootbrugge, et al., 2005; Schouten, et al., 2000; Küspert, 1982).

4.2. Marine Redox and Paleoredox Proxies

Sediment trace metal concentrations are indicators of depositional pore water, bottom water, and/or water column redox conditions, and their use as redox proxies can be applied to both modern and past environments. Aqueous oxygen conditions are divided into oxic (O_2 > 2.0 ml/l), suboxic (O_2 from 2.0 to 0.2 ml/l), and anoxic (O_2 < 0.2 ml/l); anoxia is subdivided into ferruginous (dissolved Fe^{2+}-rich) and euxinic (bottom-water H_2S present; produced through bacterial sulfate reduction) (Tyson & Pearson, 1991). Some redox-sensitive trace metals are soluble under O_2-rich conditions and insoluble under O_2-poor conditions, therefore sediments deposited under increasingly anoxic waters should be enriched in these elements (Tribovillard, et al., 2006). Not all redox-sensitive trace metals are enriched equally for a specific redox state (e.g. euxinic versus ferruginous), therefore a multi-proxy approach for reconstruction of the ancient marine environment is taken for this work.

Thermal maturation of organic-rich rocks has not been shown to disrupt trace metal isotope systematics or decrease trace metal content in the sediment phase (Yang, 2019). Yang (2019) compares immature, mature and overmature samples from multiple cores in the Exshaw Formation (Alberta). While no trend is observed between trace metal concentrations and maturity, spatial variation may have been induced by local environmental effects rendering comparison ineffective. Dickson et al. (2019) performed pyrolysis (timed heating) experiments on known immature organic-rich mudrocks of the Posidonia Shale (Germany) and Kimmeridge Clay (United Kingdom). Their results confirm those of Yang (2019) such that studied trace metals (Mo, Zn and Cd) are not mobilized during maturation based on minimal fractionation

into bitumen phases. However, it was suggested that the loss of organic mass during diagenesis and catagenesis artificially increases the relative concentration of the metals and may double the metal/C_{org} ratios in the bulk sample (Dickson, et al., 2019). This could be problematic when using these metals for paleoenvironmental reconstruction in comparison to modern sediments which have not undergone post-depositional maturation. With this consideration, Dickson et al. (2019) do state that inference of changes to paleoenvironmental conditions on small spatial and temporal scales (e.g. within a single section) with similar maturation histories are not adversely affected.

4.2.1. Molybdenum

Molybdenum (Mo) is present in the upper continental crust at relatively low concentrations (1.5 µg/g; McLennan, 2001), but has relatively high seawater concentration (107 nM ≈ 10 ng/g; Collier, 1985) therefore Mo enrichments in organic-rich marine sediments deposited from anoxic bottom-waters typically suffer minimal detrital influence. Most marine Mo is supplied through riverine input (Reinhard, et al., 2013) and Mo exhibits conservative behavior in oxic seawater (Emerson & Huested, 1991). Sediments deposited under oxic bottom-water retain crustal Mo concentrations, except when manganese particulates are present (Crusius, et al., 1996). Efficient Mo sequestration to sediments occurs in euxinic environments where oxidized Mo(VI) (typically as the molybdate oxyanion MoO_4^{2-}) is reduced to Mo(IV) in Mo-polysulfides (Erickson & Helz, 2000), producing sediment enrichments commonly greater than 100 µg/g (Scott & Lyons, 2012). The necessity of free H_2S in bottom waters to precipitate Mo-polysulfides makes Mo useful in distinguishing suboxic and/or ferruginous conditions from euxinic conditions. Scott and Lyons (2012) note that an enrichment greater than crustal concentrations and less than 25 µg/g represents an intermediate Mo sink between oxic and euxinic conditions. This could be an environment with suboxic or anoxic (ferruginous) bottom waters and an H_2S chemocline within the sediment (pore water H_2S); molybdenum diffuses through the sediment towards deeper H_2S-rich pore water where it is then removed from solution.

Manganese (Mn)-oxyhydroxide particulate activity can artificially enhance Mo enrichment in sediments where an oxic water column overlies anoxic bottom- or pore-waters (Crusius, et al., 1996). The particulate shuttling process generates an increasing Mo

concentration gradient from the upper water column to the bottom waters. Molybdenum oxyanions adsorb to Mn particulates in the oxic water column and are effectively shuttled through the water column as the particulates sink. The Mn particles dissolve in the anoxic bottom waters or when interacting with anoxic pore waters below the sediment–water interface. During Mn particulate dissolution, Mo is released into the anoxic environment where it is captured and incorporated into anoxic sediments (Crusius, et al., 1996). The dissolved Mn returns to the oxic water column where the cycling may continue.

Sediment Mo concentrations between 25 and 100 µg/g may have been deposited in a euxinic environment involving one of several additional factors: (1) dilution due to rapid sedimentation; (2) alkaline waters causing reduced efficiency of Mo precipitation; (3) basin restriction with initially enhanced drawdown and depletion of aqueous Mo from the water column without repletion; and/or (4) seasonal redox variation (Hardisty, et al., 2018; Scott & Lyons, 2012; Helz, et al., 2011). Further study has illustrated additional factors that can complicate interpretation of Mo concentrations. Scholz et al. (2017) indicated that nitrogenous suboxic settings like those of the Peruvian margin upwelling zone can have Mo enrichments similar to those of euxinic deposition (~70 to 100 µg/g), while Hardisty et al. (2018) demonstrated significant overlap in sediment Mo concentrations in oxic environments with *or* without porewater H_2S.

4.2.2. Vanadium

Upper continental crust vanadium (V) concentrations are relatively high (107 µg/g; McLennan, 2001) compared to other redox-sensitive trace metals like Mo, U and Re. Due to its high particle reactivity, riverine particulate V concentrations are high (170 µg/g) compared to its dissolved riverine concentration (15 nM ≈ 0.74 ng/g) (Martin & Meybeck, 1979). Vanadium's seawater concentration is not fully conservative and is relatively low (40 nM ≈ 2.0 ng/g; Collier, 1984) compared to other trace metals and to its riverine flux, therefore sedimentary V content is affected by riverine particulate (detrital) inputs which must be considered in the study of its authigenic enrichment (Emerson & Huested, 1991).

Vanadium is unique in that it has three commonly occurring oxidation states in the marine environment. Under suboxic to weakly anoxic (ferruginous) bottom waters, V(V) as vanadate oxyanions (HVO_4^{2-} or $H_2VO_4^-$) are reduced to V(IV) as the vanadyl oxyanion VO^{2-}

which adsorbs to solid phases. Vanadium enrichment alludes to the presence of H_2S in sediments and bottom waters (Scott, et al., 2017). In euxinic bottom waters, V(IV) is reduced to V(III) which forms a solitary precipitate phase (e.g. V_2O_3 or $V(OH)_3$) (Tribovillard, et al., 2006). Ancient euxinia can be inferred from sediment V concentrations > 320 µg/g based on a compilation of well-characterised Cambrian, Ordovician, Silurian, Carboniferous and Jurassic black shales (Quinby-Hunt & Wilde, 1994).

While some modern sediments exhibit V enrichments up to 229 µg/g (e.g. Cariaco Basin; Calvert & Pedersen, 1993), many ancient organic-rich black shales feature V hyper-enrichments (defined as V > 500 µg/g; Scott, et al., 2017) for which there are no modern analogues. This may indicate that V hyper-enrichments are linked to excess H_2S in bottom waters beyond that which is observed in modern environments (i.e. H_2S > 8 mM; Scott, et al., 2017). Hyper-enrichment may also be linked to the particle reactivity of V; adsorption of V to iron (Fe)- and/or Mn-particulate shuttles is an effective means of transport through the water column to the seafloor (Emerson & Huested, 1991). Additionally, due the association of V with organic matter, hyper-enrichments may occur in environments with extensive organic matter deposition and anoxic to euxinic bottom waters where organic-bound V cannot be oxidized (Quinby-Hunt & Wilde, 1994).

4.2.3. Uranium

Uranium (U) is a redox-sensitive trace metal with a relatively low upper crustal concentration (2.8 µg/g; McLennan, 2001), but a relatively high seawater concentration (13.4 nM ≈ 3.1 ng/g; Tribovillard, et al., 2006). Uranium is supplied to the oceans mainly via riverine input. Sediments deposited under oxic bottom waters retain crustal U concentrations, while authigenic enrichments occur in anoxic organic-rich sediments. Sediment enrichment occurs by diffusion across the sediment–water interface reducing U(VI) (as soluble uranyl oxycarbonate anions $UO_2(CO_3)_3^{4-}$) to U(IV) (as solid uraninite UO_2) (Klinkhammer & Palmer, 1991), adsorption out of solution onto Fe-sulfide surfaces, or becomes complexed with organic matter as mediated by bacterial sulfate reduction processes (Brown, et al., 2018; McManus, et al., 2005; Klinkhammer & Palmer, 1991). Sediment U enrichments greater than 10 µg/g indicate deposition under anoxic conditions (Partin, et al., 2013). Unlike Mo and V, uranium enrichment is not dictated by the presence of H_2S in pore or bottom waters (Partin, et al., 2013)

and U is not readily adsorbed to Fe- or Mn-oxyhydroxide particulates implying that it is not a valid proxy for the presence of H_2S or enhanced particulate activity in the water column. Other factors that influence the enrichment and preservation of U and other trace metals in sediments are sedimentation rate, organic matter accumulation rate, O_2 penetration depth and diagenetic processes or remobilisation under re-oxygenated conditions (Tribovillard, et al., 2006).

4.2.4. Rhenium

Rhenium (Re) is mainly incorporated into suboxic and anoxic sediments and is likely reduced later in the diagenetic sequence than U (Crusius, et al., 1996). Upper crustal Re concentrations are very low (0.4 ng/g; McLennan, 2001) and seawater concentrations are conservative and relatively high (40 pM ≈ 7.2 pg/g; Anbar, et al., 1992), therefore detrital input has minimal influence on Re content in organic-rich sediments. Soluble Re(VII) as a perrhenate oxyanion ReO_4^- in seawater is removed to sediment in the Re(VII) state coupled with an Fe–Mo–S phase (Helz & Dolor, 2012) or reduced to Re(IV) and scavenged onto organic matter in sediments (Selby & Creaser, 2003). Rhenium enrichment is not controlled by the presence of H_2S in pore or bottom waters to the same extent as Mo or V, so it is not a suitable proxy for euxinia (Calvert & Pedersen, 1993). Depositional settings with anoxic pore waters can be deduced by sediment Re concentrations above 5 ng/g (Sheen, et al., 2018). Suboxic sediments can reach concentrations from 25 to 42 ng/g even under nitrogenous (early) suboxia (> 0.2 μM NO_2^-, < 2 μM O_2), and anoxic sediments between 40 and 56 ng/g (Crusius, et al., 1996).

4.2.5. Iron

Iron (Fe) is a major element with average upper continental crust concentrations of 3.50 wt% (McLennan, 2001) mainly in sedimentary and hydrothermal settings as oxide, oxyhydroxide and sulfide compounds (e.g. hematite, Fe_2O_3; goethite, FeOOH; pyrite, FeS_2) and in mafic silicate minerals (e.g. hornblende, $Ca_2(Mg,Fe^{2+})_4(Al,Fe^{3+})(Si_7Al)O_{22}(OH)_2$; biotite, $K(Mg,Fe^{2+})_3AlSi_3O_{10}(OH)_2$). Due to the crystal structures and chemical bonding, Fe in these silicate minerals are considered unreactive to H_2S; Fe in solution, oxides, oxyhydroxides and sulfides are reactive to H_2S (Lyons & Severmann, 2006; Raiswell & Canfield, 1996). Iron is redox-sensitive with two oxidation states: oxidized ferric iron (Fe^{3+}) and reduced ferrous iron (Fe^{2+}). Unlike other redox-sensitive metals discussed in this work which form soluble

oxyanions in oxidizing environments, Fe tends to precipitate solid phases in both oxidizing (e.g. as Fe-oxides) and sulfidic (e.g. as Fe-sulfides) environments; therefore, the modern seawater Fe concentration is very low and varies seasonally and spatially through location and water depth (230–640 pM = 12–35 pg/g; Tagliabue, et al., 2012).

In an oxic water column, Fe(III)-oxyhydroxide particulate phases precipitate and sink from surface waters to the sediment–water interface. If bottom waters remain oxic, the particulates accumulate as a change in redox state is not encountered. If the particulates are transported below the redox chemocline, reductive dissolution of the Fe(III) particulates occurs and any adsorbed metal anions desorb from the particle surface and may be reduced to sediments. However, under reducing conditions, Fe(II) requires H_2S to form solid sulfide phases so if ferruginous anoxia pervades in the sediments and bottom waters, dissolved Fe may return to oxic surface waters and continue to cycle (Poulton & Canfield, 2011). If euxinic conditions are present, H_2S in bottom waters reacts with Fe to form pyrite and other solid Fe–S compounds (Canfield, et al., 1996).

The complex redox cycling of Fe informs the use of the element as a paleoredox indicator. Sediment Fe/Al ratios and C_{org}–S_{TOT}–Fe relationships are used to infer oxic versus euxinic conditions (Lyons & Severmann, 2006; Arthur & Sageman, 1994; Dean & Arthur, 1989). Aluminium is an indicator of local siliciclastic (detrital) sediment flux to a basin (Lyons & Severmann, 2006). In oxic environments, Fe/Al ratios are less than or similar to the average shale ratio of 0.55, while euxinic sediments typically have Fe/Al ratios > 0.55 (Lyons & Severmann, 2006). The increase in Fe/Al ratio from oxic to euxinic sediments stems from the higher siliciclastic input on the oxic shelf (closer to a detrital source; ↑Al) and low pyritization (limited to no H_2S present for compounding with reactive Fe; ↓Fe) versus lower detrital input (↓Al) and increased pyritization (↑Fe) in deeper, more distal euxinic environments where reactive Fe interacts with bottom water H_2S (Lyons & Severmann, 2006). A C_{org}–S_{TOT}–Fe ternary diagram is also employed to differentiate oxic marine sediments which trend along a constant S_{TOT}/C_{org} ratio of ~0.4, from sediments where Fe is bound in pyrite which trend along a constant stoichiometric pyrite S_{TOT}/Fe weight ratio of ~1.15 (Arthur & Sageman, 1994; Dean & Arthur, 1989).

4.2.6. Cadmium and Cd/Mo Covariations

In seawater, Cadmium (Cd) has a low concentration of 0.6 nM (~0.07 ng/g; Boyle, 1992) compared to a continental crust value of 98 ng/g (McLennan, 2001). Unlike previously-discussed trace metals, Cd is not redox-sensitive as it exists in one oxidation state (Cd^{2+}) in the marine environment. Cadmium is strongly associated with marine organic matter due to its role as a micronutrient in phytoplankton (Tribovillard, et al., 2006). In anoxic environments where organic matter is preserved, Cd content will be enriched. Cadmium also has an affinity for forming sulfide compounds (as CdS or coprecipitating with FeS) so in euxinic environments where organic matter is deposited, Cd may be found in association with organic matter or in sulfides (Tribovillard, et al., 2006). Additionally, Cd substitutes for calcium in the apatite structure, therefore phosphatic intervals may exhibit strong Cd enrichment (Tribovillard, et al., 2006, and references therein).

The Cd–Mo covariation (**Figure 5**) presented in Sweere et al. (2016) is used to distinguish upwelling environments from silled or strongly restricted environments recorded in organic-rich sediments or rocks. These "end-member" environments are thought to be distinguished by the relative importance of the productivity (↑Cd/Mo) versus preservation (↓Cd/Mo) enrichment mechanisms for organic matter and their influence on Cd/Mo ratios. Sweere et al. (2016) compiled geochemical data from several modern upwelling zones (Namibian and Peruvian margins, Gulf of California and the Arabian Sea) and restricted basins (the Black Sea, Cariaco Basin, Saanich Inlet and Mediterranean Sea). Cadmium was more enriched in the productive upwelling zones (~0.4 to 80 µg/g) than the restricted basins (~0.15 to 15 µg/g). Molybdenum was slightly more enriched in the restricted environments (~1 to 300 µg/g) than the upwelling zones (~1 to 100 µg/g), but there was significant overlap in concentrations between environments. These trends are reflected by higher Cd/Mo ratios in the upwelling zone than the restricted basins. From their study, Sweere et al. (2016) define an empirical Cd/Mo cut-off between these environments, where Cd/Mo ratios > 0.1 indicate upwelling, and < 0.1 indicate restriction. Recent paleoenvironmental application of the Cd/Mo covariation technique (McArthur, 2019) is used to argue that the Toarcian black shales of Europe were a response to restriction (low Cd/Mo trend) of the Cleveland Basin (Tethys Ocean), rather than global ocean anoxia.

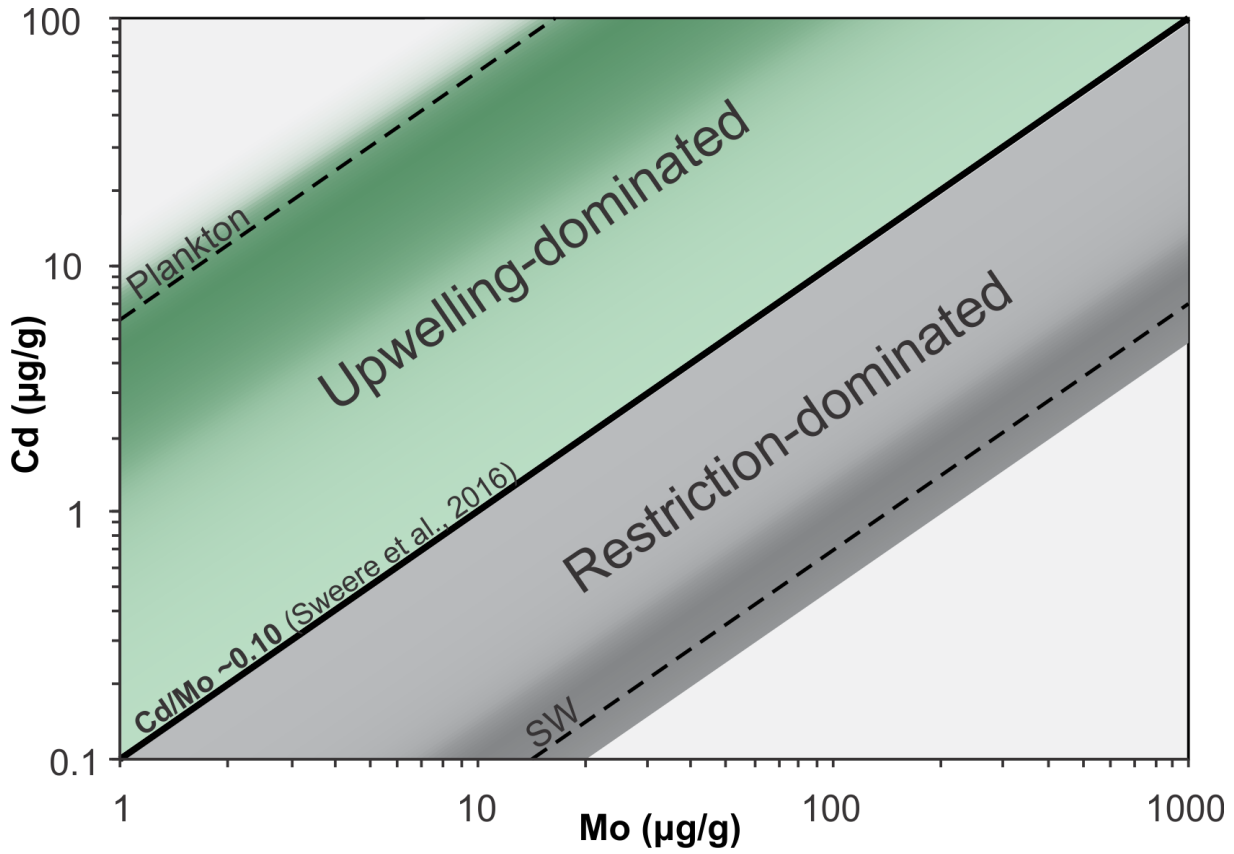

Figure 5. **Cd/Mo Covariation Diagram.** Cadmium–Mo covariation modified from Sweere et al. (2016) indicating fields for upwelling zone and restricted basin "end-member" environments. Sweere et al. (2016) define an empirical cut-off for the Cd/Mo ratio of 0.1 to distinguish between the environments. Also noted are the seawater (SW) Cd/Mo weight ratio (~0.007; Tribovillard, et al., 2006) and mean plankton Cd/Mo ratio (6.0; Brumsack, 1986).

4.2.7. Mo/U Covariation

Covariation diagrams of enrichment factors (EF) for Mo versus U (Mo_{EF}/U_{EF}; **Figure 6**) can be used to determine the mechanism of trace metal enrichments within a depositional basin, and basin hydrography (Algeo & Tribovillard, 2009). Enrichment factors (**Equation 2**) correct for detrital content of the trace metal, *X*, in a sample versus a standard material like the upper continental crust or average shale.

(2)
$$X_{EF} = \frac{(X/Al)_{sample}}{(X/Al)_{standard}}$$

Algeo and Tribovillard (2009) suggest three mechanisms that can cause variations in Mo_{EF}/U_{EF} ratios of marine sediments: (1) redox variations from oxic→euxinic across a basin or depositional period; (2) Fe–Mn particulate shuttles delivering excess Mo, but not U to the

sediment–water interface; and (3) evolving aqueous chemistry from seawater depletion of trace metals during persistent anoxia or euxinia with limited repletion after trace metals are removed to sediments. The first mechanism is typical of open-ocean basins and upwelling zones (e.g. Eastern Tropical Pacific) whereas the second reflects weakly-restricted basins with euxinic bottom waters and relatively rapid deep-water mass replenishment (e.g. Cariaco Basin). The third mechanism is typical of strongly restricted basins (e.g. Black Sea), which have euxinic bottom waters resulting in an initially enhanced drawdown of trace metals into sediments, but with little repletion of the water mass resulting in diminished bottom water trace metal concentrations at steady-state conditions. Because the sequestration of Mo into euxinic sediments is more efficient than U, this leads to a gradual decrease in sediment Mo/U as the local deep waters become severely depleted in Mo, and moderately depleted in U.

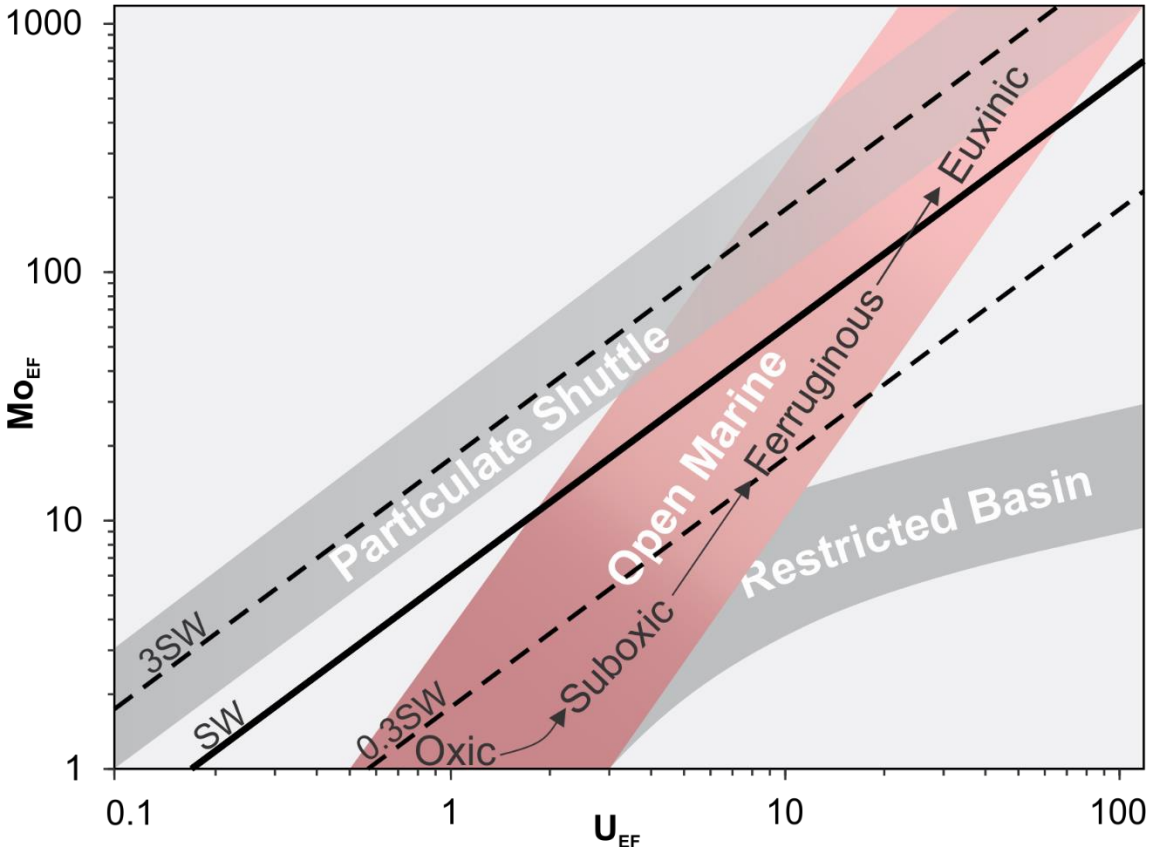

Figure 6. **Mo/U Covariation Diagram.** Covariation of Mo and U enrichment factors (EFs) modified from Algeo and Tribovillard (2009). Inference of basin hydrography (open ocean or restricted) and additional enrichment mechanisms (Fe–Mn particulate shuttling) can be made using the diagram. Seawater Mo/U weight ratio is noted (3.1; Tribovillard et al., 2006), as are the general EF fields which record euxinic, anoxic/non-sulfidic and suboxic conditions.

4.2.8. Re/Mo Covariation

The Re/Mo ratio is a tool to determine depositional redox conditions as both Re and Mo are conservative and have high seawater-to-crust ratios (Crusius et al., 1996). This trace metal covariation is specifically useful in distinguishing between suboxic/ferruginous and euxinic environments (Turgeon & Brumsack, 2006; Crusius, et al., 1996). Crusius et al. (1996) report modern Re and Mo sediment concentrations at four sites (Japan margin, Pakistan oxygen minimum zone [Arabian Sea], Saanich Inlet [British Columbia], and the Black Sea), the results of which are summarized by a Re–Mo covariation diagram (**Figure 7)**. Sediments deposited under euxinic bottom-waters are typically enriched with both Re and Mo (up to 50 ng/g and 120 µg/g, respectively), and trend along the modern seawater Re/Mo ratio (0.73×10^{-3}). Suboxic and anoxic (ferruginous) environments are less conducive to Mo removal, therefore enrichment in Re outweighs Mo, leading to Re/Mo ratios along a trend up to 15×10^{-3} (Turgeon and Brumsack, 2006).

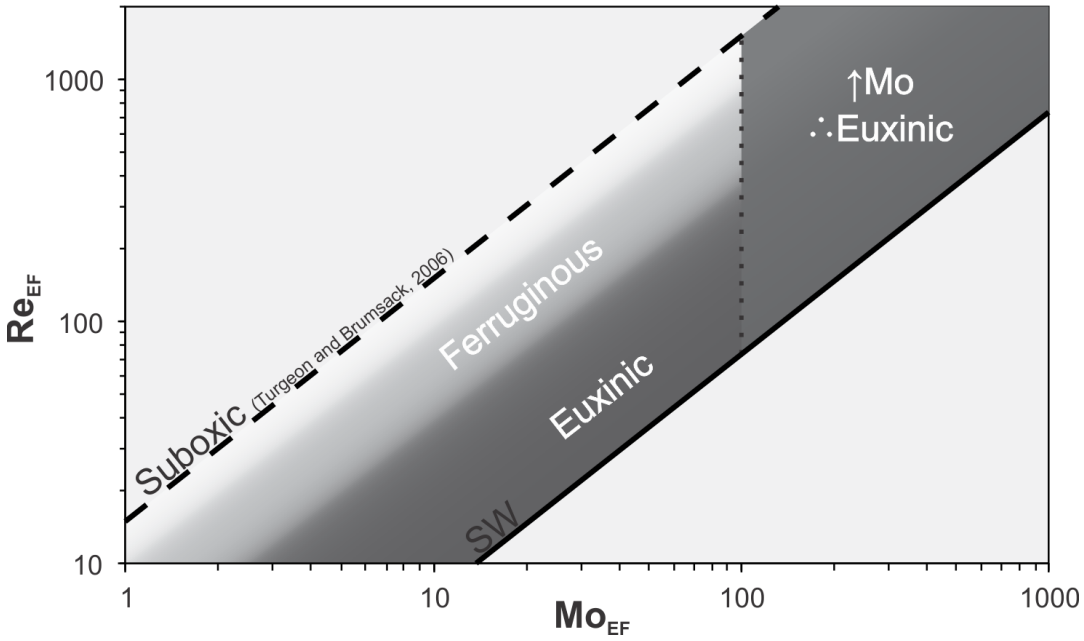

Figure 7. **Re/Mo Covariation Diagram.** Re/Mo covariation diagram with modern redox environment trends (Crusius, et al., 1996). Dashed line is suboxic Re/Mo ratio (~15) trend after Turgeon and Brumsack (2006). Solid black line is modern seawater (SW) Re/Mo ratio (0.73×10^{-3}; Crusius, et al., 1996). Note that at elevated Mo content (here Mo_{EF} > ~100), the environment is assumed euxinic generally close to SW ratio.

4.2.9. Mercury

In nature, mercury (Hg) is delivered to the atmosphere as gaseous elemental Hg^0 (> 95%), oxidized inorganic Hg^{2+} (< 5%) through quiescent volcanic outgassing (primary source; 46 tonnes annually) and volatilization of biomass-Hg and Hg-bearing rocks and soils (e.g. forest fires, subaerial weathering; secondary sources; 1.1 kilotonnes annually[1]) (Fitzgerald & Lamborg, 2005; Pyle & Mather, 2003). The atmospheric residence time of Hg^0 is from several months to 2 years (Lindqvist & Rodhe, 1985), allowing for distribution on a global scale. By contrast, reactive atmospheric Hg (particulates and compounds carrying Hg^{2+}) have a much shorter residence time from a few days to weeks (Lindqvist & Rodhe, 1985). Elemental Hg is distributed evenly across the planet and can be converted to Hg^{2+} through oxidation processes, while reactive atmospheric Hg^{2+} expelled during volcanism is deposited at local scales. During periods of elevated volcanic activity, there is a ~100-fold increase in atmospheric Hg flux from the release of volcanic gases (up to 4.6 kilotonnes annually) based on modern eruptions (Fitzgerald & Lamborg, 2005).

Mercury enters the ocean as Hg^{2+} and is reintroduced into the atmosphere as Hg^0 through exchange at the atmosphere–ocean interface (net Hg flux to oceans of 1000 tonnes annually; Driscoll, et al., 2013). Hydrothermal vents along submarine tectonic zones (260–360 tonnes annually; Fitzgerald & Lamborg, 2005) and riverine input (60 tonnes annually[1]; Mason, et al., 1994) are additional pathways through which Hg enters the ocean. Removal of Hg^{2+} from the water column occurs through organic and inorganic mechanisms. When organic substrates are present in bottom waters or sediments, Hg^{2+} has a strong affinity to bind with organic thiols (e.g. Mishra, et al., 2017). Direct inorganic deposition of Hg into sediments occurs when the chalcophilic Hg^{2+} precipitates as HgS or coprecipitates with metal sulfides (e.g. pyrite) under anoxic conditions (Mishra, et al., 2017). Therefore, long term removal of Hg from the water column into sediments occurs via complexation with thiol groups on the cell surfaces of organic matter and precipitation of Hg–S phases.

Post-depositional processes affect the Hg content and solid phases preserved in sediment. Encountering oxic conditions in sediments oxidizes Hg-sulfides, but the resulting

[1] Pre-anthropogenic flux

pore water Hg^{2+} likely re-complexes with insoluble humic substances *in situ* in organic-rich environments (Beldowski & Pempkowiak, 2009). Anoxic diagenesis transforms thiolated Hg associated with organic matter into the insoluble sulfide HgS; however, highly sulfidic conditions can dissolve HgS to form soluble polysulfides which may be recaptured by suitable organic compounds, migrate through the sediment column and reprecipitate under anoxic (non-hyper-sulfidic) conditions, or reintroduced to the water column by diffusion at the sediment–water interface (Beldowski & Pempkowiak, 2009; Paquette & Helz, 1995).

Recently, sedimentary Hg from organic-rich black shales was suggested as a proxy for past intensified volcanic activity (e.g. Grasby, et al., 2019; Them II, et al., 2019; Percival, et al., 2015; Sanei, et al., 2012). Based on the modern 100-fold increase in Hg volcanic source flux from dormant to active periods (Fitzgerald & Lamborg, 2005), increased Hg concentrations in sediments are likely linked to increased volcanic activity. Ancient massive volcanism is associated with Large Igneous Province (LIP) emplacement, which has occurred episodically over periods in Earth's history (Prokoph, et al., 2004). Periods of LIP emplacement last from 1 to 5 Myr with 10s to 100s of massive eruptions or intrusions occurring during that period (Bryan, et al., 2010), therefore these periods should be recorded by the preservation of elevated Hg concentrations in sediments.

Because Hg integration into sediment is primarily controlled by the host phase, normalisation to that host phase must be completed to avoid false positives with respect to enhanced volcanogenic Hg fluxes. To avoid deceitfully high Hg concentrations due to increased organic matter deposition, Them II et al. (2019) and Percival et al. (2015) normalise Hg to C_{org}. Sanei et al. (2012) acknowledge the likely incorporation of large amounts of Hg in authigenic pyrite under euxinic conditions, but only normalised Hg to C_{org}. Shen et al. (2019) compare Hg to C_{org} and S_{TOT} and find they are poorly ($r^2 < 0.01$) and well ($r^2 > 0.80$) correlated, respectively. Additionally, energy-dispersive x-ray spectroscopy was used to further verify that pyrite, and not organic matter, was the host phase for Hg in their samples. Sediment Hg may also be associated with clay or Fe-oxide phases, so an Al or Fe normalisation is suggested (Grasby, et al., 2019). Since sediment Hg retention is not fully understood, examination of all potential host phases may help to reduce the possibility of false positives.

4.3. Mass Balance Models

Trace metal seawater concentrations are regulated by source fluxes from rivers and seafloor hydrothermal activity and sink fluxes to oxic, suboxic and anoxic/euxinic seafloor sediments. Trace metals like Re and Mo are removed most efficiently to the anoxic/euxinic sinks, as indicated by higher trace metal burial rates. Therefore, an expansion of anoxic/euxinic areas will result in a drawdown of metals from seawater, thereby depleting the global seawater metal reservoir over time. Mass balance models take advantage of the source–seawater–sink relationship to characterise ancient environments by their seafloor anoxic or euxinic sink areas.

The redox sensitive trace metals Re and Mo are conservative in seawater with residence times of 130 and 440 thousand years (kyr), respectively (Miller, et al., 2011) for the modern ocean—greater than average ocean mixing times (1 to 2 kyr)—making them ideal candidates for modelling global ocean redox conditions. In non-restricted settings where ocean circulation is not inhibited, or is only weakly restricted, these trace metals can be used to determine the global areal extent of seafloor anoxia by mass balance models. Sheen et al. (2018) developed a model for general anoxic (ferruginous + euxinic) seafloor area using Re, and Reinhard et al. (2013) for euxinic seafloor area using Mo. The models are first-order in that sediment metal enrichments are assumed to scale directly with seawater metal reservoir size. These models are solved to determine the authigenic sediment enrichments at a given anoxic or euxinic seafloor area following **Equations 3a** to **3c**, which are fully derived in Sheen et al. (2018) and Reinhard et al. (2013).

(3a) $$[Me]' = [Me]_M \frac{F_{in}}{\sum A_i b_i}$$

(3b) $$b'_{ae} = b_{ae} \frac{[Me]'}{[Me]_M}$$

(3c) $$[Me]_{auth} = \frac{b'_{ae}}{BMAR}$$

Where:

Me = metal (Re or Mo)
[Me]' = seawater metal concentration at a new steady state
$[Me]_M$ = modern seawater metal concentration
F_{in} = input flux

A_i = area of seafloor covered by a given sink (i)

b_i = characteristic metal burial rate for a given sink (i)

b_{ae}' = metal burial rate in the anoxic or euxinic sink at a new steady state

b_{ae} = metal burial rate in the modern anoxic or euxinic sink

$[Me]_{auth}$ = authigenic metal enrichment in anoxic or euxinic sediments

BMAR = bulk mass accumulation rate

These models assume riverine input of each element as the dominant source to the ocean, as observed in modern oceans (**Table 3**, following page). Sinks included in the models are oxic, suboxic and anoxic sediments (for Re), or oxic, suboxic, and euxinic sediments (for Mo), with modern environments used in both cases to determine fluxes for sources and sinks (**Table 3**, following page). Additionally, scaling algorithms for b_{ae}' were considered to account for decreasing burial rate due to lower mass accumulation rates as anoxic/euxinic seafloor area expands from continental margins into deeper waters farther from the continents. Reinhard et al. (2013) applied a fourth-order polynomial fit to approximate ocean bathymetry, and Sheen et al. (2018) expanded on this by calibrating burial rates to the eTOPO ocean bathymetry database (Amante & Eakins, 2009) which allowed for fine-tuning of burial rate with depth as anoxic expansion occurs. Bulk mass accumulation rates in the published models are those recorded in the Cariaco Basin (largest modern anoxic basin with only weak restriction from the open ocean) of 0.01 g cm^{-2} yr^{-1}. In addition to scaling using the polynomial or bathymetric functions, b_{ae}' scales proportionately to the global reservoir of Re or Mo by **Equation 3b.**

To perform these models, data is filtered to ensure only samples deposited under anoxic or euxinic settings are used. Sheen et al. (2018) apply filters of Fe/Al > 0.5 and C_{org} > 0.4 wt% to infer anoxic samples for Re; Reinhard et al. (2013) apply filters of Fe, Al and C_{org} > 1 wt%, Fe/Al > 0.5, and Fe_{py}/Fe_{HR} (py = pyrite; HR = highly reactive) > 0.7 or degree of pyritization (DOP) > 0.6 to infer euxinic samples for Mo.

Table 3. **Summary of sink parameters for Re and Mo mass balance models.** Percent area of the modern seafloor ($\%A_{SF}$) for oxia and anoxia/euxinia are taken from best estimates, while suboxia is calculated based on the estimated areas of oxic and anoxic/euxinic seafloor to achieve mass balance. Note that the sum of oxic, suboxic and anoxic/euxinic seafloor sinks is not 100%, due to an ~11% area of the authigenically neutral seafloor (area with no drawdown of Re or Mo from seawater). The Re and Mo flux (F) is the quantity of mass flux into each sink from rivers. The percent source flux ($\%F_{in}$) is the relative amount of the total riverine flux into a given sink. The ratio of percent source flux to the area of seafloor for a given sink (F_{in}/A_{SF}, in %) illustrates that the smallest sink areas (anoxic/euxinic) incorporate the highest Re and Mo masses per unit area. Characteristic burial rates for each sink (b_i) are noted.

			Re(1)				**Mo**(2)			
		$\%A_{SF}$	***F*** (× 10^5 mol/yr)	**$\%F_{in}$**	**F_{in}/A_{SF}**	***b_i*** (ng/ cm^2/yr)	***F*** (× 10^8 mol/yr)	**$\%F_{in}$**	**F_{in}/A_{SF}**	***b_i*** (µg/ cm^2/yr)
Source (Rivers)			4.29				3.00			
Sinks	Oxic	83.89	0.26	6.1	0.07	0.0016	0.87	29	0.3	0.00275
	Suboxic	4.67(1), 1.92(2)	3.75	87.4	18.7	0.415	1.94	64.7	33.7	0.27
	Anoxic	0.11	0.28	6.5	59.1	1.339				
	Euxinic						0.19	6.3	57.3	2

(1) Sheen et al. (2018) (2) Reinhard et al. (2013)

5. Methods

Samples were taken from a core from northeastern British Columbia (*c-B6-A/94-B-8*) during three collection periods: February 2016, January 2018, and January 2019. The core measures 45.7 meters and covers stratigraphy from the uppermost Pardonet Formation, Gordondale Member, PCS, and lowermost upper Fernie Formation shales. Lithology varies through the core, including dolomites (Pardonet), turbidite and/or debris flow sequences (Gordondale), siltstones (Gordondale, PCS), volcanic ash beds (Gordondale, PCS), grey shales (upper Fernie Formation shales), and black shales (Gordondale, PCS). The Gordondale Member in its type section contains an upper, middle, and lower subunit. The middle unit is not represented in all sections or is very thin (< 2 m; Asgar-Deen, et al., 2004). The middle unit was not detected in the study core section; therefore, the Gordondale Member in the core is subdivided into Lower and Upper Subunits based on major and trace element geochemistry. The Gordondale–PCS boundary is defined by a sharp transition from calcareous (Gordondale) to non-calcareous (PCS) deposition. The PCS as described in the study core is analogous to the PCS-B of Riediger (2002), while the Gordondale Member Upper Subunit is equivalent to Riediger's PCS-A. The primary target for geochemical analyses in this study are the black shales of the Gordondale Member and PCS.

5.1. Sample Collection and Preparation

5.1.1. 2016 Collection

Samples from February 2016 were collected for corporate research (Progress Energy Canada Ltd., now Petronas Canada) at Weatherford Laboratories Canada Ltd. (Weatherford Labs; Calgary, AB) prior to this thesis project. Forty-five horizontal plugs were acquired at approximately 1 m intervals with geophysical, geochemical, and mineralogical analyses completed by Weatherford (spectral core gamma, source rock analysis) and Argile Analytica (X-ray diffraction; XRD). Sampling captured a wide range of lithologies including fissile upper Fernie Formation shales (n = 6), grey to black organic-rich shales with and without calcareous fossil material (PCS, n = 16; Gordondale, n = 13), turbidites (Gordondale, n = 7), displacive fibrous calcite fracture zones (e.g. Riediger and Coniglio, 1992; Gordondale, n = 1) and Pardonet Formation dolomites (n = 2). The samples of greatest interest in this project are the

grey to black organic-rich shales without fossils or veins to best interpret the depositional environment (authigenic mineral phases, sulfide minerals, and bulk organic matter), rather than the fossil, detrital (turbidite), or diagenetic (calcite vein) signatures. Before sampling, the core was subject to spectral gamma testing; following sampling the core was slabbed (one-third and two-thirds), surface cleaned and photographed under white light (Weatherford Laboratories Canada Ltd., 2017).

5.1.2. 2018 and 2019 Collection

Core sampling occurred over three days in January 2018 at Weatherford Labs in Calgary, Alberta. These samples were collected for multiple geochemical analyses at the Metal Isotope Geochemistry Laboratory (MIGL) and Environmental Isotope Laboratory (EIL) of the University of Waterloo (UW), the Agriculture and Food Laboratory (AFL) of the University of Guelph, the Geochemistry of Ancient and Modern Environmental Systems Laboratory (GAMES Lab) of the College of Charleston, and Activation Laboratories (Actlabs; Ancaster, ON). Previous core descriptions (Moslow, 2016) and direct observations were used as the basis for sampling. Forty-six samples were collected at an average of approximately one sample per 1 m ("low stratigraphic resolution"), most of which were black shales from the Gordondale and PCS (n = 18 and 16, respectively). The remaining samples were volcanic ash beds (n = 1 and 2, respectively), siltstones (n = 1 and 1, respectively), and turbidites (n = 2 and 0, respectively) from the Gordondale and PCS, as well as dolomites from the Pardonet Formation (n = 3), and grey shales of the upper Fernie Formation (n = 2). Several features within the core were avoided to ensure that the primary geochemical signal was that of syn-depositional to earliest diagenetic processes, rather than those of secondary environmental processes; these included macroscopic pyrite nodules and calcite veins and/or veinlets (later-stage diagenesis), fossils, and bedding contacts (intermixing). Samples were removed by stainless steel chisel, photographed, bagged, catalogued, and transported to Waterloo.

Another sample set for geochemical analyses was collected over two days in January 2019 at the Alberta Energy Regulator Core Research Centre in Calgary, Alberta. These samples were collected from a portion of the core (26.3 m interval) based on the results of the 2018 geochemical analyses at an average of approximately one sample per 40 cm ("high

stratigraphic resolution"). The sampling procedure from 2018 was followed, however, only black shale samples of the Gordondale and PCS were taken (n = 55 and 7, respectively).

5.1.3. Physical Sample Preparation (2018/2019)

Physical preparation of samples collected in January 2018 and 2019 occurred in the Hard Rock Laboratory at UW. Samples were trimmed by a diamond rock trim saw to remove unwanted material; i.e. chisel marks, core paint, or sedimentary features (e.g. fossils, calcite veins, macroscopic pyrite) that would interfere with efforts to infer depositional conditions from the black shale geochemistry. Trimmed samples were manually crushed with a rubber mallet, or, when necessary for samples with high physical competency, with a metal rock hammer wrapped in several layers of duct tape to avoid metal contact with the sample. Sample chips were powdered in a Retsch automated ball mill with agate grinding jars. Sample powder was stored in 20 ml low-density polyethylene (LDPE) vials.

From each powdered sample, five subsamples were taken for analysis of (1) multi-element concentrations (100 mg; MIGL), (2) total carbon, C_{org}, and C_{inorg} contents (1-5 g; AFL), (3) C_{org} isotope composition (1 g; EIL), (4) sediment mercury (Hg) content (1 g; GAMES Lab), and (5) total sulfur (S_{TOT}) content (1 g, Actlabs). Subsample sets 1 and 3 were retained for analysis at UW, while subsample sets 2, 4 and 5 were shipped to their respective laboratories for further preparation and analysis.

5.2. Whole Rock Multi-Element Analysis

5.2.1. Sample Digestion and Dilution

Whole rock subsamples for multi-element analysis were weighed (m_{wr}, grams), then ashed in ceramic crucibles within a muffle furnace at 550°C for 24 hours to oxidize organic matter. Ashed subsamples were chemically prepared for analysis at the MIGL in a class 10 000 metal-free cleanroom. Fisher Scientific TraceMetal™ Grade nitric acid (HNO_3) at 70% w/w, hydrochloric acid (HCl) at 35% w/w and hydrofluoric acid (HF) at 50% w/w were used. Acid concentrations are noted in the procedure only if they differ from the Fisher stocks. Digestions were completed under class 10 to 100 laminar-flow fume hoods within the cleanroom.

In the balance room within the cleanroom, ashed material was transferred from the ceramic crucible to a 22 ml Teflon beaker and wet with 10 drops of Milli-Q ultrapure water to

avoid airborne sample powder within the main cleanroom. Wet sample material was digested in 2.5 ml HNO_3 and 0.5 ml HF for 48 hours at 110°C. After the digestion period, the Teflon beaker lids were removed, and digestions were left on the hot plate at 110°C to evaporate through the day until just dry. A second acid digestion in 4 ml *aqua regia* solution—3 ml HCl and 1 ml HNO_3—was prepared and set at 110°C for 48 hours. The evaporation process was completed following the *aqua regia* digestion period. A final digestion in 2 ml 35% w/w HCl at 110°C for 24 hours was completed, followed by evaporation. Dry residues were dissolved in 6 ml of 6 mol/l HCl and 3 drops of 0.5% v/v HF, then transferred from the Teflon beakers to 15 ml LDPE vials. Mass of the LDPE stock solutions (m_s) were recorded in grams.

Sample aliquots were produced from the stock solutions at dilution factors (DF) of approximately 6000 (for major and most trace elements) and 400 (for Cd, Re and heavy rare earth elements). The estimated aliquot volume (V_a, ml) required for the desired DF (DF_d) was calculated by **Equation 4.**

(4)
$$V_a = \left({10g}/{1.11g/ml}\right)\frac{m_s}{m_{wr}\times DF_d}$$

The estimated volume is corrected by the anticipated mass of the final aliquot solution (10 g) and the approximate density of the sample solution (1.11 g/ml). The calculated V_a was pipetted from the stock solution to a 7 ml Teflon beaker. The aliquots were weighed (m_a, grams) and evaporated at 110°C to dryness. Dry residues were dissolved in 1 ml of 2% v/v HNO_3, then evaporated to remove all traces of HCl. The final residues were transferred to 15 ml centrifuge tubes in ~10 ml of 2% v/v HNO_3 and 2 drops of 0.5% v/v HF. The final mass of the analyte solutions (m_f, grams) were weighed and recorded. Analyte solutions were stored for up to 20 days before analysis. The true DF (DF_t) for each analyte solution was calculated by **Equation 5**.

(5)
$$DF_t = \frac{m_s\times m_f}{m_{wr}\times m_a}$$

5.2.2. Sample Analysis

Inorganic element concentrations of the diluted samples were measured at MIGL on an Agilent 8800 triple-quadrupole inductively coupled plasma mass spectrometer (QQQ-ICP-MS). Two analytical runs were completed, one for each of the sample dilutions. The more

dilute digestions (DF = 6000) were run first for major and most trace elements (see **Table 4**). The more concentrated digestions (DF = 400) were run the following day for the heavy rare earth elements (HREE), Cd and Re (see **Table 4**). The order of the analyses from high to low DF is necessary to avoid element build up or memory effects in the QQQ-ICP-MS instrument during the high concentration run.

Table 4. Elements analysed by QQQ-ICP-MS at the MIGL. Major elements are those with average upper continental crust concentrations (UCC; McLennan, 2001) > 1 wt%, minor elements are those with UCC between 0.1 and 1 wt%, and trace elements are those with UCC < 0.1 wt%. The elements discussed in this work are presented; none lie within the "minor element" category. Major elements in this thesis are recorded in weight percent (wt%) and trace elements in µg/g, except for Re (ng/g). The dilution factor (DF) that was used to make analytes for a given element analysis are listed, where 6000 is more dilute and 400 is more concentrated.

	DF = 6000	DF = 400
Major	**Al**, **P**, **Ca**, **Fe**	n/a
Trace	**V**, **Mo**, **U**	**Cd**, **Re**

These analyses were performed in helium (He) mode, meaning that He was the carrier gas introducing sample solutions into the QQQ-ICP-MS system. Internal standard elements scandium (^{45}Sc), germanium (^{72}Ge), indium (^{115}In) and bismuth (^{209}Bi) were continuously analysed to correct for instrument drift. These elements were chosen to bracket the entire range of element masses sought in the analysis. However, some of the major elements (^{27}Al, ^{31}P and ^{44}Ca) have masses lighter than Sc, while uranium (^{238}U) is heavier than Bi. Calibration standards were diluted at factors of 10 to 200 000 from stock solutions containing ~20 to 200 µg/g of the desired major elements, and ~1 to 2 µg/g of the desired trace metals. The calibration standards were analysed at the beginning of each analytical run and are used to correct for concentration offset between the known (calculated) and measured values for the calibration standards.

Results of the QQQ-ICP-MS analysis were transmitted from the instrument to the accompanying workstation in the Agilent MassHunter software package. Measured element concentrations (C_m) are stated in parts-per-billion (ppb) w/w (ng/g) from the dilute solution. True whole rock element concentrations (C_t) were calculated by **Equation 6**.

(6) $$C_t = C_m \times DF_t$$

Major element concentrations were converted from ppb to weight percent (wt%; **Equation 7a**), and trace elements (excluding Re) were converted from ppb (ng/g) to parts-per-million (ppm, µg/g; **Equation 7b**).

(7a) $$C_f\ (\text{wt\%}) = C_t \times 10^{-7}$$

(7b) $$C_f\ (\text{ppm}) = C_t \times 10^{-3}$$

Where C_f is the final converted element concentration, and 10^{-7} and 10^{-3} are used to convert from ppb to percent and ppm, respectively.

5.2.3. Quality Control

From the analyses, element concentrations are reported with a percent relative standard deviation (RSD), based on three measurements taken during an analytical run. Most individual samples had RSDs less than 5% for all elements analysed. Some elements were analysed more precisely than others; of 108 samples, P, Ca, and Fe had 106 with RSDs less than 5%, Mo had 93, U had 89, Al had 88, and V had 86, Re had 71, and Cd had 65. However, for those samples/elements which exceeded 5% RSD, the majority still remained below a 10% RSD.

Along with core samples, three United States Geological Survey (USGS) black shale standards (SBC–1, SDO–1, and SGR–1b) were digested and diluted following the same procedure as core samples, and analysed at the beginning, midpoint and end of the analytical run. Certified standard values are reported by Wilson (2012; SBC-1), Smith (1991; SDO-1), and Wilson (2014; SGR-1b), except for Re concentrations which were reported by Yin et al. (2017; SGR-1b) and Li and Yin (2019; SBC-1). Results of the standard analysis were used to verify instrument accuracy based on the certified standard concentrations (C_c) for each element and monitor instrument drift by comparing reported concentrations from each standard value across the analytical run. Most elements gave standard percent recovery (**Equation 8**) within 100 +9/–15% based on the C_m of the standard compared to the C_c.

(8) $$\text{Standard \% Recovery} = \frac{C_m}{C_c} \times 100\%$$

Several total procedural blanks were produced with the sample set. Blank analytes are used to monitor for contamination that could have occurred during the digestion, dilution, or

measurement phase of the procedure. Total procedural blank solutions should have element concentrations near or below the detection limit of the instrument (i.e. concentrations approaching zero), however a sample percent blank (% Blank; **Equation 9**) for each element in each sample of less than 10^{-3} was considered satisfactory.

(9) $$\% \text{ Blank} = \frac{C_{m,blank} m_{a,blank}}{C_t m_{wr}} \times 100\%$$

Where $C_{m,blank}$ and $m_{a,blank}$ are the measured concentration and mass of the blank analyte solution.

Replicates of several whole rock samples were prepared along with the main sample set using the same chemical and analytical procedures. These were used to verify the precision of the measurements based on the relative standard deviations (RSD) between the concentrations of each element from the main and replicate samples (**Equation 10**).

(10) $$\text{Replicate RSD} = \frac{s}{\bar{x}} \times 100\%$$

Where s and $\bar{x}$ are the sample standard deviation and mean, respectively, between the main and replicate samples. Precision of the measurement was considered excellent when replicate RSDs were less than 5%, and satisfactory between 5% and 10%. **Equation 10** was also applied to USGS standards, which were measured multiple times during analytical runs. Of all replications, 37% were considered excellent, while 18% were considered satisfactory, therefore most samples fell below a replicate RSD of 10%.

5.3. Organic Carbon Isotope Analysis

5.3.1. Sample Acid Washing

Subsamples for C_{org} isotope analysis were chemically prepared in a general wet geochemistry laboratory at the EIL. These subsamples were bathed in approximately 5 ml of 5% to 10% reagent grade HCl at 50°C for several hours to remove C_{inorg} (as carbonate, CO_3^{2-}). Solutions were pH-tested to ensure that the alkaline carbonate had been sufficiently removed. Acid was siphoned from the sample vial with a pumping tube with glass tip, and four rinses with NanoPure water were completed across several hours to remove all acid. Note that due to their high C_{org} content, approximately half of the samples were hydrophobic (did not mix or settle within the vial) and required delicate siphoning. After the final water rinse and siphon,

the sample vials were placed on a warm surface for 48 hours to dry. Dried sample material formed a puck in the sample vials, which was re-powdered and re-mixed. Between 1 and 10 mg of the acid-washed samples were weighed, placed in a foil cup and stored in a sampling tray until analysed.

5.3.2. Sample Analysis

Sample analysis for C_{org} isotope composition ($\delta^{13}C$) was completed at the EIL on a Costech Instruments 4010 Elemental Analyzer combustion chamber to volatilize sample material, coupled with a Thermo-Finnigan Delta Plus XL continuous-flow isotope ratio mass spectrometer to measure $\delta^{13}C$. Carbon isotope ratios are reported as per mil (‰) values against a standard reference material with precision of ± 0.2‰, calculated by **Equation 1**. The EIL uses several international and in-house standard reference materials that are calibrated to the primary carbon isotope scale anchored by Pee Dee Belemnite (PDB).

5.4. External Laboratory Procedures

Samples collected and analysed in 2016 by Weatherford and Argile Analytica, and subsamples of 2018 and 2019 samples that were sent to the AFL, Actlabs and GAMES Laboratory were not prepared or analysed by the author.

5.4.1. Programmed Pyrolysis (Weatherford Labs)

Weatherford Labs completed programmed pyrolysis on 45 horizontal plugs from the 2016 sample set using their proprietary Source Rock Analyzer Plus TOC instrument to obtain C_{org} content, free hydrocarbon content (S_1), source potential (S_2), carbon dioxide yield (S_3), and thermal maturity (Tmax). Whole rock samples are powdered and passed through a 250 µm mesh sieve prior to analysis. Programmed pyrolysis (stage temperature heating) of sample powders volatilizes hydrocarbon- and oxygen-bearing compounds which are directly measured in the instrument. Further calculations can be made from measured values, the most useful for this project being the hydrogen index (HI) and oxygen index (OI). The HI is used to determine organic matter source (marine or terrestrial) and a Van Krevelen diagram (HI versus OI) is used to determine kerogen type. The HI and OI are calculated by **Equations 11** and **Equation 12**, respectively (Weatherford Laboratories Canada Ltd., 2017).

(11) $$HI = 100 \times \frac{S_2}{C_{org}}$$

(12) $$OI = 100 \times \frac{S_3}{C_{org}}$$

5.4.2. X-ray Diffraction (Argile Analytica)

Bulk and clay mineralogy were determined for 45 horizontal plug samples from the 2016 sample set using XRD techniques at Argile Analytica's laboratory on a Rigaku Miniflex XRD instrument with copper x-ray tube. For bulk mineralogy, 1.5 g of sample material was powdered in a Retsch ball mill for 3 minutes, and if necessary was further ground in an agate mortar to homogenize grain size. Sample powders were packed in the sample holders to avoid preferential orientation of mineral grains and scanned with angles of incidence from 2° to 30°. For clay mineralogy (particles < 2 µm), material was wet-ground in an agate mortar with aqueous sodium bicarbonate and transferred to a glass tube. The material in the glass tube was sonicated and centrifuged to separate clays from the bulk material by sedimentation. The supernatant containing the clay material was transferred to a plastic tube and rapidly centrifuged for 20 minutes to allow clays to settle. The supernatant was poured off and the remaining clay material packed into sample holders to air-dry at room temperature. Scans of dry mounts occurred at incident angles from 1.5° to 17.5°. Swelling clays (e.g. smectite group) require further treatment for analysis; the same samples were placed in a glycol chamber at 75°C for 4 hours to expand the swelling clays. Finally, samples were heated at 550°C for 1 hour to differentiate further between swelling and non-swelling clays, as this dehydrates (collapses) swelling clays while the structural integrity remains intact in non-swelling clays (e.g. illite group). This process will also destroy some clays (e.g. kaolinite). Method accuracy was validated through analysis of a sample with known weights of kaolinite (10 wt%), corundum (20 wt%), quartz (30 wt%) and calcite (40 wt%); measured values were 9.5 wt%, 20.9 wt%, 30.3 wt% and 39.3 wt%, respectively (Stefani, 2017).

5.4.3. Carbon Content (Agriculture and Food Laboratory)

Carbon analysis was completed at the AFL on the 2018/2019 sample sets. TOC is measured indirectly by subtracting C_{inorg} from total carbon C_{tot} measured from two splits of the same sample. To determine C_{inorg}, samples are ashed at 475°C for 3 hours to oxidize organic matter. Ashed samples are processed on an Elementar Vario Macro Cube CN catalytic

combustor at 960°C and the resulting gases (carbon and nitrogen) are separated and measured with a thermal conductivity detector. Total C is determined using the same analytical procedure, excluding the ashing step (Wang, 2018). Shale standards USGS SBC–1 and SGR–1b, and sample replicates were measured alongside the main samples to verify accuracy and precision, respectively. Standard recovery was 96% on average, and replicate RSDs were less than 3%.

5.4.4. Sediment Mercury Concentrations (GAMES Laboratory)

Mercury concentrations were measured at the GAMES Laboratory on splits of 2018 and 2019 sample material. Approximately 50 mg of each subsample was placed in a Milestone DMA-80 evo and stage-heated to 750°C to volatilize Hg. Volatile Hg was collected by gold bead amalgamation, flushed from the beads, and then Hg concentrations were measured by atomic absorbance spectroscopy. The DMA-80 evo was calibrated using a liquid standard. National Research Council Canada certified reference materials TORT-3 (lobster hepatopancreas) and DORM-4 (fish protein) were analysed to ensure method accuracy. Mean percent recovery was 100.3 ± 1.5% (1s) for 21 measurements. Replicate RSDs were less than 2.2% for 25 replicate pairs.

5.4.5. Total Sulfur Content (Activation Labs)

Total sulfur was measured at ActLabs in July 2019 through combustion analysis (ActLabs, 2019). Sample powders (~0.2 g) were combusted in ceramic boats at up to 1550°C in a resistance furnace with a 99.5% pure oxygen atmosphere (Eltra, 2019). Volatilized sulfur species react with oxygen gas to form sulfur dioxide (SO_2). The SO_2 gas is filtered for particulates with a ceramic filter and traces of water are removed in a glass tube containing magnesium perchlorate (Eltra, 2019). Sulfur dioxide gas is measured in an Eltra CS-2000 infrared cell coupled to the furnace. The detection limit is 0.01%. Black shale standard USGS SGR-1b, a barium sulfate ($BaSO_4$) standard, and Geostats PTY Ltd sulphide gold ore GS900-5 and Pt-Pd-Au ore GS311-4 standards were used to ensure method accuracy. Mean percent recovery for all standards was 103.3 ± 3.0% (1s; n = 31). Seven replicate pairs were completed with replicate RSDs less than 3%.

6. Results

This section presents the results of geochemical analyses performed on the study core. Compressed results (sample means and standard deviations of element concentrations for stratigraphic intervals in the core) are shown in **Table 5**. The main observations of these data are described in the following subsections. Complete data tables for elements (and carbon isotopes) discussed in this section are found in **section 0**.

***Table 5*. Summary of geochemical results.** Mean ± 1s for XRD mineralogy, major elements, trace metals and organic carbon parameters for all samples, members and subunits.

Element / Unit			All Samples	Gordondale			PCS
				Total	Lower	Upper	
Upper Depth		m	1560.06	1575.00	1584.95	1575.00	1560.06
Lower Depth			1595.51	1595.51	1595.51	1584.58	1574.85
C_{org}	**C_{org}**	wt%	5.8 ± 2.2	6.3 ± 2.2	8.1 ± 2.2	5.2 ± 1.3	4.3 ± 0.8
	$\delta^{13}C_{org}$	‰	–29.5 ± 0.6	–29.7 ± 0.5	–29.7 ± 0.4	–29.6 ± 0.6	–29.1 ± 0.8
	Tmax	°C	476 ± 3	477 ± 3	476 ± 4	477 ± 4	475 ± 3
XRD	**Qtz**	wt%	41 ± 24	38 ± 27	33 ± 28	43 ± 26	45 ± 19
	Carb*		24 ± 26	40 ± 23	50 ± 27	30 ± 13	1.9 ± 3.0
	Clay**		26 ± 26	11 ± 19	6.5 ± 14	17 ± 23	45 ± 22
	Ap		4.8 ± 12	8.2 ± 15	8.6 ± 19	7.7 ± 12	0 ± 0
	Py		0.92 ± 1.5	0.35 ± 1.2	0.44 ± 1.4	0.26 ± 0.82	1.7 ± 1.6
Major Elements	**Al**		2.6 ± 1.1	3.8 ± 2.2	2.1 ± 1.0	4.9 ± 2.1	7.2 ± 1.6
	Ca		8.7 ± 7.5	11 ± 7	17 ± 6	7.6 ± 5.2	0.9 ± 0.5
	C_{inorg}		2.4 ± 2.0	3.0 ± 1.9	4.7 ± 1.6	2.0 ± 1.2	0.4 ± 0.2
	P		0.8 ± 1.7	1.0 ± 1.9	0.7 ± 0.8	1.2 ± 2.4	0.09 ± 0.14
	Fe		2.1 ± 1.4	1.8 ± 1.3	1.0 ± 0.5	2.3 ± 1.4	2.8 ± 1.5
	S_{TOT}		2.6 ± 1.1	2.4 ± 1.1	2.0 ± 0.6	2.7 ± 1.2	3.1 ± 1.2
Trace Metals	**Mo**	µg/g	80 ± 87	99 ± 91	175 ± 95	50 ± 42	18 ± 12
	V		711 ± 586	838 ± 614	1163 ± 624	623 ± 510	309 ± 164
	U		13 ± 8	15 ± 8	19 ± 9	12 ± 6	5.4 ± 2.9
	Cd		15 ± 16	16 ± 14	24 ± 15	11 ± 12	9 ± 21
	Re	ng/g	188 ± 123	209 ± 120	202 ± 90	214 ± 137	121 ± 108
	Hg		154 ± 78	143 ± 68	138 ± 57	147 ± 75	185 ± 98
	Mo	EF	172 ± 244	221 ± 260	474 ± 249	55 ± 45	14 ± 11
	V		18 ± 22	23 ± 24	45 ± 24	8.9 ± 5.3	3.3 ± 1.9
	U		13 ± 13	16 ± 14	27 ± 14	8.5 ± 6.3	2.2 ± 1.1
	Cd		431 ± 550	530 ± 579	1050 ± 587	187 ± 187	117 ± 268
	Re		472 ± 393	575 ± 392	873 ± 429	379 ± 195	145 ± 139

*Clays = illite + layered illite–smectite + kaolinite
**Carbonates = calcite + dolomite

6.1. Organic Carbon Geochemistry

6.1.1. Organic Carbon Content

Organic carbon content (C_{org}) varies within black shale samples in the *c-B6-A/94-B-8* core from a minimum of 2.6 wt% to a maximum of 11.5 wt% (**Figure 8**, column 1). The mean C_{org} content for all black shales, the PCS, and the Gordondale Member are 5.8 ± 2.1 wt% (*n* = 125), 4.4 ± 0.9 wt% (*n* = 39), and 6.5 ± 2.1 wt% (*n* = 86), respectively. The Gordondale Member Lower Unit exhibits the highest C_{org} values with a mean of 8.0 ± 2.1 wt% (*n* = 33) and contains four peak intervals where values from 9.6 wt% to 11.5 wt% are attained. The Upper Unit has a mean C_{org} content of 5.5 ± 1.5 wt% (*n* = 53); however, there are two peak intervals where C_{org} contents reach similar values (9.2 wt% and 10.7 wt%) as the Lower Unit peaks.

Often, trace metal concentrations are normalized to C_{org} due to their association with organic matter in the water column. However, in this core, metal concentration–C_{org} correlations are weak: Fe–, Mo–, V–, U–, Re–, Cd– and Hg–C_{org} have $r^2 < 0.24$. Trace metal EF–C_{org} correlations are also weak: Mo_{EF}–, V_{EF}–, U_{EF}–, Re_{EF}–, Cd_{EF}–C_{org} have $r^2 < 0.42$.

6.1.2. Stable Organic Carbon Isotopes

The mean organic carbon isotope composition ($\delta^{13}C_{org}$) for all black shale samples in the core is –29.5 ± 0.6 ‰ (*n* = 96) (**Figure 8**, column 2). Gordondale Member samples average –29.7 ± 0.5 ‰ (*n* = 73), while the Poker Chip Shale averages –29.1 ± 0.8 ‰ (*n* = 23). The Gordondale and PCS $\delta^{13}C_{org}$ means are significantly different based on *p*-values < 0.05 from an unpaired t-test assuming both sample sets are approximately normally distributed (*p*-value = 0.006). The more-negative Gordondale mean is attributed to a ~7 m interval at the top of the member (1582.10 m to 1574.85 m, inclusive; interval marked by red lines in **Figure 8**) where a sharp excursion to $\delta^{13}C_{org}$ values to a minimum of –30.5 ‰ is encountered (mean across the interval is –29.8 ± 0.3 ‰; *n* = 38). The negative excursion in the $\delta^{13}C_{org}$ signature (or "negative carbon isotope excursion"; N-CIE) lies centred within an overall positive arc in the $\delta^{13}C_{org}$ profile (or "positive carbon isotope excursion"; P-CIE; ~20 m; 1587.10 m to 1567.66 m). Samples before the P-CIE (1595.51 to 1587.64 m) have average $\delta^{13}C_{org}$ values of –29.9 ± 0.5 ‰ (*n* = 19), followed by the onset of the broad P-CIE that, excluding the samples within the N-CIE interval, averages –28.8 ± 0.4 ‰ (*n* = 30). The samples after the P-CIE (1566.37 to

1560.06 m) return to the more negative values similar to the pre-P-CIE values with a mean of –30.0 ± 0.3 ‰ (n = 9).

6.1.3. Programmed Pyrolysis Tmax, HI and OI

The Tmax (maximum temperature at the S2 peak in the programmed pyrolysis process) values for organic matter in black shale samples in the core average 476 ± 3 °C (n = 35), and do not vary statistically (p-value = 0.19) between the PCS (475 ± 3 °C; n = 15) and the Gordondale Member (477 ± 3 °C; n = 20) (**Figure 8**, column 3). Tmax values less than 435°C are thermally immature, those between 435 and 470°C are thermally mature, and greater than 470°C are thermally overmature (Peters, et al., 2005). The Gordondale Member and PCS Tmax values indicate that the core is thermally overmature. The hydrogen and oxygen indices (HI and OI, respectively) are plotted on a pseudo-van Krevelen diagram (**Figure 9**) and corroborate thermal overmaturity by their low values. **Figure 9** also indicates that kerogen could be of Type I or II, as is observed by others (e.g. Riediger & Bloch, 1995; Riediger, 1991). However, due to overmaturity, kerogen type should not be interpreted from the pseudo-van Krevelen plot for these core samples.

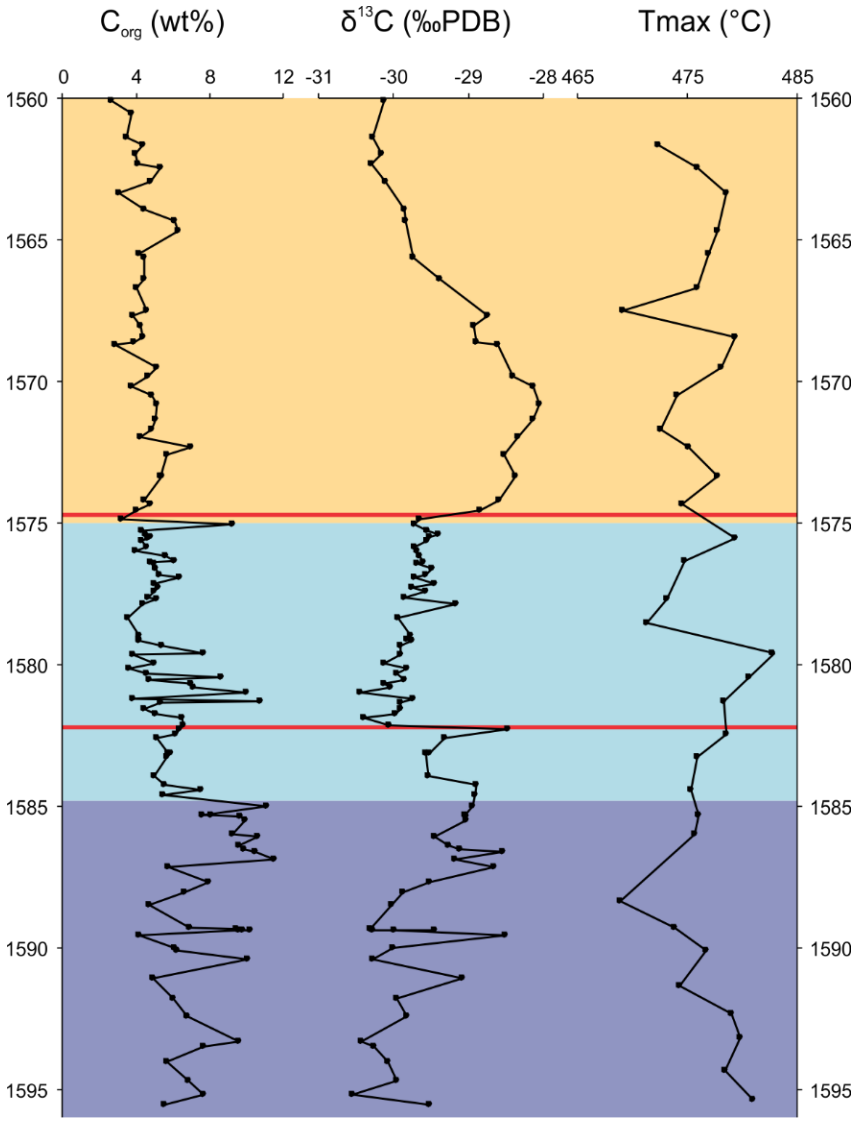

Figure 8. **Organic carbon geochemistry and thermal maturity indicator in the study core.** Total organic carbon (C_{org}) content, organic stable carbon isotope ($\delta^{13}C_{org}$) composition and Tmax profiles for the studied core. See **Figure 10** for stratigraphy.

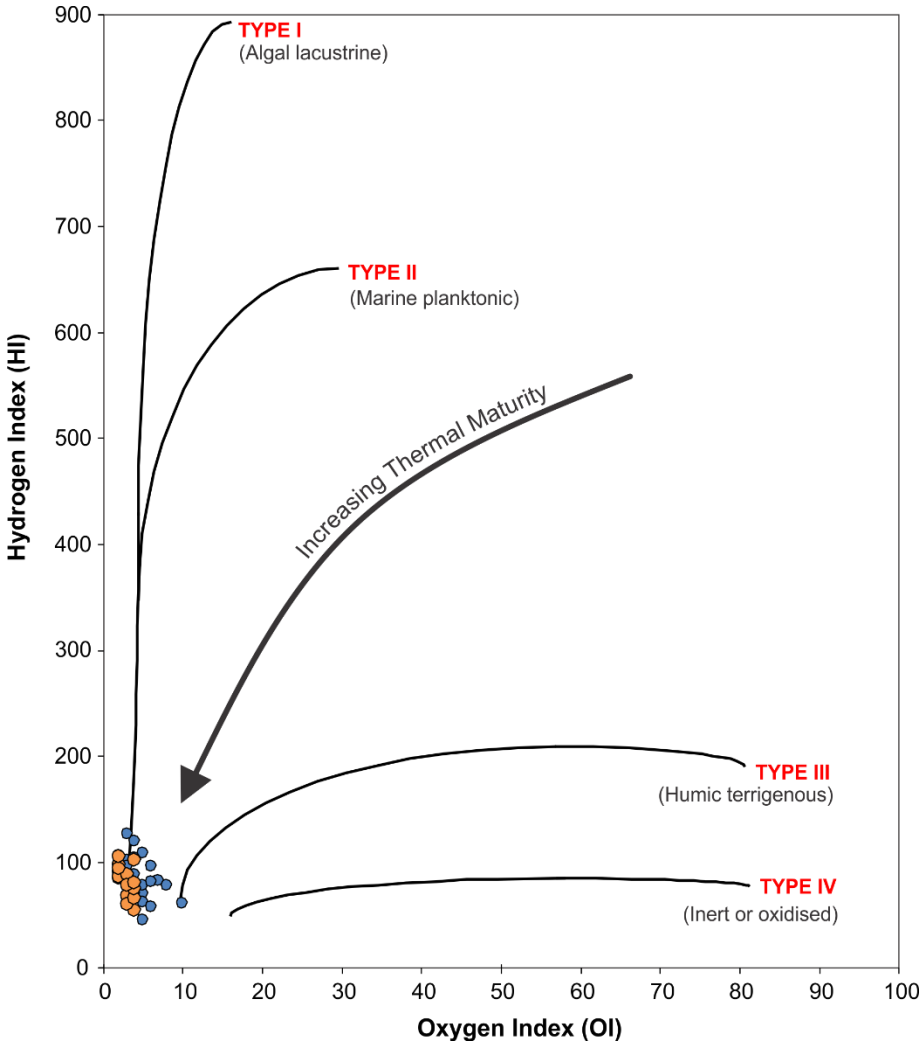

Figure 9. **Pseudo-van Krevelen diagram for kerogen type and thermal maturity.** Plot of hydrogen index (HI) versus oxygen index (OI) from Rock-Eval pyrolysis on the PCS (orange markers) and Gordondale Member (blue markers) black shales. Trends depicted for types I to IV kerogens and their typical organic matter types after Peters et al. (2005).

6.2. X-ray Diffraction Mineralogy

Quartz (Qtz) (**Figure 10**, column 1) is a major mineralogical component throughout the core at a mean of 41 ± 24 wt%. The Gordondale Member and PCS exhibit statistically similar Qtz content (p-value = 0.32), at means of 38 ± 27 wt% and 45 ± 19 wt%, respectively. The Gordondale Member Upper Unit is similar to the PCS (p-value = 0.81) with a mean Qtz content of 43 ± 26 wt%. The Lower Unit is not significantly different from the Upper Unit (p-value = 0.38) at a mean of 33 ± 28 wt%.

The *Carbonate (Carb)* fraction (**Figure 10**, column 2) is the sum of calcite (Cal) and dolomite (Dol) components. Carbonates are more abundant in the Gordondale Member at a mean of 40 ± 23 wt%, relative to the PCS at a mean of 1.9 ± 3.0 wt%. All PCS carbonates are dolomite (Dol = 1.9 ± 3.0 wt%; Cal = 0 ± 0 wt%), while calcite is the dominant carbonate phase in the Gordondale Member (Dol = 3.7 ± 5.9 wt%; Cal = 37 ± 26 wt%). The Gordondale Member Upper and Lower Unit carbonate contents are significantly different (p-value = 0.05), where the Lower Unit contains much more carbonate (50 ± 27 wt%) than the Upper Unit (30 ± 13 wt%). Carbonate content is weakly inversely correlated with Qtz content (r = –0.45) and clay content (r = –0.60).

The *Clay* fraction (**Figure 10**, column 3) is the sum of illite, layered illite–smectite, and kaolinite. The mean clay content in the core is 26 ± 26 wt%, indicating its variability. Illite is the most common clay mineral, found in 56% of the XRD samples. Layered illite–smectite and kaolinite are rarer in the core, found in 8% and 25% of the samples, respectively. Illite and layered illite–smectite occurrences are exclusive of one another, while kaolinite occurs with either illite or illite–smectite. Kaolinite only occurs in the PCS and is the most minor clay by its concentration, where samples containing the mineral have 1.7 ± 1.2 wt% (n = 9). While illite–smectite is found in only 3 samples, these contain 42 ± 10 wt%. In the 20 samples containing illite, the mean is 39 ± 24 wt%. Clay content is greater in the PCS than the Gordondale Member, with significantly different (p-value = 0.00003) means of 45 ± 22 wt% and 11 ± 19 wt%, respectively. The Gordondale Member Upper Unit has a higher mean clay content than the Lower Unit (17 ± 23 wt% and 6.5 ± 14 wt%, respectively), however these are not statistically different (p-value = 0.24).

Apatite (Ap) and *Pyrite (Py)* (**Figure 10**, columns 4 and 5) are minor mineralogical components in the core—compared to the Qtz, carbonate and clay contents—either because they do not occur frequently (Ap) or do not reach values > 5 wt% (Py). Only 7 of 45 of the XRD core samples contain measurable quantities of Ap, all of which are in the Gordondale Member. When Ap is present in the Gordondale Member, the mean sample content is 25 ± 19 wt%. While the PCS does not contain measurable quantities of Ap, it has the most samples with measurable Py content (15 of 22 samples) compared to the Gordondale Member (2 of 23 samples). Samples in the PCS which contain measurable Py have a mean concentration of 3.6 ± 2.2 wt%. The two samples in the Gordondale Member with measurable Py are not statistically different (p-value = 0.27) from the PCS; their mean is 3.7 ± 1.6 wt%.

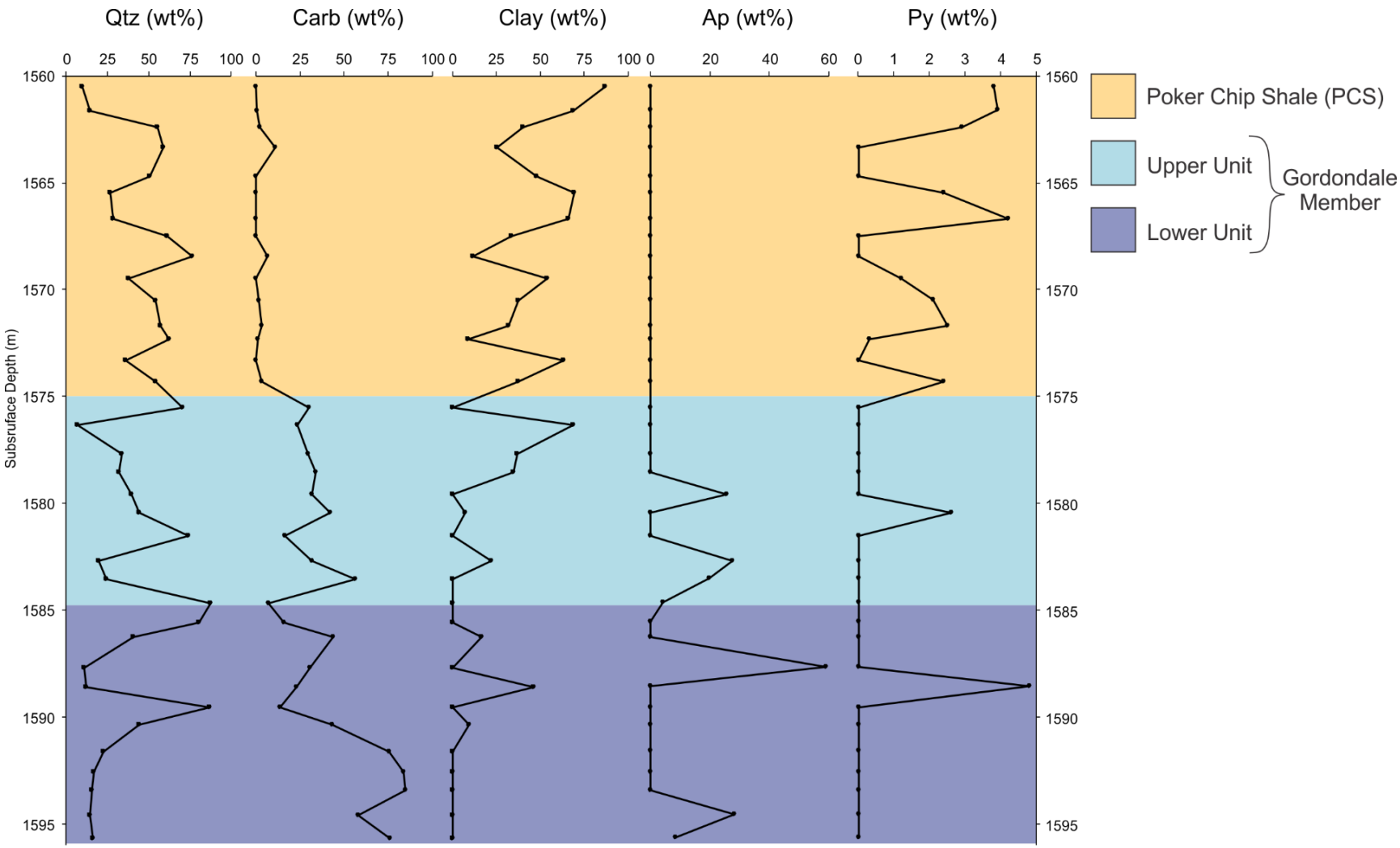

***Figure 10*. X-ray diffraction (XRD) mineralogy for the study core.** From left to right (column 1 to 5), the minerals are quartz (Qtz), carbonates (Carb; calcite + dolomite), clays (illite + layered illite–smectite + kaolinite), apatite (Ap) and pyrite (Py). Colours denoting geological members and subunits are labeled on the right.

6.3. Elemental Geochemistry

6.3.1. Major Element Concentrations

Mean *Aluminium (Al)* (**Figure 11**, column 1) for the black shale samples is 4.6 ± 2.6 weight percent (wt%). There is a steady increase in Al concentrations up-core, which can be observed through comparison of the Gordondale Member and PCS. Mean Al concentrations in the Gordondale Member and PCS are 3.8 ± 2.2 wt% (n = 73) and 7.2 ± 1.6 wt% (n = 23), respectively. The up-core increase corresponds most closely to the increasing XRD clay content (**Figure 10**, column 1), however a direct comparison cannot be made because these analyses were not completed on the same sample set (XRD samples not available for further geochemical analyses). Aluminium content exhibits very minor, statistically significant (p-value < 0.0006) inverse correlations with Mo and U concentrations (r^2 = 0.14 and 0.12, respectively), a minor statistically significant (p-value = 0.00009) positive correlation with Hg (r^2 = 0.16) and no correlation with the other trace metals discussed in the following **section 6.3.2**.

Calcium (Ca) and C_{inorg} contents (**Figure 11**, columns 2 and 3) are strongly correlated in the core (r^2 = 0.87), and both exhibit a sharp decrease at the Gordondale–PCS boundary. The mean Ca concentrations in the Gordondale and PCS are 11.1 ± 7.0 wt% (n = 73) and 0.9 ± 0.5 wt% (n = 23), respectively; mean C_{inorg} contents are 3.0 ± 1.9 wt% (n = 73) and 0.4 ± 0.2 wt% (n = 23), respectively. The Ca and C_{inorg} profiles most strongly correspond to the XRD carbonate profile (**Figure 10**, column 2). Calcium and C_{inorg} both exhibit moderate inverse correlations with Al (r = –0.70 and –0.67, respectively, n = 96), and poor positive correlation with organic carbon (r^2 = 0.34 and 0.28, respectively; n = 96).

Phosphorus (P) (**Figure 11**, column 4) is one of the most variable elements in the core; concentrations range from 0.02 to 14.9 wt%, with a mean of 0.8 ± 1.7 wt% (n = 96). All Gordondale Member samples give a mean P concentration of 1.0 ± 1.9 wt% (n = 73), but six of the included samples (at 1594.66, 1589.96, 1582.55, 1582.23, 1581.33 and 1580.94 m) with concentrations above the mean + 1s range between 3.0 and 15 wt%. The PCS mean P concentration is two orders of magnitude lower than the Gordondale Member at 0.09 ± 0.14 wt% (n = 23). A single PCS sample (at 1574.85 m, just above the PCS–Gordondale Member

contact) has an outlying concentration (greater than the mean + 1s) of 0.71 wt% meaning it is likely more similar to the Gordondale Member.

Iron (Fe) (**Figure 11**, column 5) increases slightly up-core with Gordondale and PCS means of 1.8 ± 1.3 wt% (n = 73) and 2.8 ± 1.5 wt% (n = 23), respectively; the mean for all samples is 2.1 ± 1.4 wt% (n = 96). Correlations between Fe and Al are slightly convoluted by 4 samples with high Fe contents (> 4.5 wt%). With these outliers removed, there is a good correlation between Fe and Al contents (r^2 = 0.76; n = 92). Iron shows a strong correlation with total sulfur content (S_{TOT}; **Figure 11**, column 6) (r^2 = 0.84; n = 83). Like Fe and Al, S_{TOT} exhibits an up-core increase; Gordondale Member and PCS means are 2.4 ± 1.1 wt% (n = 61) and 3.1 ± 1.2 wt% (n = 22), respectively. Both Fe and S_{TOT} show good positive correlations with Hg (r^2 = 0.56 and 0.71, respectively; $n_{Fe–Hg}$ = 92, $n_{S–Hg}$ = 82), but do not correlate with any other trace metal concentrations discussed in **section 6.3.2** (r^2 < 0.02).

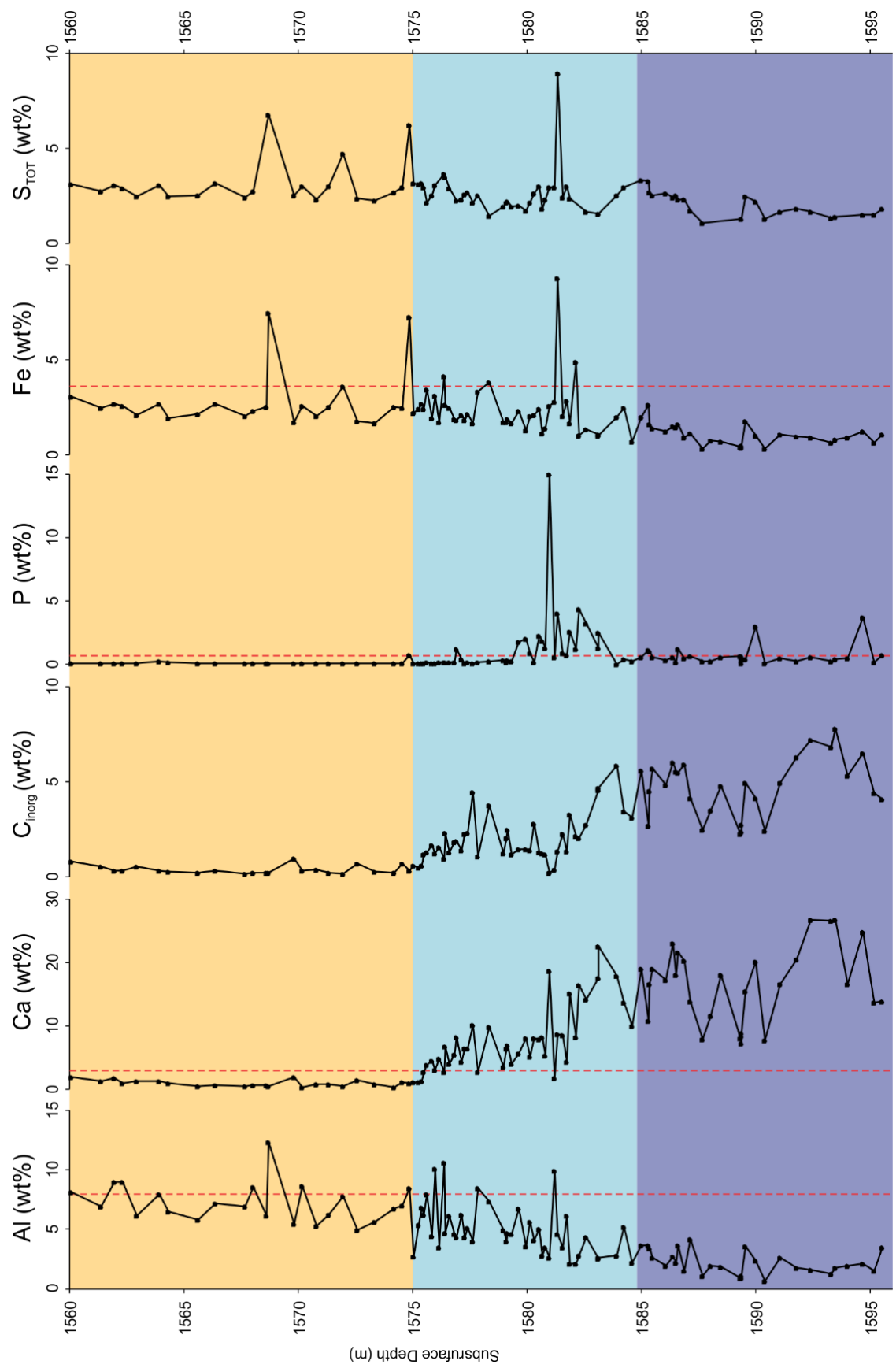

Figure 11. **Major elemental concentration profiles.** Solid black curves denote elemental concentrations, and red dashed lines denote upper continental crust content for the element when available (McLennan, 2001). See **Figure 10** for stratigraphy.

6.3.2. Trace Metal Concentrations

Molybdenum (Mo) (**Figure 12**, column 1) is highly enriched in the Gordondale Member Lower Unit with a mean concentration of 175 ± 95 µg/g and enrichment factor (Mo_{EF}) of 474 ± 249 (n = 29). The concentration and Mo_{EF} decrease up-core, as shown by comparing the elevated Lower Unit content with the Upper Unit and PCS means of 50 ± 42 µg/g (Mo_{EF} = 55 ± 45; n = 44) and 18 ± 12 µg/g (Mo_{EF} = 14 ± 11; n = 23), respectively. However, the Gordondale Member Upper Unit exhibits an initially low value of 22 ± 13 µg/g (Mo_{EF} = 31 ± 19; n = 25) from 1584.58 to 1578.93 m, and increases to 87 ± 37 µg/g (Mo_{EF} = 87 ± 49; n = 19) from 1578.34 to 1575.00 m.

The Mo trends are mirrored by *vanadium (V)* (**Figure 12**, column 2); Mo and V concentrations and EFs are well correlated (r^2 = 0.71) and strongly correlated (r^2 = 0.87), respectively (n = 96). Vanadium concentrations and V_{EF} in the Gordondale Member Lower and Upper Units, and PCS are 1163 ± 624 µg/g (V_{EF} = 45 ± 24; n = 29), 623 ± 510 µg/g (V_{EF} = 8.9 ± 5.3; n = 44) and 309 ± 164 µg/g (V_{EF} = 3.3 ± 1.9; n = 23), respectively. For V, the Upper Unit is subdivided as it is for Mo from 1584.58 to 1578.93 m and 1578.34 to 1575.00 m, which have V concentrations (and V_{EF}) of 262 ± 160 µg/g (V_{EF} = 4.8 ± 2.1; n = 25) and 1099 ± 409 µg/g (V_{EF} = 14 ± 3; n = 19), respectively.

There is an observable decrease in the *uranium (U)* (**Figure 12**, column 3) concentrations up-core from the Gordondale Member to the PCS, from 15 ± 8 µg/g (U_{EF} = 16 ± 14; n = 73) and 5.4 ± 2.9 µg/g (U_{EF} = 2.2 ± 1.1; n = 23), respectively. Like the Mo and V content, the U concentrations are greater in the Gordondale Member Lower Unit (19 ± 9 µg/g; U_{EF} = 27 ± 14; n = 29) than in the Upper Unit (12 ± 6 µg/g; U_{EF} = 8.5 ± 6.3; n = 44). However, unlike the Mo and V contents, the Upper Unit does not show a statistically significant difference between the 1584.58–1578.93 m (12 ± 7 µg/g; U_{EF} = 10 ± 8; n = 25) and 1578.34–1575.00 m (13 ± 6 µg/g; U_{EF} = 7 ± 3; n = 19) intervals.

Rhenium (Re) (**Figure 12**, column 4) is highly enriched in the core with concentrations of 188 ± 123 ng/g (Re_{EF} = 472 ± 393) in the black shales. The Re concentrations decrease up-core, most notably from the Gordondale Member (209 ± 120 ng/g; Re_{EF} = 575 ± 392; n = 73) to the PCS (121 ± 108 ng/g; Re_{EF} = 145 ± 139; n = 23). A decrease in the mean Re concentration from Gordondale Member Lower Unit (202 ± 90 ng/g; Re_{EF} = 873 ± 429; n = 29)

to Upper Unit (214 ± 137 ng/g; Re_{EF} = 379 ± 195; n = 44) is also observed, however concentrations are statistically alike (p-value = 0.63) while Re_{EF} values are significantly different (p-value = 1.3×10^{-6}).

Cadmium (Cd) (**Figure 12**, column 5) content varies strongly through the core, with concentrations averaging 15 ± 16 µg/g and Cd_{EF} of 431 ± 550 (n = 96). The Cd stratigraphic trend mirrors those of Mo and V, and Cd_{EF} correlates well with both Mo_{EF} (r^2 = 0.73; n = 96) and V_{EF} (r^2 = 0.74; n = 96). As with Mo and V, Cd contents decrease up-core; the highest Cd concentrations are observed in the Gordondale Member at 16 ± 14 µg/g (Cd_{EF} = 530 ± 579; n = 73) and the lowest and most variable Cd concentrations are found in the PCS at 9 ± 21 µg/g (Cd_{EF} = 117 ± 268; n = 23). The Lower Unit of the Gordondale Member has a mean Cd concentration of 24 ± 15 µg/g (Cd_{EF} = 1050 ± 587; n = 29) and the Upper Unit shows the switch from low (3.6 ± 3.5 µg/g; Cd_{EF} = 78 ± 74; n = 25) to high (21 ± 11 µg/g; Cd_{EF} = 330 ± 195; n = 19) Cd content in the same intervals as for Mo and V.

Mercury (Hg) (**Figure 12**, column 6) concentrations in the black shale samples yield an average of 154 ± 78 ng/g (n = 92) and is generally lower (but only by a minor statistical difference; p-value = 0.07) in the Gordondale Member (143 ± 68 ng/g; n = 69) than the PCS (185 ± 98 ng/g; n = 23). Mercury content is not statistically different (p-value = 0.57) between the Lower and Upper Units of the Gordondale Member (138 ± 57 ng/g and 147 ± 75 ng/g, respectively). Peaks in the Hg concentration (up to 566 ng/g) above the mean occur in several samples; the four most apparent peaks occur at 1581.33, 1574.85–1574.53, 1571.92 and 1568.68 m.

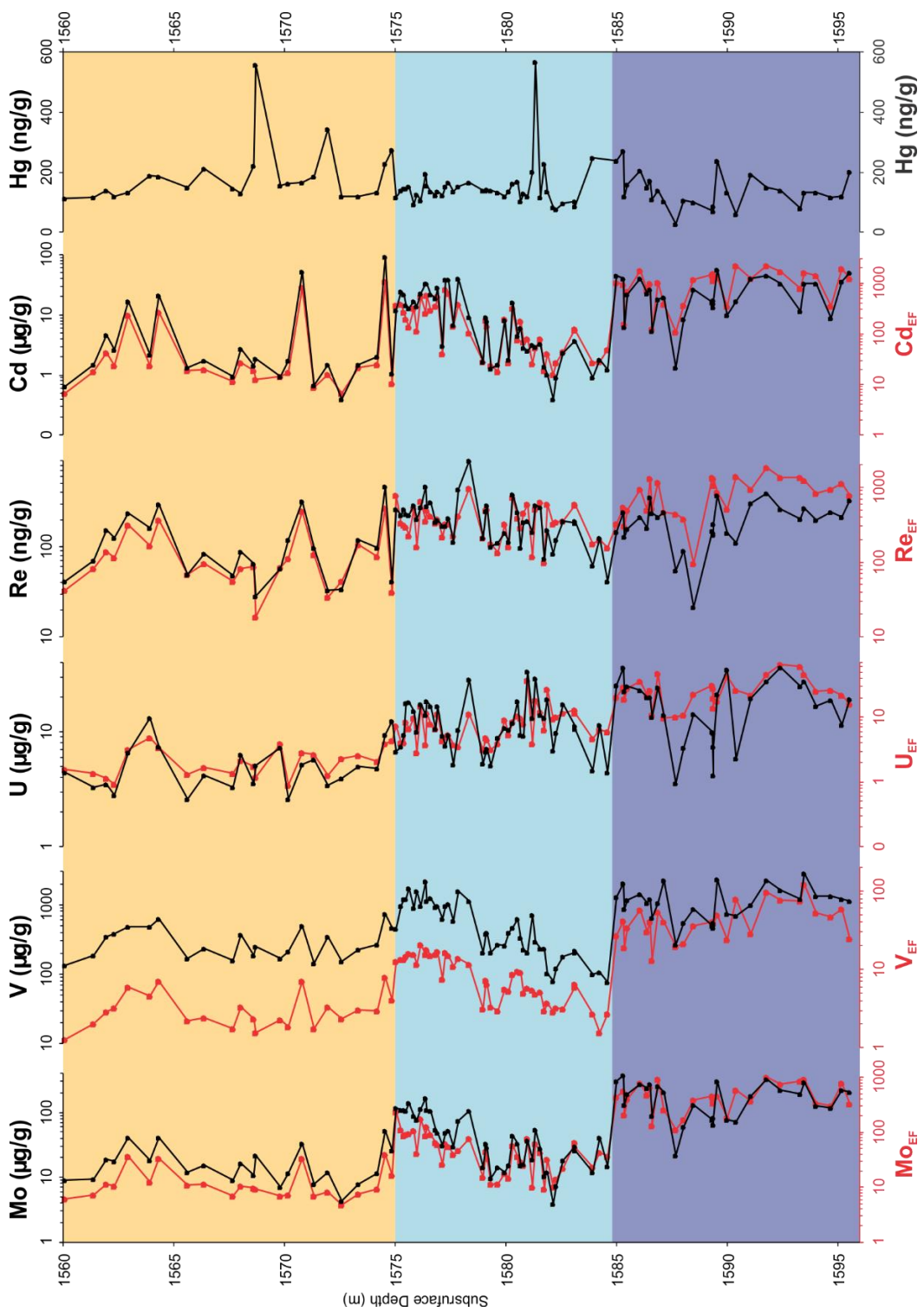

Figure 12. **Trace metal elemental concentration and enrichment factor (EF) profiles.** Black curves denote the trace metal concentrations, and red curves denote EFs corrected to upper continental crust content for the trace metal and Al (McLennan, 2001). See **Figure 10** for stratigraphy.

7. Discussion

7.1. Consideration of Thermal Maturity

Tmax values for the Gordondale Member and PCS in the *c-B6-A/94-B-8* core lie within a narrow range around 476°C (**Figure 8**, column 3) indicating that the organic-rich units through the entire section are overmature with respect to hydrocarbon generation (Tmax > 470°C; Peters, et al., 2005). Yang (2019) demonstrated that trace metals remain largely immobile and are not lost from the sediment phase during maturation. The Re-Os geochronometer has produced precise and accurate depositional ages for overmature black shale intervals, which is only possible with limited post-depositional redistribution of the metals (Selby & Creaser, 2005; Creaser, et al., 2002). Dickson et al. (2019) also note trace metal immobility during maturation based on limited partitioning of the metals into fluid phases, but do suggest that significant amounts of the C_{org} phase may be lost, thereby artificially inflating trace metal concentrations. Expulsion of oil and gas compounds from the Gordondale Member and/or PCS to other stratigraphic units or geographical location is unlikely based on limited correlation between biomarker signatures in these source rocks and migrated hydrocarbons through the WCSB (Riediger, 1994). However, potential localized degradation or small-scale migration of hydrocarbons has resulted in decoupling of C_{org} from the elemental content of the surrounding sediments as observed by non-relation of C_{org} with all trace metals (very low linear regression r^2 values).

Carbon isotope systematics may be affected by compound partitioning during maturation, as demonstrated by the range of $\delta^{13}C_{org}$ compositions of thermogenic methane (–60 to –40 ‰) versus oils and heavier gases (–45 to –20 ‰) (Fuex, 1977). However, the $\delta^{13}C_{org}$ values of these overmature samples represent the bulk organic matter $\delta^{13}C_{org}$ composition because (1) the compounds inherit the C-isotope systematics of the same predecessor material, (2) reconfiguration of C_{org} is localized rather than whole-system loss, and (3) bulk rather than compound-specific C_{org} isotope compositions are measured.

7.2. Identification of the T-OAE

The T-OAE is identified in the *c-b6-A/94-B-8* core by the telltale N-CIE embedded within an overall P-CIE in the $\delta^{13}C_{org}$ profile (**Figure 13**). Due to the non-linear baseline, a

second-order polynomial function (r^2 = 0.57) is fitted to the broad P-CIE with N-CIE samples removed and is used as the baseline to determine the extent of the N-CIE. The highest predicted $\delta^{13}C_{org}$ during the P-CIE is –28.6‰ at 1576.80 m. The difference between the lowest measured $\delta^{13}C_{org}$ value in the N-CIE interval (–30.5‰) and the highest predicted value provides a maximum excursion of –1.9‰ from the polynomial P-CIE baseline. Measured differences at the onset and conclusion of the N-CIE are –1.6‰ and –0.8‰, respectively. The onset of the P-CIE defines the Pl–To boundary and the onset of the mass extinction that accompanied the T-OAE, and the N-CIE marks the classically-defined OAE (Them II, et al., 2018). Here, the T-OAE is defined between the onset and conclusion of the P-CIE, with its apex occurring through the N-CIE. The T-OAE was defined in comparison to other WCSB (Alberta) sections from Them II et al. (2019).

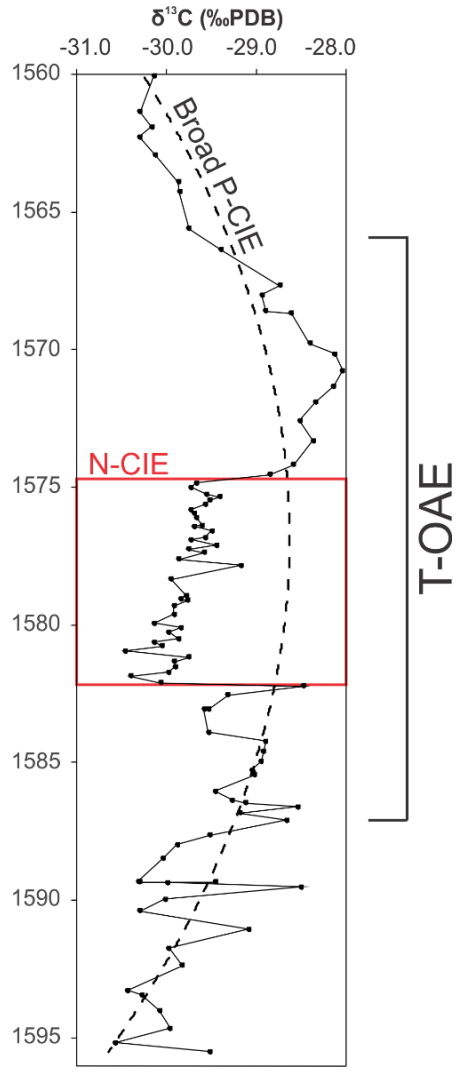

Figure 13. **Study core organic carbon isotope profile.** Stable bulk organic carbon isotope signature ($\delta^{13}C_{org}$) reported in permil relative to PeeDee Belemnite (‰PDB). The profile follows a broadly positive carbon isotope excursion (P-CIE; black dashed line) punctuated with an abrupt negative carbon isotope excursion (N-CIE) near the centre of the trend. The Toarcian Oceanic Anoxic Event (T-OAE) is identified by the N-CIE, however the event begins at the P-CIE onset and concludes at the end of the P-CIE.

7.3. Local Paleoenvironment

7.3.1. Sea Level Changes

The entire Jurassic system encompasses a first-order eustatic sea level rise, with multiple embedded second- and third-order global transgressive–regressive (T-R) cycles (Ruban, 2015). The Early Jurassic contains the first of two Jurassic second-order T-R cycles (Ruban, 2015). Gordondale Member deposition occurred during a sea level transgression of several 10s of meters, with highstand at the top of the *Falciferum Zone* (early Toarcian)

(Asgar-Deen, 2003). The transgression is followed by second-order regression in which the PCS is deposited. The highstand is noted in the study core atop the N-CIE where trace metal content peaks followed by a sharp decline and mineralogy/major geochemistry switches from carbonate/Ca-rich/Al-poor to silicate/Ca-poor/Al-rich deposition. High trace metal contents in sediments at sea level highstands are a result of deeper water deposition combined with enhanced primary productivity (e.g. driven by upwelling of nutrient-rich waters), and organic matter remineralization, which creates conditions for lower-oxygen sea floors where redox-sensitive metals are reduced and removed to sediments efficiently (LaGrange, et al., 2019).

Temporal variability in carbonate–silicate sedimentation as observed in the study core may be controlled by sea level and/or sediment supply changes (Boggs, 2006). A sea level transgression may cause sediment deposition lower than the carbonate compensation depth (CCD), below which the rate of carbonate mineral dissolution outpaces the rate of supply. The CCD fluctuates from ~3000 to 5000 m water depth and in the Jurassic was located at approximately 4000 m water depth (van Andel, 1975). However, the Gordondale Member was unlikely to have been deposited below CCD (Asgar-Deen, 2003) and the PCS was deposited in a more-oxygenated, regressive environment (Riediger, 2002) therefore both units are assumed to have been deposited above CCD. Because carbonate sediment production is mainly an organic process (versus abiotic precipitation), sea level transgression can also affect the shallow water organic source flux to deeper waters. Carbonate platforms are drowned if transgression occurs too rapidly and outpaces shallow-water biological carbonate generation. Platform drownings are accompanied by elevated phosphogenesis due to increased P availability (Follmi, 1996). Gordondale Member deposition coincided with the presence of a carbonate platform to the southwest (Nordegg Member) and an elevated P content at the onset of the N-CIE, so transgressive platform drowning is a candidate for causing the transition from carbonate to silicate deposition. A subsequent sea level regression would have led to deposition in a proximal setting where continental siliciclastic (detrital) input was elevated. An increasing Al concentration up-core is likely reflective of this environmental change, as Al is a major component of aluminosilicate continental material. It is likely that both carbonate platform drowning during transgression and increasing detrital flux during regression led to the abrupt shift from carbonate (Gordondale) to silicate (PCS) composition.

7.3.2. Cordilleran Tectonics

Initial study of Jurassic strata of the WCSB led to suggested tectonic margin activation and development of a foreland basin on the west coast of ancient North America by the Late Jurassic (Kimmeridgian–Oxfordian) when subsidence occurred (Price, 1994). More recently, the timing of initiation has been pushed into the Early Jurassic based on syn-genetic detrital zircon preservation from contemporaneous western igneous sources (Pana, et al., 2017).

The Gordondale Member in the study core is punctuated by highly competent, light grey 20-60 cm intervals of silty normally-graded bedding, occasionally topped with inversely-graded bedding. Moslow (2016) describes these as turbidite–debris flow couplets. Ross and Bustin (2006) describe 15-90 cm thick microcrystalline argillaceous marlstones interbedded in the Gordondale Member Lower Unit in a core (*d-88-H-94-A-13*) ~70 km NNE of the study core. Asgar-Deen et al. (2004) describe 10 cm thick erosion-resistant, quartzose calcilutites and calcarenites interbedded with the black shales of the Hettangian Black Bear Ridge outcrop strata (~65 km WSW of the study core) and within the Gordondale Member Lower Unit in the Gordondale Member type section (~160 km ESE of the study core). The normally-graded intervals ("turbidites") in the core may be tectonic-induced flows in a developing foreland basin. Together with the interbedded fine-grained black shales this interval could constitute the pre- to syn-orogenic *flysch* tectofacies (after the Alpine Flysch of Europe; Homewood & Lateltin, 1988). Flysch sequences are deep-marine units interspersed with terrestrial turbidites developed on active margins (Homewood, 1982) and are typically overlain by a shallower, syn- to post-orogenic *molasse* shale and sandstone tectofacies (after the European Alpine Molasse; Homewood and Lateltin, 1988). In the WCSB, the mid-Jurassic interval of the Fernie Formation has been described as a molasse deposit (Eyles and Miall, 2007), therefore underlying sediments of the Early Jurassic can be reasonably classified as flysch.

These turbidites are like the underlying Pardonet Formation dolostones based on the major element geochemical results from this core. The geochemical similarity means that flows could have originated on the eastward continental slope, rather than a westward allochthonous terrane along the subducting margin as invoked by western-sourced meteoric input to the basin (Riediger & Coniglio, 1992). However, slope destabilization triggering flows may still have be tectonic in nature—e.g. subduction-induced earthquakes. Additionally, ash bed frequency

increases from the Gordondale Member (n = 5) to the PCS (n = 13), indicating increased proximal active volcanism (subduction zone volcanic arc development?).

7.3.3. Bottom Water Redox Conditions

Redox-sensitive trace metal concentrations and authigenic enrichments (as EFs) in ancient marine sediments are representative of bottom water redox conditions at the time of sediment deposition (Tribovillard et al., 2006). Single-element proxies provide some insight into general conditions; e.g. sediments with Mo > 100 μg/g were likely deposited under euxinic waters (Scott and Lyons, 2012). However, there are limitations with single-element proxies because contrasting environments may produce like-enrichment signatures; e.g. Mo from 25 to 100 μg/g may have been deposited under euxinic conditions but clastic dilution decreased the relative concentration, or under suboxic conditions with an active particulate shuttle delivering excess Mo to bottom waters and shallow pore water H_2S reducing Mo into sediments (Scott and Lyons, 2012). Combining trace metals through a multi-proxy approach enhances environmental interpretations.

The core samples exhibit a range in concentrations for all redox-sensitive trace metals (Mo, V, U, Re) and their ratios (Re/Mo, Mo/U) signalling fluctuating bottom water redox and/or local environmental conditions over the depositional period (**Figure 14**). However, trace metal content remained enriched above upper continental crust content in most samples implying that well-oxygenated bottom-water conditions were generally not recorded. Macrofossils allude to oxic conditions at least periodically; bivalves and belemnites are the most abundant macro-organisms observed in the core. Bivalves are benthic organisms and due to their relative immobility would be unlikely to survive if oxygen levels decreased quickly, but thin (< 2 cm), discrete shell beds may indicate short periods of dysoxic to oxic bottom-waters assuming that these were deposited *in situ* (Henderson, 2004). Belemnites were squid-like pelagic organisms and are found sporadically through the core; unlike bivalves, due to belemnoid mobility both laterally and vertically through the water column, these organisms are less diagnostic of redox conditions in the water column directly overlying deposited sediments but do indicate that oxygen was present at some level within the column or geographical area. Evidence from the Cleveland Basin (northwestern Europe) suggests a shift from deeper-dwelling belemnites before the T-OAE to surface-dwelling belemnites during the T-OAE as

bottom-water anoxia took hold (Ullmann, et al., 2014). If the bottom-to-surface shift happened in the northeast Panthalassan basin, then the occurrence of belemnites within the studied core suggest that surface oxygen levels were high enough to support their existence during the T-OAE.

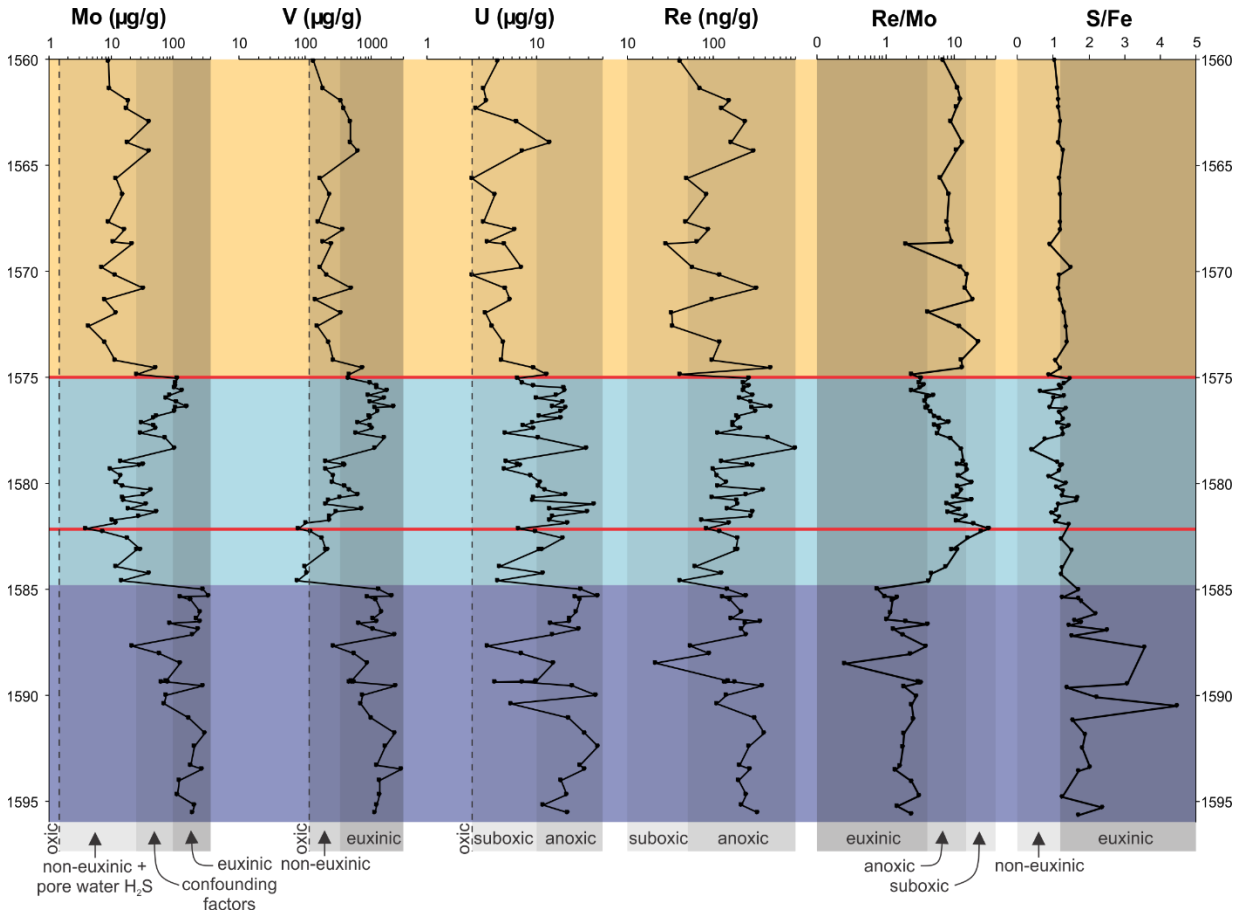

Figure 14. **Bottom water redox states based on trace metal concentrations and ratios for the study core.** Redox states are indicated by vertical grey bars (labelled at base). Upper continental crust average concentrations (black dashed lines; McLennan, 2001) are noted for Mo (1.5 µg/g), V (107 µg/g) and U (2.8 µg/g). The Re scale does not extend to the crustal concentration of 0.4 ng/g. Enrichment factors for Re and Mo are used for the Re/Mo ratio. Gordondale Member Lower Unit (dark blue), Upper Unit (light blue), Poker Chip Shale (orange) and negative carbon isotope excursion interval (between red lines) are noted.

Suboxic conditions are inferred mainly within the PCS, but also at the base of the Gordondale Member Upper Unit. Suboxia is diagnosed in these samples by high Re/Mo_{EF} ratios and plotting within the suboxic trend (approaches Re/Mo_{EF} ~15 ppb/ppm; Turgeon & Brumsack, 2006) on a Re_{EF}–Mo_{EF} covariation diagram (**Figure 15**). An increasing Re/Mo_{EF} trend towards suboxia begins at the Gordondale Member Lower–Upper Unit contact, reaching

a maximum at the onset of the N-CIE where values lapse back to general anoxia. The Re/Mo_{EF} in the PCS does not follow a strict temporal trend as values fluctuate in the lower half of the PCS but appear to equilibrate somewhat in the upper half. Poker Chip Shale Re and U concentrations also dip into the suboxic ranges (Re 0.4–42 ng/g, Crusius, et al., 1996; U = 2.8–10 μg/g, Partin, et al., 2013) and into the anoxic range; therefore, the PCS likely experienced suboxic to weakly anoxic bottom water conditions.

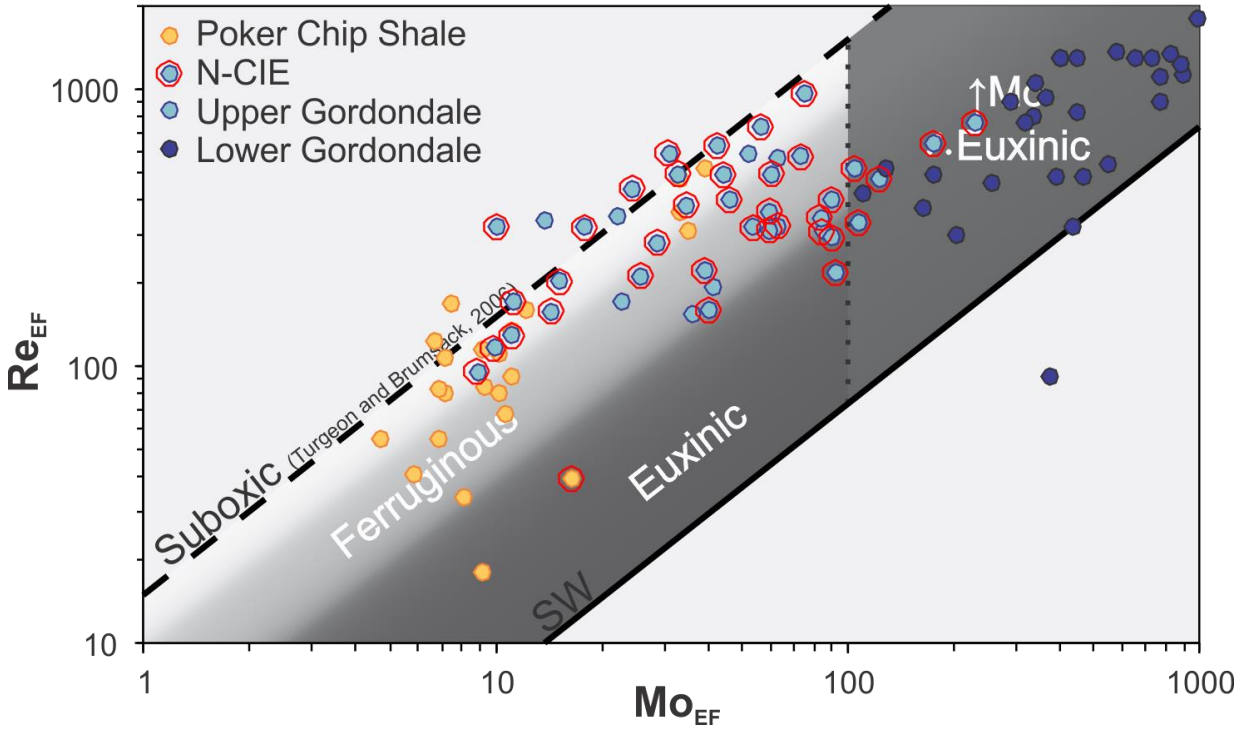

Figure 15. **Re_{EF}–Mo_{EF} covariation plot for study core samples.** Re and Mo covariation for samples of the Gordondale Member and Poker Chip Shale. Samples range from below sea water (SW) weight ratio (0.8 ppb/ppm) to beyond the suboxic weight ratio (15 ppb/ppm) interpreted by Turgeon and Brumsack (2006).

Generally anoxic (ferruginous + euxinic) conditions are interpreted to have prevailed through much of the Gordondale Member. General anoxia is inferred from U > 10 μg/g (Partin et al., 2013) and Re > 42 ng/g (Crusius et al., 1996). Uranium content decreases slightly from the Gordondale Member Lower Unit to the Upper Unit, but both units are inferred as dominantly anoxic.

Corrections for dilution of trace metal signals by detrital sedimentation can be made using enrichment factors (EFs), which are calculated by **Equation 2**. In **Figure 16**, trace metal EFs are depicted with redox trends. Because EFs are not typically given in the literature to

define redox state ranges and Al concentrations are not available for all studies, EF ranges for redox states are the concentration ranges from the literature (Mo: Scott & Lyons, 2012; V: Quinby-Hunt & Wilde, 1994; U: Partin, et al., 2013; Re: Crusius, et al., 1996) normalized to upper continental crust averages (McLennan, 2001). Enrichment factor profiles improve the ability to interpret the trace metal signals, especially for U and V in this core which must have been somewhat influenced by the increasing detrital input in the PCS.

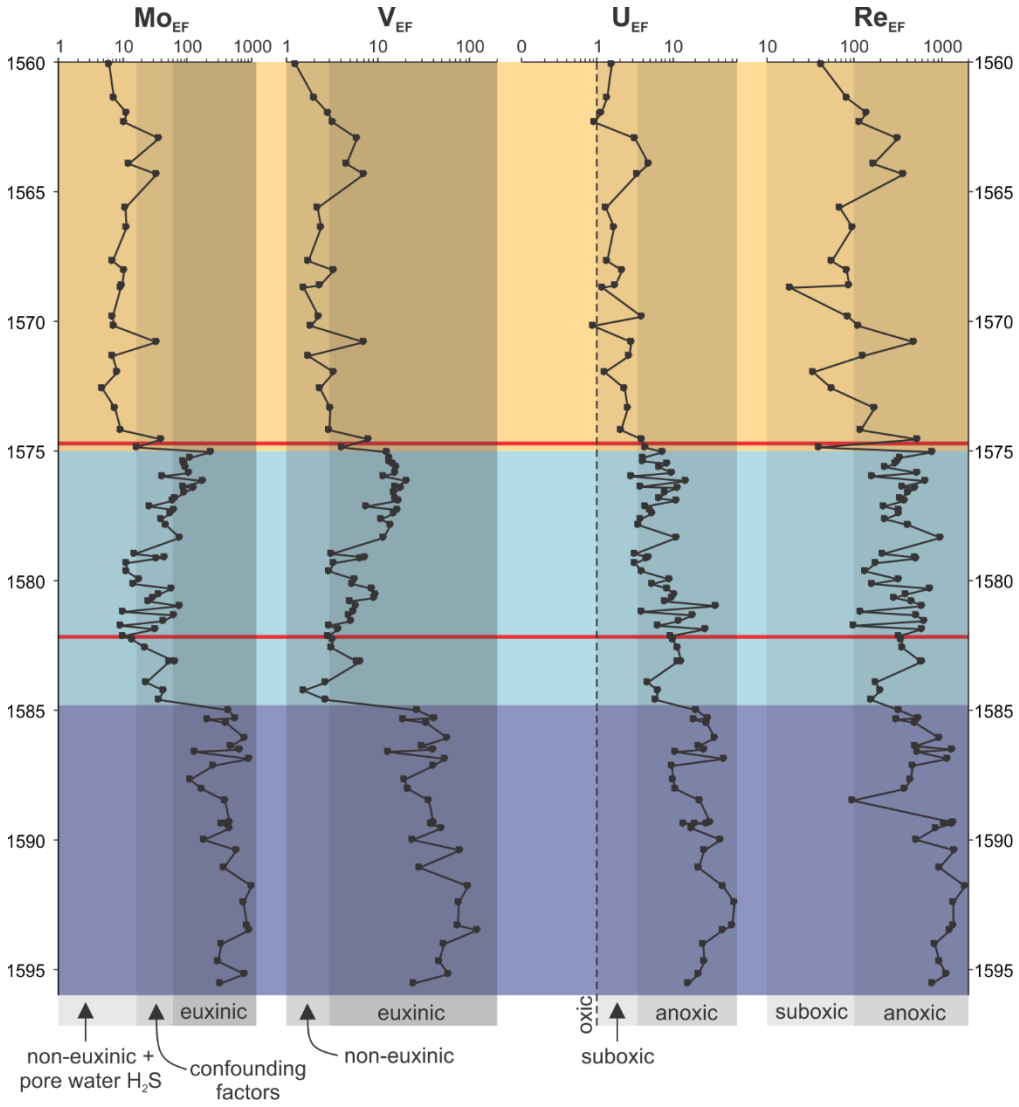

Figure 16. **Redox states based on trace metal enrichment factors for the study core.** Redox states are indicated by vertical grey bars (labelled at base) and are based on literature concentration ranges normalized to upper continental crust average concentrations (McLennan, 2001). Gordondale Member Lower Unit (dark blue), Upper Unit (light blue), Poker Chip Shale (orange) and negative carbon isotope excursion interval (between red lines) are noted.

Concentrations of Mo > 100 μg/g (Scott & Lyons, 2012; Mo_{EF} > 67) and V > 320 μg/g (Quinby-Hunt & Wilde, 1994; V_{EF} > 3), strongly correlated S_{TOT}/Fe ≥ 1.15 (pyrite ratio) and Re/Mo_{EF} < 4 (Turgeon & Brumsack, 2006) distinguish euxinic from non-euxinic samples in anoxic intervals. The Gordondale Member Lower Unit is greatly enriched in all trace metals; mean Mo and V concentrations are 175 ± 95 μg/g and 1163 ± 624 μg/g, respectively, Re/Mo_{EF} ratios are 2.1 ± 0.9 and S_{TOT}/Fe are strongly correlated (r^2 = 0.80) above the pyrite ratio at 2.0 ± 0.8 indicating that conditions were predominantly euxinic. The Upper Unit which contains the T-OAE as identified by a N-CIE, is less enriched in redox-sensitive trace metals than the Lower Unit but is still enriched above upper continental crust concentrations. The entire Upper Unit is generally anoxic, but there is a transition from low Mo and V content in the bottom portion of the unit (1584.58–1578.93 m), suggesting generally non-euxinic conditions, to high Mo and V content and low Re/Mo_{EF} ratios in the top portion (1578.34–1575.00 m), indicating a shift to strong euxinia within the N-CIE interval.

The S_{TOT}/Fe ratio remains at or above the stoichiometric pyrite weight ratio in most Upper Unit samples, so sulfidic conditions remained in pore waters even during non-euxinic periods (corroborated by Mo concentrations between 1.5–25 μg/g; Scott & Lyons, 2012) allowing for pyrite formation within reactive Fe-rich sediment even when bottom waters were non-euxinic. This is likely the case for the suboxic to weakly-anoxic (non-euxinic) PCS, as Mo concentrations remain between 1.5–25 μg/g and the unit is often characterised as "pyritic" (Riediger, 2002), which is corroborated by increased XRD pyrite content.

7.3.4. Basin Connection to the Global Ocean

Relationships between trace metal content and hydrographic regimes of modern environments have been observed by Sweere et al. (2016) for Cd–Mo, Algeo and Tribovillard (2009) for Mo_{EF}–U_{EF} and Algeo and Lyons (2006) for Mo–C_{org}. Using these relationships, trends on trace metal covariation plots have been used to infer paleohydrographic configurations for paleoredox reconstructions (e.g. McArthur, 2019; Algeo and Rowe, 2012; Tribovillard et al., 2012; Algeo and Tribovillard, 2009). These applications—except for Mo–C_{org}—are used here for the Early Jurassic samples to determine if the Gordondale Member/PCS basin was open to or restricted from water mass exchange with the global ocean during the T-OAE. The Mo–C_{org} covariation of Algeo and Lyons (2006) is not applied to the

study core samples, as the overmature conditions have likely caused a decoupling of the trace metals from the organic content. Basin hydrography is an important paleoenvironmental factor to define for these samples because the T-OAE was by definition a global event, therefore any interpretations made on the global marine paleoredox environment can only be inferred if the basin was physically linked to that environment. If the basin was strongly restricted from exchange with the global ocean, only local paleoenvironmental characteristics can be inferred.

The Mo–U covariation (**Figure 17a**) for the Gordondale Member and PCS core samples cover an open/unrestricted marine trend influenced by redox variation (Tribovillard, et al., 2012; Algeo & Tribovillard, 2009). The open marine trend occurs as an increasing Mo/U ratio from suboxic (Mo/U ≈ 1–3; below seawater weight ratio) to ferruginous (Mo/U ≈ 3–10; across the seawater weight ratio) and euxinic (Mo/U ≈ 10+; above the seawater weight ratio). A redox variation occurs up-core from strongly euxinic to euxinic in the Gordondale Member Lower Unit, from strongly ferruginous to euxinic in the Upper Unit, and from weakly ferruginous to strongly suboxic in the PCS. The N-CIE samples identifying the T-OAE all lie within the ferruginous to euxinic Gordondale Member Upper Unit.

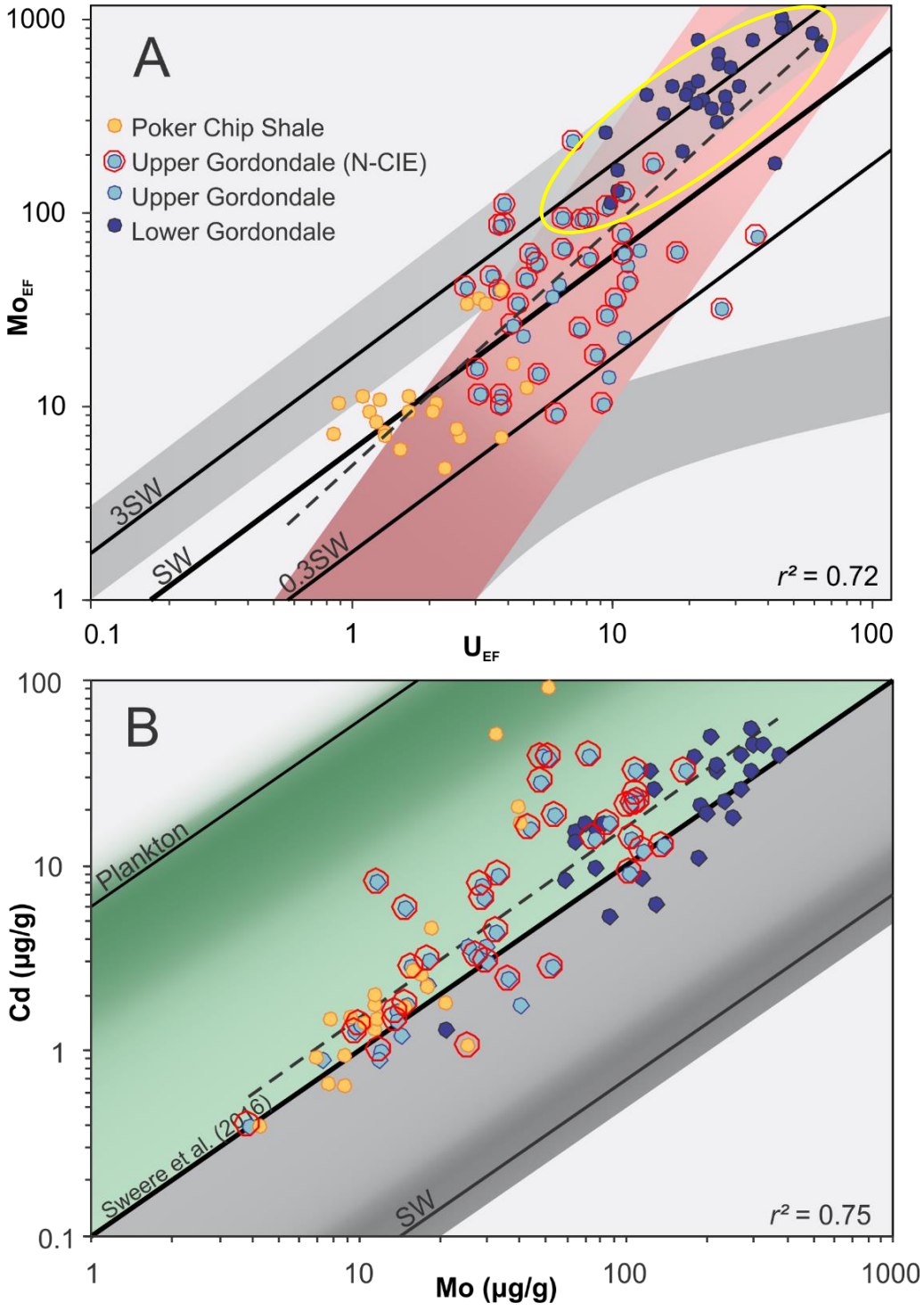

***Figure 17*. Trace metal covariations for basin hydrography.** (**A**) Mo_{EF}–U_{EF} covariation (after Algeo & Tribovillard, 2009) within the open marine (red bar) and particulate shuttle (upper grey bar) trends (overlap identified by yellow oval). No samples lie within the restriction trend (lower grey arc); (**B**) Cd–Mo covariation after Sweere et al. (2016) with most samples lying in the open marine upwelling zone trend (green). Lines indicate weight ratios of the trace metals in seawater (SW; Tribovillard, et al., 2006) and factors thereof, average modern plankton (Brumsack, 1986) and empirical sediment Cd/Mo ratio of 0.1 based on the threshold between modern upwelling and restricted environments (Sweere, et al., 2016).

The Cd–Mo covariation plot for Gordondale Member and PCS samples (**Figure 17b**) corroborates the generally unrestricted trend observed in the Mo_{EF}–U_{EF} covariation. A power regression through all samples yields good correlation (r^2 = 0.75) along $Cd = 0.14Mo^{1.03}$ which is approximated to a linear relationship where Cd/Mo = 0.14, indicating that most samples lie above the empirical Cd/Mo ratio of 0.1 as defined in Sweere et al. (2016) which distinguishes between a continental margin upwelling setting (Cd/Mo > 0.1) and a hydrographically restricted basin (Cd/Mo < 0.1). Phosphorus content in the Gordondale Member is substantially elevated (P up to 15 wt%), which also indicates the probability that upwelling was a significant process occurring at the time of the unit's deposition (Follmi, 1996).

Taken together, the Mo_{EF}–U_{EF} and Cd–Mo covariations imply that the Gordondale Member and PCS were deposited in an open marine environment along a continental margin upwelling zone with a generally temporal (stratigraphic) bottom water redox variation from strongly euxinic in the lower Gordondale Member to suboxic in the PCS; bottom water redox interpretations agree with those based on other proxies (Mo, V, U, Re concentrations/EFs and Re/Mo_{EF}, S_{TOT}/Fe ratios).

7.3.5. Consideration of a Particulate Shuttle

A confounding factor in the interpretation of the Gordondale Member Lower Unit and euxinic Upper Unit samples on the Mo_{EF}–U_{EF} covariation (**Figure 17a**) arises due to an overlap in the open/unrestricted marine trend and the particulate shuttle trend along the 3-times seawater weight ratio. High Mo and V concentrations also allude to the possibility of a particulate shuttle as both are particle-reactive. If a particulate shuttle operated during the deposition of the Gordondale Member and/or PCS, paleoredox conditions may be exaggerated by the enrichment of Mo and V, and high Mo/U ratios.

The particulate trend on an Mo_{EF}–U_{EF} covariation occurs due to the strong affinity for Mo (and V), but not U, to adsorb to Mn-(oxy)hydroxide particles in an oxic water column (Ostrander et al., 2019). Upon sinking across the redox chemocline and delivery to the sediment–water interface the Mn particulates undergo reductive dissolution, releasing adsorbed Mo thereby increasing its bottom water and/or pore water concentration with respect to the average seawater concentration. Due to the increased availability of Mo in bottom waters, reduction to sediments under weakly suboxic to anoxic-ferruginous conditions with shallow

pore water H_2S may produce a false-euxinic (very high) Mo/U signature. However, true euxinic conditions in an open ocean setting where water mass exchange occurs continuously—thereby providing a continuous replenishment of trace metals into reducing bottom water environments—also produces high Mo/U ratios when Mo reduction to sediments is more efficient than U reduction.

Particulate Mn (and Fe) are not preserved in non-oxic environments and therefore directly accounting for their activity in ancient non-oxic sediment is not possible. To resolve if the elevated Mo/U ratios are a result of particulate activity or highly efficient Mo removal to sediments under euxinic conditions without a particulate shuttle, I propose the use of a V–Mo covariation plot. Molybdenum and V are alike in that they are particle-reactive and require H_2S for reduction to sediments. Vanadium is much more efficiently adsorbed to both Mn *and* Fe (whereas Mo is only effectively adsorbed to Mn) particulates (Tribovillard et al., 2006), by more than a factor of 3 when normalized to dissolved concentrations (Ostrander et al., 2019), but Mo and V are both efficiently reduced to sediments under euxinic conditions. Therefore, if only weak particulate shuttle activity is occurring in a water column over euxinic bottom waters, the authigenic V/Mo ratio should approach the average seawater V/Mo ratio. If a particulate shuttle is active and H_2S is present in bottom or pore waters, an enrichment of authigenic V with respect to Mo is anticipated as particulates deliver excess V, and to a lesser extent Mo to the bottom waters and sediments.

To quantify particulate enrichment, particulate V and Mo concentrations from various locations, depths and dates in the Baltic Sea water column (Bauer, et al., 2017) are invoked. Bauer et al. (2017) also report particulate Mn and Fe concentrations. Two groups of samples were distinguished based on particulate Fe and Mn concentrations (**Figure 18**): (1) samples with low Fe content (0.52–8.3 ng/g), wide-ranging Mn concentrations (0.12–78 ng/g), poor Fe–Mn correlation ($r^2 = 0.26$) and low Fe/Mn weight ratios (< 6); and (2) samples with high Fe content (6.9–362 ng/g), low to moderate Mn content (0.22–8.0 ng/g) and good Fe–Mn correlation ($r^2 = 0.74$) and high Fe/Mn weight ratios (> 16). Group 1 is interpreted to consist of Mn-(oxy)hydroxide particles with minimal Fe incorporation, and group 2 is interpreted as ferromanganese particles.

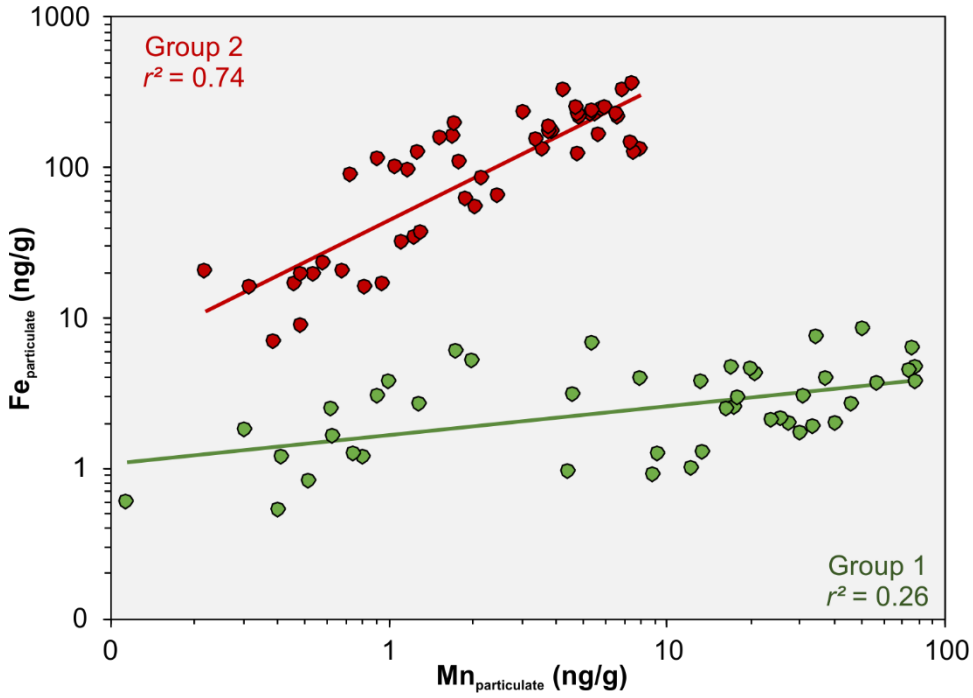

Figure 18. **Fe–Mn covariation for Baltic Sea particulates.** Particulate Fe and Mn data from Bauer et al. (2017) illustrate two groups of particulate samples: (1) those with low Fe and a wide range of Mn concentrations, interpreted as Mn-(oxy)hydroxides (green markers); and (2) those with correlated Fe and Mn concentrations with higher Fe and a smaller range of Mn concentrations, interpreted as Fe-Mn-(oxy)hydroxides (red markers).

Mean $V/Mo_{particulate}$ weight ratios are calculated for the two groups at 0.39 ± 0.29 (n = 45) for group 1 and 10.3 ± 6.8 (n = 51) for group 2, which are represented as linear trends on a V–Mo covariation plot (**Figure 19**). Several group 1 samples deviate from their V/Mo average, climbing towards the group 2 trend and falling below the average seawater V/Mo ratio. On average, V is much less concentrated in seawater than Mo (V/Mo weight ratio of 0.2; Tribovillard, et al., 2006). The samples which climb towards higher V/Mo ratios are those that were collected from the upper water column ("Surface Zone"), where oxygen concentrations are elevated and there is no H_2S present. These samples may have attained the higher V/Mo ratios if V(V) oxyanions were more efficiently adsorbed to particulates than Mo(VI) oxyanions under the fully oxic conditions. Samples which fall to lower V/Mo ratios were collected from the lower water column ("Bottom-water Zone") approaching the sediment–water interface. In the Bottom-water Zone, euxinia is encountered (H_2S; no O_2) triggering reductive dissolution of the particulates and subsequent desorption of trace metal oxyanions. The Fe/Mn ratio is greater in these samples than in other manganese particulates, perhaps because reductive dissolution under euxinia renders Mn soluble, while Fe reacts with H_2S to form pyrite. While sulfur

concentrations are not reported in Bauer et al. (2017), if Fe reacted to form pyrite it is possible that these are FeS_2 particulates rather than Fe-Mn oxyhydroxides. Under euxinic conditions, Mo tends to form sulfides unaccompanied (MoS_2) or in the presence of Fe (incorporated into pyrite) so if the particulates are pyritic, they would retain Mo more than V producing the decreased V/Mo ratios observed. Therefore, while some group 1 samples deviate from the mean, these are not representative of the true V/Mo ratios associated with Mn particulates.

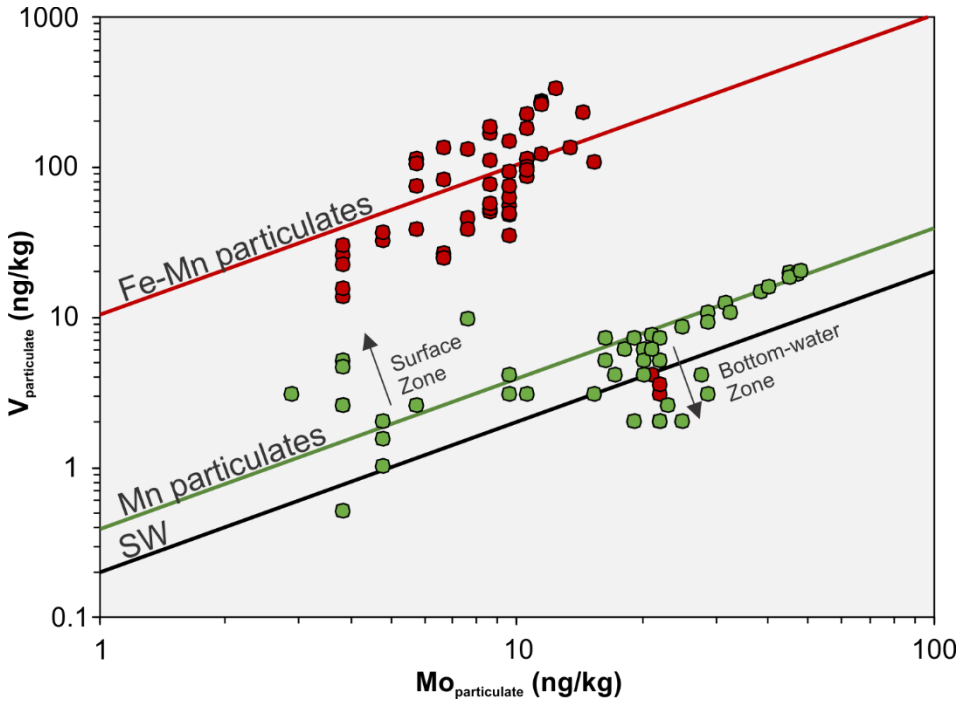

Figure 19. **V–Mo covariation for Mn and Fe-Mn particulates from the Baltic Sea.** V and Mo concentrations on Mn and Fe-Mn particulates from various locations, water depths and times in the Baltic Sea (data from Bauer, et al., 2017). Depicted V/Mo trends for Mn and Fe-Mn particulates are based on means for group 1 and group 2, respectively. "Surface Zone" and "Bottom-water Zone" are defined by depths above and below the water column redox zone (Bauer et al., 2017), where O_2 is highest in the surface zone with no H_2S, and no O_2 and high H_2S concentrations are reported in the Bottom-water Zone. SW = seawater (V/Mo weight ratio).

In **Figure 17a**, the issue of possible particulate shuttle activity arises for the Gordondale Member Lower Unit and euxinic Upper Unit samples where their Mo/U_{EF} ratios lie in both the open marine and particulate shuttle trends around the 3-times seawater weight ratio. A V–Mo covariation plot was constructed to confirm or eliminate the possibility of the particulate activity. The V/Mo_{EF} of the samples in question (approximated by yellow oval) demonstrate that the samples that experienced elevated Mo/U_{EF} were not Mo-enriched by particulate activity because they fall at or below the seawater V/Mo weight ratio (V/Mo_{SW}),

indicating non-particulate euxinia. It is possible that non-euxinic Upper Unit and PCS samples may have been affected by particulate activity because V/Mo_{EF} lies above V/Mo_{SW} and approaches the mean Mn particulate V/Mo weight ratio from the Bauer et al. (2017) samples. These samples are interpreted as ferruginous to suboxic therefore if Mn-particulate shuttles were operating, H_2S would have been present in pore waters at a shallow enough depth to capture V and Mo delivered by particulates. However, because interpretation of these samples by trace metal enrichments and Mo/U_{EF} covariations indicated ferruginous to suboxic settings, there is no issue with false-euxinia caused by particulates, and if there was Mn particulate activity it was too weak to mask paleoredox conditions.

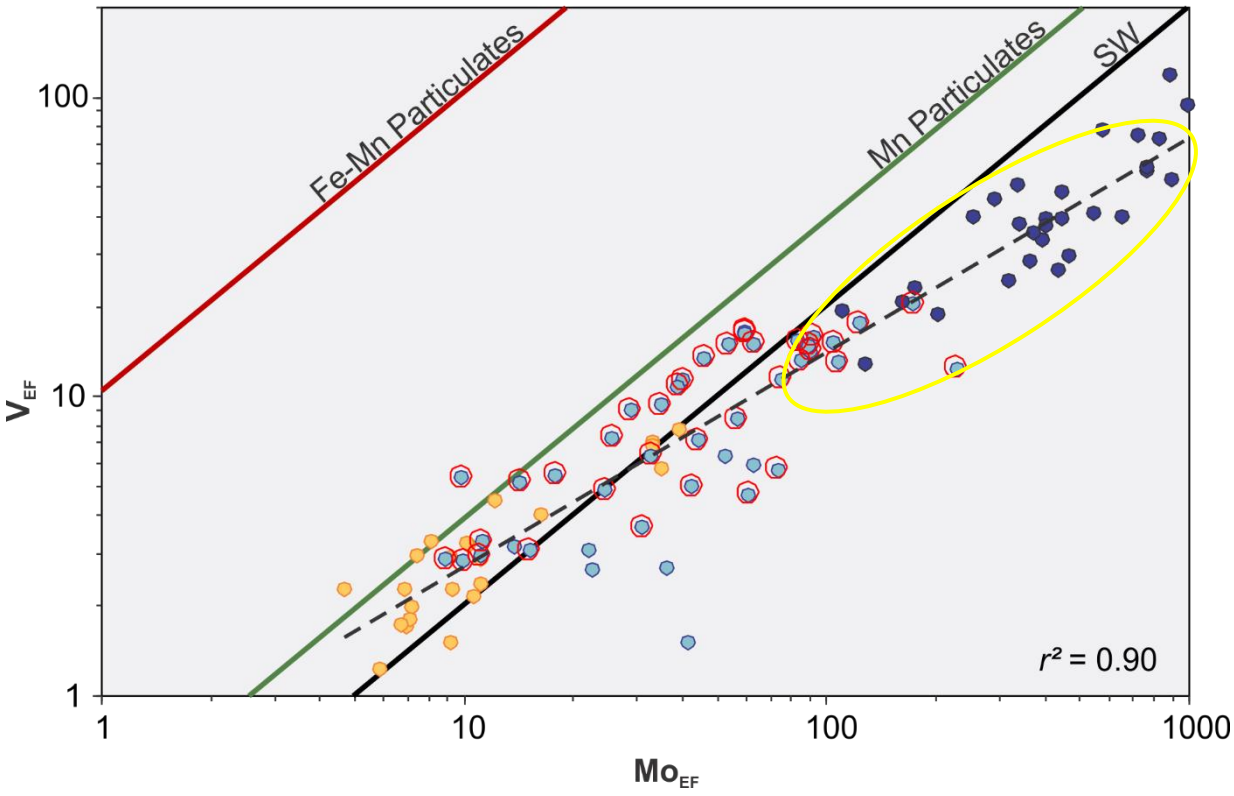

Figure 20. **V–Mo covariation with Gordondale Member and PCS samples.** Gordondale Member Lower Unit (dark blue), Upper Unit (light blue) and PCS (orange) samples plotted in relation to modern seawater (SW) V/Mo weight ratio of 0.20, and Mn and Fe-Mn particulate trends from Bauer et al. (2017) particulate trace metal V/Mo weight ratios.

To further understand and utilize the V/Mo ratio as a paleoredox proxy, validation of the trends suggested in this work should be completed on modern bottom-water sediments underlying regions of active particulate shuttling (e.g. Baltic Sea, Cariaco Basin) and sediment from areas with weak particulate activity to provide a baseline.

7.3.6. Local Environment Summary and Application of Global Mass Balance Models

The local depositional redox and hydrographic conditions were inferred using a multi-proxy approach. Paleoredox conditions were interpreted from concentrations of Mo, V, U, Re and ratios of Re/Mo and S_{tot}/Fe. The Gordondale Member was subdivided into Lower and Upper subunits which were interpreted as mainly euxinic and ferruginous–euxinic, respectively. The PCS was observed as a single unit and interpreted as mainly suboxic to weakly ferruginous. Both the Gordondale Member and PCS were likely deposited in an environment which was open to global water mass circulation based on trends from the Mo–U and Cd–Mo covariation plots.

The T-OAE, which occurred during the deposition of these units, was likely a period when bottom water anoxia and euxinia expanded to cover a greater area of the global seafloor. To quantify the hypothesised expansion, global mass balance models for Re (Sheen, et al., 2018) and Mo (Reinhard, et al., 2013) can be applied to locally anoxic (for Re model) or euxinic (for Mo model) samples which were deposited in a basin connected to the global ocean. Thus, most samples from the Gordondale Member can be used in the mass balance model calculations to reconstruct the global area of anoxic or euxinic seafloor in the Early Jurassic. Due to its suboxic to weakly ferruginous deposition, the PCS is not a candidate for global ocean reconstruction using the Re or Mo models.

7.4. Global Paleoredox Environment

In the global oceans, trace metal seawater concentrations are regulated by input fluxes from rivers and seafloor hydrothermal activity and output fluxes to oxic, suboxic and anoxic/euxinic seafloor sediment sinks. The anoxic/euxinic sinks are where trace metals like Re and Mo are removed most efficiently, as indicated by higher trace metal burial rates. Therefore, an expansion of the anoxic/euxinic sink areas will result in an increased drawdown of the metals from the seawater, thereby reducing their global seawater concentrations over time. First-order trace metal mass balance models for Re and Mo take advantage of the source–seawater–sink relationship to characterise ancient environments by their seafloor anoxic and euxinic sink areas (A_{anoxic} and $A_{euxinic}$), respectively (Sheen et al., 2018; Reinhard et al., 2013). These mass balance models are used here to determine the possibility of an expansion of A_{anoxic} and $A_{euxinic}$ during the T-OAE recorded in the study core.

7.4.1. Data Filtering and Grouping

Samples used in the mass balance models must have been deposited under locally anoxic (for Re) or euxinic (for Mo) conditions in an environment where global ocean water mass exchange occurred continuously to ensure that any changes in Re or Mo concentrations are not caused by basin restriction effects. Based on Mo–U and Cd–Mo covariations, the Gordondale Member/PCS basin was deposited in an open marine environment where water mass exchange with the global ocean could occur freely, therefore paleoredox interpretations of these strata reflect global ocean trace metal systematics.

Sheen et al. (2018) applied a filter of Fe/Al > 0.5 for anoxia which is not used here. The Fe/Al filter suggested by Sheen et al. (2018) is based on the global average shale Fe/Al ratio (~0.5; Lyons & Severmann, 2006), but local oxic background can range from 0.3 to 0.8, so may not reflect the average ratio (Clarkson, et al., 2014). If the local oxic background is less than the average shale Fe/Al ratio, then using this global average will mask enrichments. Thus, the Fe/Al ratio is not used to filter for anoxia in the study core. Sheen et al. (2018) use a C_{org} filter (C_{org} > 0.4 wt%) that prevents spurious Re/C_{org} values in organic-poor rocks, but the Gordondale Member and PCS are both organic-rich (C_{org} > 2.6 wt%) so the filter does not eliminate samples. The filters that are applied to determine sample anoxia in this study are the same as those used to determine local anoxia as discussed in **section 7.3.3**; these are U_{EF} > 3.6 (after Partin, et al., 2013) and Re_{EF} > 100 (after Crusius, et al., 1996).

Reinhard et al. (2013) apply filters of Fe, Al and C_{org} > 1 wt%, Fe/Al > 0.5, and Fe_{py}/Fe_{HR} > 0.7 or DOP > 0.6 to infer euxinic samples. The 1 wt% threshold for Fe and Al is not applied here as its original use in Reinhard et al. (2013) was to identify fine-grained siliciclastic sediments from a large (n > 3000) dataset. As discussed above, Clarkson et al. (2014) illustrate a wide range in Fe/Al at local levels (0.3 to 0.8), and thus using the average shale ratio of 0.5 may mask sample enrichments so the Fe/Al filter is not applied. The study core samples do not have Fe-speciation data available to determine Fe_{py}/Fe_{HR} or DOP. In addition to the anoxic proxies discussed in the above paragraph, the local euxinic proxies discussed in **section 7.3.3** are used here to filter samples; these are V_{EF} > 3 (after Quinby-Hunt and Wilde, 1994) and S_{TOT}/Fe > 1.15 (stoichiometric pyrite weight ratio).

Sample filtering resulted in a subset of samples for Re (n = 69) and Mo (n = 56) mass balance models (**Figure 21**). Two PCS samples passed anoxic sample filters, and one passed euxinic filters, but these not discussed because while they represent short anoxic/euxinic periods, they are not representative of the entire interval (thus n_{Re} = 67, n_{Mo} = 55).

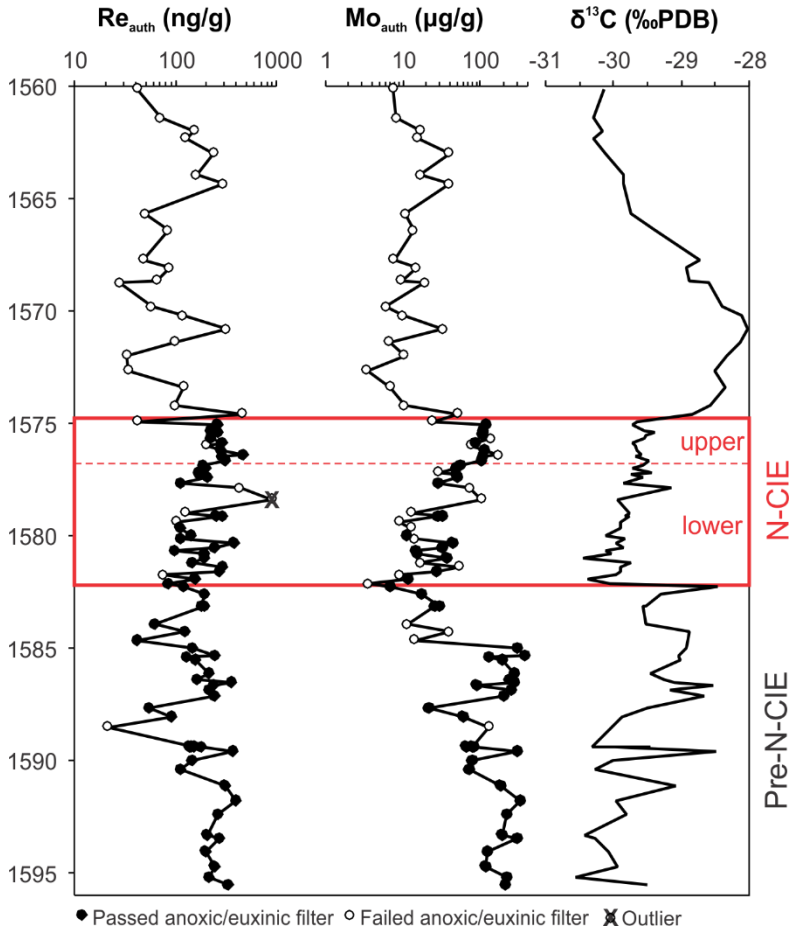

Figure 21. **Filtered anoxic/euxinic sample profile.** Samples which passed the filtering criteria for anoxia or euxinia are represented by black circles. Samples which failed to meet filtering criteria are represented by unfilled circles. One outlier sample in the Re_{auth} profile is marked by an 'X' and is discussed in the text. Samples are grouped stratigraphically into those which were deposited before the N-CIE ("Pre-N-CIE") and during the N-CIE ("lower N-CIE" and "upper N-CIE").

One outlier sample is present in the filtered Re data ($Re_{outlier}$ = 878 ng/g versus $Re_{filtered}$ = 233 ± 148 ng/g). The outlier was sampled from a black shale interval (1578.34 m) deposited closely between two turbidites (sampled at 1578.08 and 1578.53 m) (**Figure 22**). The enrichment of Re in the outlier compared to the background in the immediate core interval may be attributed to the deposition of the turbidites. The turbidites are substantially enriched in Mn (849 ± 181 µg/g) versus background levels (167 ± 121 µg/g). Manganese precipitates under

oxic conditions (Calvert & Pedersen, 1996), so Mn enrichment may be indicative of an oxic, Mn-rich turbidite source environment (McKay & Pedersen, 2014) or turbidity-induced bottom water oxygenation with post-turbidite accumulation of Mn-carbonate phases (Calvert & Pedersen, 1996). Turbidite deposition may have resulted in oxygenation of the top portion of underlying, previously-anoxic sediments. This may have led to oxidative mobilisation and redistribution of trace metals (e.g. Re, Mo, V, U) through diffusion into the newly emplaced turbidite sediment and further into the water column, or concentrated re-precipitation at the oxic–anoxic boundary within the underlying marine sediment. Initial oxic conditions would be replaced by anoxia as oxygen was exhausted by organic matter decomposition within the sediment, further immobilising trace metals (McKay & Pedersen, 2014). It is at the initial pore water oxic–anoxic boundary underlying the turbidite where the substantial Re enrichment in the outlier sample is postulated to have occurred. Thus, the outlier would have been a result of the upper turbidite (1578.08 m) deposition. No sample point was acquired within close enough proximity to the base of the lower turbidite (1578.53 m) to determine if this scenario occurred with every turbidite emplacement event. Therefore, Re enrichment in the outlier sample is likely a result of turbidite-induced Re redistribution and $Re_{outlier}$ is not included in the Re mass balance model (n = 68). The $Re_{filtered}$ becomes 213 ± 91 ng/g. The Mo concentration of the outlier sample is also enriched; however, the sample was eliminated during euxinic data filtering due to a very low S_{TOT}/Fe ratio (0.38).

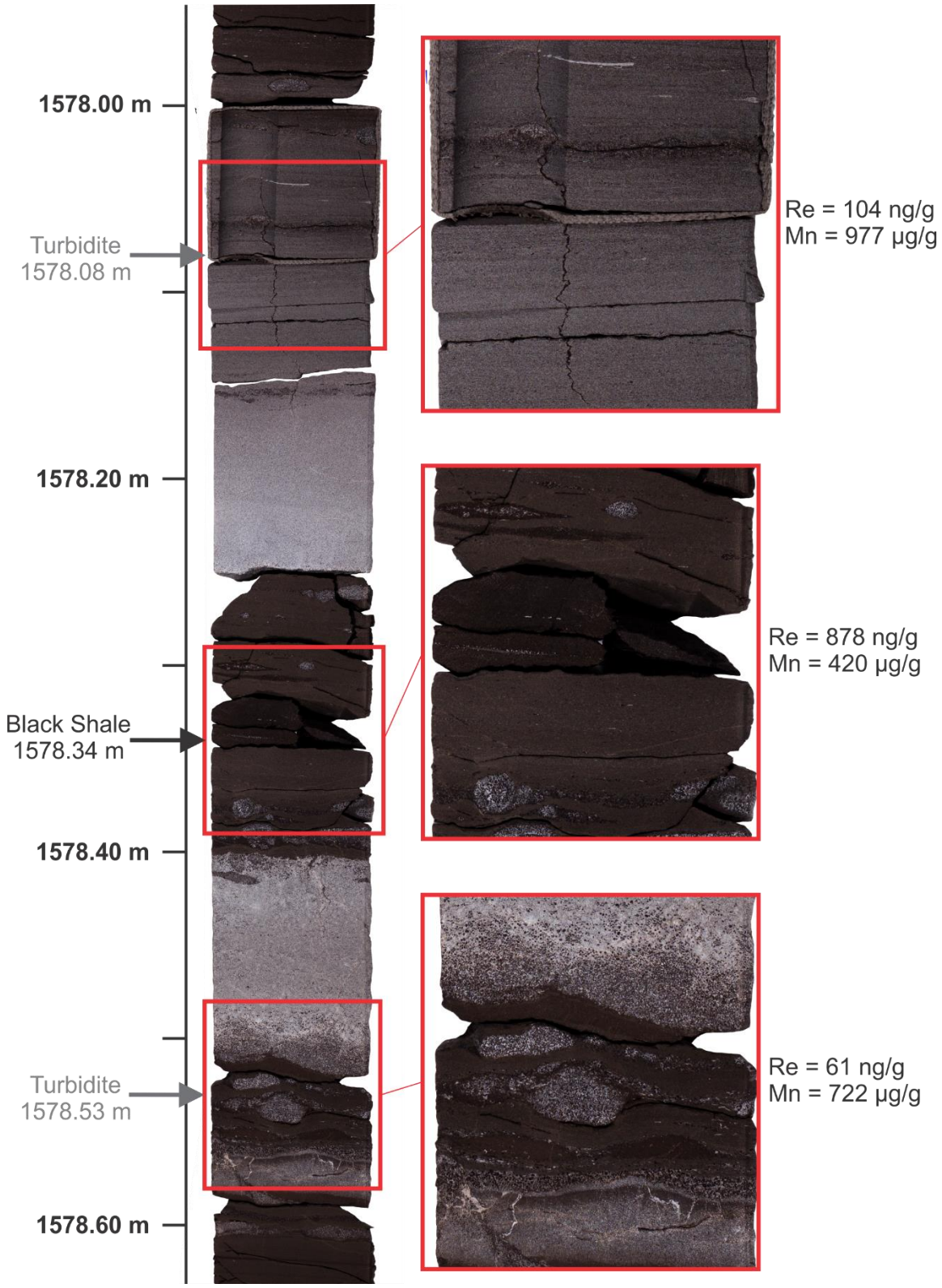

Figure 22. **White light photograph of $Re_{outlier}$ and turbidite interval.** Photos on the right are ± 5 cm centred around sample location and magnified by a factor of 2 with respect to the continuous core photo on the left. The turbidite at 1578.53 m may represent a mixture of turbidite and black shale material.

The mass balance models are used to determine if A_{anoxic} and/or $A_{euxinic}$ expanded or contracted through the T-OAE. To observe changes, samples are grouped stratigraphically (**Figure 21**). The "Pre-N-CIE" group includes samples of the Gordondale Member Lower Unit and lower portion of the Upper Unit (deeper than 1582.10 m). The "N-CIE" group includes samples of the Upper Unit within the N-CIE interval (1582.10 to 1575.00 m). Rhenium and Mo variation from lower concentrations at the onset of the N-CIE (1581.85 to 1576.82 m) to higher concentrations in the latter portion of the N-CIE (1576.59 to 1575.00 m) is observed, so the interval is split into "lower N-CIE" and "upper N-CIE" sections. **Table 6** denotes mean authigenic Re and Mo concentrations (Re_{auth}, Mo_{auth}; **Equation 13**) of the filtered samples in the stratigraphic groups.

(13) $$X_{auth} = X_{sample} - \left(\frac{X}{Al}\right)_{UCC} \times Al_{sample}$$

Where X_{auth} is the authigenic enrichment of the metal (X), X_{sample} is the measured concentration of X in the sample, the X/Al_{UCC} ratio is the trace metal to aluminium ratio in the Upper Continental Crust (McLennan, 2001), and Al_{sample} is the aluminium concentration measured in the sample.

Table 6. **Mean Re_{auth} and Mo_{auth} of filtered sample data for mass balance models.** Pre-N-CIE group includes samples from 1594.66–1583.89 m, lower N-CIE from 1582.10–1580.27 m and upper N-CIE from 1576.41–1575.00 m. Means reported to 1 standard deviation.

	Pre-N-CIE	N-CIE	
		Lower	Upper
Re_{auth} (ng/g)	192 ± 86 (*n* = 35)	187 ± 74 (*n* = 21)	278 ± 70 (*n* = 10)
Mo_{auth} (µg/g)	156 ± 104 (*n* = 32)	32 ± 14 (*n* = 15)	104 ± 9 (*n* = 8)

Unpaired t-tests assuming equal variance for Re (i.e. standard deviations between groups lie within a narrow range between 70 and 86 ng/g) and unequal variance for Mo (i.e. standard deviations between groups lie within a wide range between 9 and 104 µg/g) were performed on the sample groups to resolve statistical distinctiveness. Significant difference between the group means are inferred from p-values < 0.05, whereas p-values > 0.05 imply no statistical difference between the groups. Resulting p-values (**Table 7**) indicate that Re_{auth} concentrations are not significantly different between the Pre-N-CIE and lower N-CIE groups (p-value = 0.83), while the upper N-CIE group differs from both the Pre-N-CIE and lower N-

CIE groups (p-values < 0.006). All groupings of Mo_{auth} show significant difference (p-values < 0.009).

***Table 7. p*-values between groups of filtered Re_{auth} and Mo_{auth} data.** Results for Re are listed in the upper right (blue shading) and Mo in the bottom left (red shading). The Re_{auth} means between the Pre-N-CIE and lower N-CIE are the only pair which are statistically similar.

p-values	**Pre-N-CIE**	**Lower N-CIE**	**Upper N-CIE**
Pre-N-CIE		0.83	0.006
Lower N-CIE	1.42×10^{-7}		0.003
Upper N-CIE	0.009	2.6×10^{-12}	

7.4.2. Use of Published Models

Rhenium concentrations > 187 ng/g for the sample groups do not plot on the Re_{auth} axis as presented in Sheen et al. (2018), so the axis is extended to include enrichments up to 200 ng/g (**Figure 23**). The Pre-N-CIE A_{anoxic} of 0.12% is followed by a 1.3× increase to the lower N-CIE where A_{anoxic} is 0.16%; this is not likely a significant change given that the group means are not statistically different (p-value = 0.83). There is a contraction from lower to upper N-CIE, as inferred from an increase in the Re_{auth}, however, because the model as presented in Sheen et al. (2018) only captures values up to 205 ng/g (as $A_{anoxic} \rightarrow 0$), the A_{anoxic} for the upper N-CIE cannot be quantified.

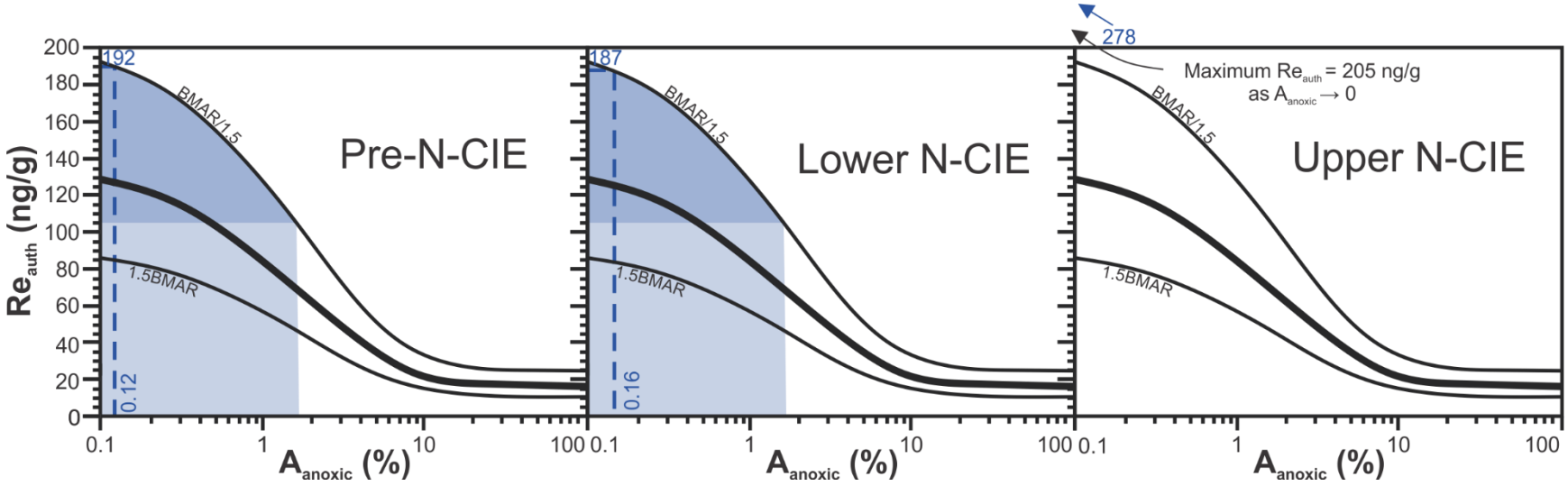

***Figure 23*. Re$_{auth}$ vs. A$_{anoxic}$ from mass balance models as published in Sheen et al. (2018).** The published model assumes modern riverine input flux, model initiation at mean modern continental margin sink burial rates, variation of burial rates with anoxic expansion based on a fit to eTOPO ocean bathymetry, constant suboxic seafloor area, Cariaco Basin bulk mass accumulation rate (thick black line) and factors of 1.5 above and below it (thin black lines). Dashed blue lines are mean Re$_{auth}$ for the given interval and their corresponding A$_{anoxic}$ at $^{1}/_{1.5}$ of the Cariaco Basin BMAR. Blue shading is ± 1s around the mean Re$_{auth}$ and corresponding range of A$_{anoxic}$.

The Mo mass balance model as presented in Reinhard et al. (2013) (**Figure 24**) does better to express the range and variation of $A_{euxinic}$ for the current study's sample group mean Mo values than did the Re model (**Figure 23**). The Pre-N-CIE group is the only one with a substantial enough Mo enrichment to extend beyond the scope of the presented model. An extension of the Mo_{auth} axis indicates the 156 µg/g Mo corresponds to an $A_{euxinic}$ of 0.18%. The decrease in Mo_{auth} in the lower N-CIE group corresponds to an $A_{euxinic}$ of 3.2% at Cariaco Basin BMAR. This represents an increase by a factor of ~18 from Pre-N-CIE $A_{euxinic}$. The upper N-CIE group corresponds to an $A_{euxinic}$ of 0.55% and a decrease to ~⅙ lower N-CIE $A_{euxinic}$.

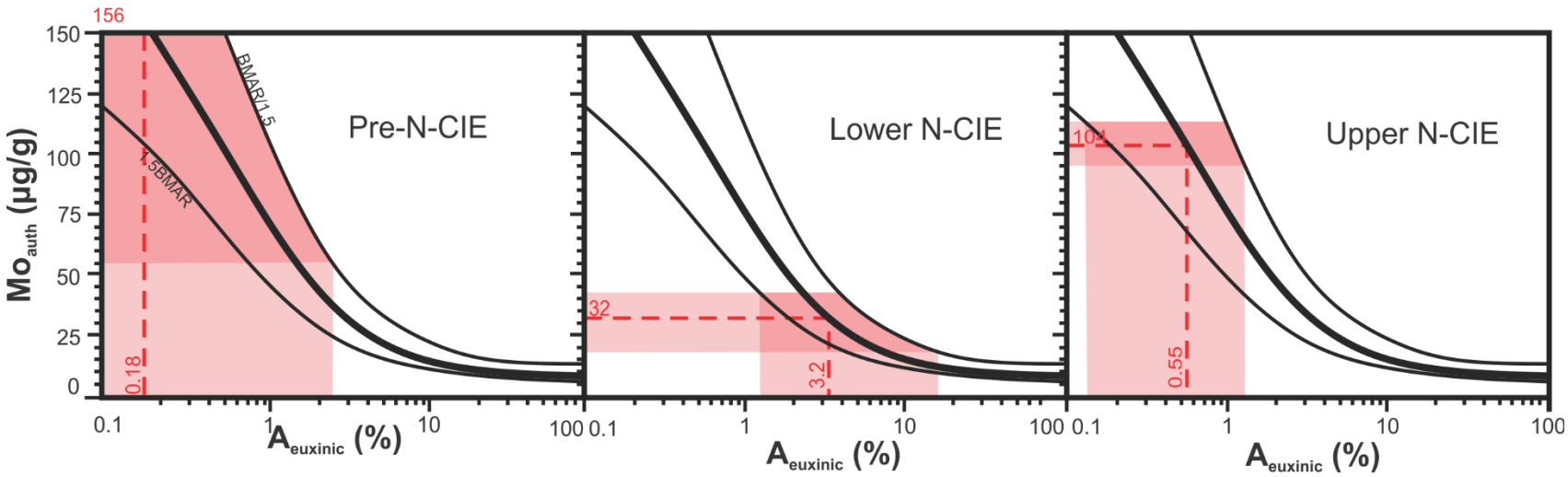

Figure 24. **Mo$_{auth}$ vs. A$_{euxinic}$ from mass balance models as published in Reinhard et al. (2013).** The model presented in their publication assumes modern riverine input flux, model initiation at mean modern continental margin sink burial rates, variation of burial rates with euxinic expansion based on a fit to eTOPO ocean bathymetry, modern sink burial rates, constant suboxic seafloor area, bulk mass accumulation rate of the Cariaco Basin (thick black line) and factors of 1.5 above and below it (thin black lines). Dashed red lines are mean Mo$_{auth}$ for the given interval and their corresponding A$_{euxinic}$. Red shading is ± 1s around the mean Mo$_{auth}$ and corresponding range of A$_{euxinic}$.

7.4.3. Addressing Model Parameters 1: Bulk Mass Accumulation Rate

Sheen et al. (2018) and Reinhard et al. (2013) illustrate their models using a Cariaco Basin bulk mass accumulation rate (BMAR) of 1.0×10^{-2} g cm^{-2} yr^{-1} and factors of 1.5 above and below. While this provides an ample range for possible A_{anoxic} and $A_{euxinic}$, a closer approximation of the local depositional BMAR can be calculated for an interval by **Equation 14** assuming continuous sedimentation, where ρ_b is mean bulk density (g cm^{-3}), Δz is vertical interval length (cm) and Δt is the interval duration (yr).

(**14**) $$BMAR = \frac{\rho_b \Delta z}{\Delta t}$$

The ρ_b for samples within the N-CIE interval is 2.42 ± 0.16 g cm^{-3} which is recorded in the study core between depths of 1575.00 m and 1582.10 m, or Δz of 710 cm. Bulk densities were determined at Weatherford Labs in 2016 during routine core analysis by determining sample weight (g) and using a mercury pump to determine bulk volume (cm^3). The N-CIE has an estimated Δt of 300 to 500 kyr (Sell et al., 2014; Boulila et al., 2014). By **Equation 14** with the standard deviation (1s) propagated from ρ_b and averaged between Δt endmembers, the N-CIE interval BMAR is $4.6 \pm 0.2 \times 10^{-3}$ g cm^{-2} yr^{-1} (~½ Cariaco Basin BMAR). The ρ_b for samples within the entire Gordondale Member interval including the N-CIE is 2.45 ± 0.14 g cm^{-3} which lies in the study core between depths of 1575.00 m and 1595.51 m or Δz of 2051 cm. Gordondale Member Δt is estimated as 10 ± 3.9 Myr (Pana et al., 2018a). By **Equation 14** with 1s propagated from ρ_b and Δt, the BMAR of the Gordondale Member interval is $5.0 \pm 2.0 \times 10^{-4}$ g cm^{-2} yr^{-1} (~$1/_{20}$ Cariaco Basin BMAR). It is unlikely that the very low BMAR calculated over the entire Gordondale Member is representative, as discontinuities and sediment starvation (Asgar-Deen, 2003) would not have recorded the entire time interval. Thus, the Sheen et al. (2018) and Reinhard et al. (2013) models are modified to reflect the BMAR range of the N-CIE interval in **Figure 25** and **Figure 26**, respectively.

Additionally, Reinhard et al. (2013) suggest that BMAR and authigenic burial rate (*b*) should not be decoupled arbitrarily. However, because the model burial rates are a global average at a given depth (calculated from an initial state and varying with eTOPO ocean bathymetry) and the BMAR is a local property, the burial rates are not varied from the values used in the published models.

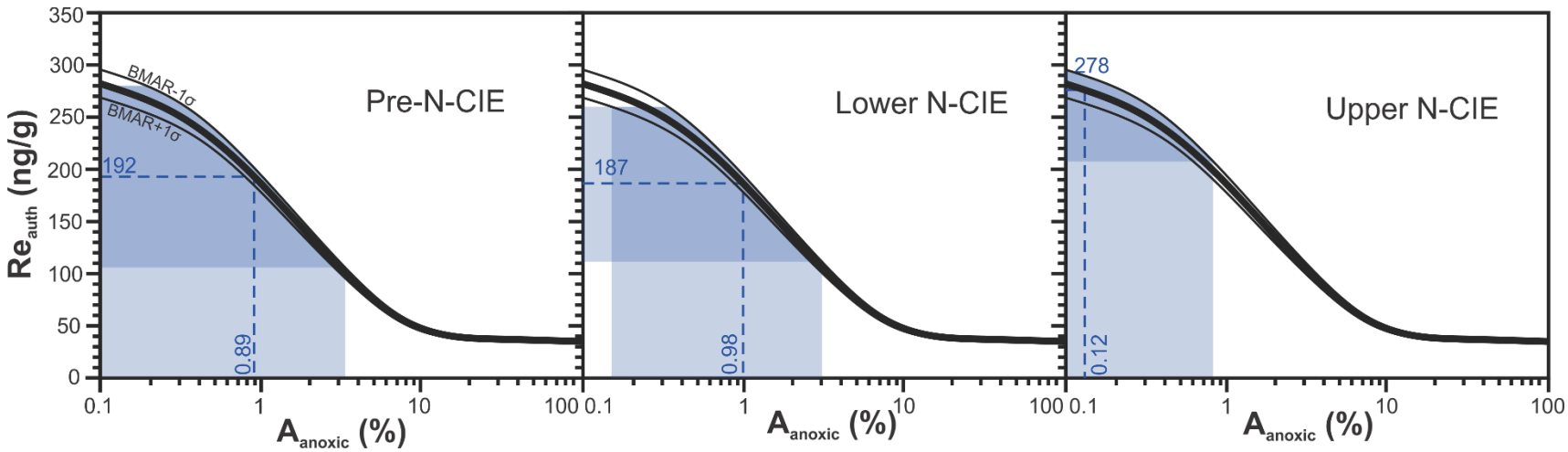

Figure 25. **Re_{auth} vs. A_{anoxic} modified to reflect local BMAR.** The mass balance model of Sheen et al. (2018) is modified to account for the local depositional BMAR of 4.6×10^{-3} g cm^{-2} yr^{-1} calculated for the N-CIE interval, and is plotted as a thick black line. One standard deviation (1s) above and below local BMAR ($\pm 0.2 \times 10^{-3}$ g cm^{-2} yr^{-1}) are plotted as thin black lines. Dashed blue lines represent the group's mean Re_{auth} and corresponding A_{anoxic}. Blue shaded areas are ±1s from the mean Re_{auth} and corresponding A_{anoxic} (darker area is overlap).

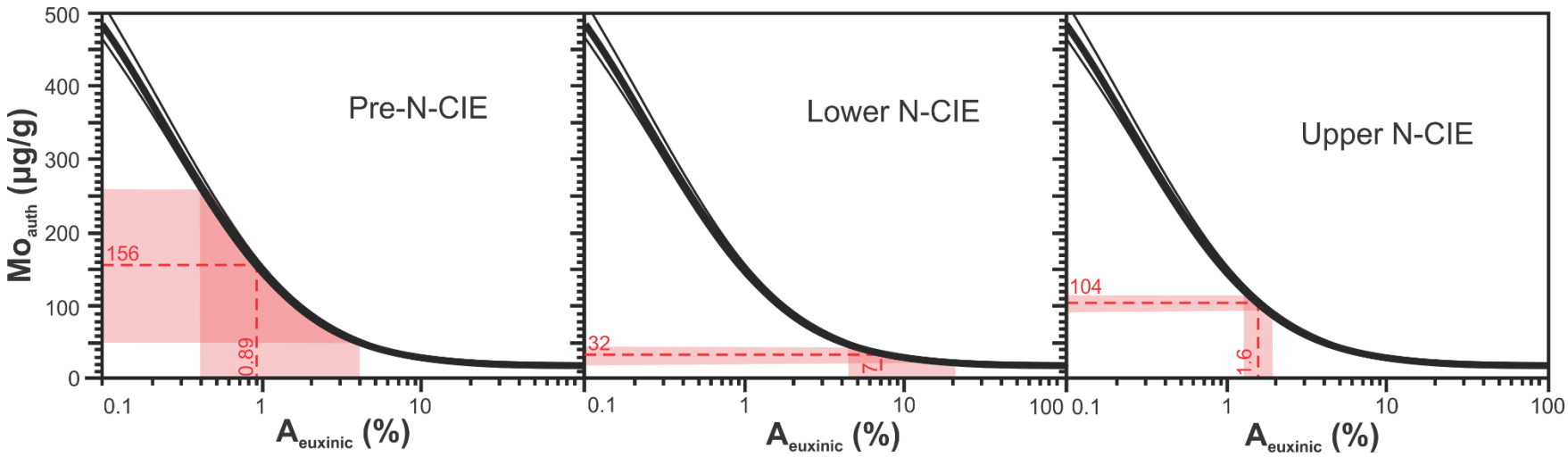

Figure 26. **Mo_{auth} vs. $A_{euxinic}$ modified to reflect local BMAR.** The mass balance model of Reinhard et al. ***(2013)*** is modified to account for the local depositional BMAR of 4.6×10^{-3} g cm^{-2} yr^{-1} calculated for the N-CIE interval, and is plotted as the central thick black line. One standard deviation (1s) above and below local BMAR ($\pm 0.2 \times 10^{-3}$ g cm^{-2} yr^{-1}) are plotted as thin black lines. Dashed red lines are the mean Mo_{auth} for the groups and corresponding $A_{euxinic}$; red boxes are ±1s.

Lowering BMAR from Cariaco Basin to local values results in the models shifting to include higher Re_{auth} and Mo_{auth}. A minor variation exists between Re_{auth} in the Pre-N-CIE and lower N-CIE sample groups, where A_{anoxic} of the former is 0.89% and the latter is 0.98% (**Figure 25**); ~1.1× increase in A_{anoxic}. This expansion is not likely significant, given that the two groups have mean Re_{auth} that are not statistically different (p-value = 0.83). A contraction of –0.86% A_{anoxic} from the lower N-CIE (0.98%) to upper N-CIE (0.12%) is observed. Using Mo, a similar trend of $A_{euxinic}$ expansion from Pre-N-CIE to lower N-CIE, and contraction from lower to upper N-CIE is noted in **Figure 26**. Pre-N-CIE $A_{euxinic}$ is 0.89% and lower N-CIE $A_{euxinic}$ is 7%; a 7.8× increase. The contraction from the lower to upper N-CIE interval is observed as $A_{euxinic}$ in the upper N-CIE diminishes to 1.6%, which is $¼.4$ the $A_{euxinic}$ of the lower N-CIE.

7.4.4. Addressing Model Parameters 2: Input Flux

In Sheen et al. (2018) and Reinhard et al. (2013), riverine input is the major trace metal source flux (F_{in}) to the modern oceans supplying 4.29×10^5 mol Re and 3.00×10^8 mol Mo per year. Both models consider hydrothermal inputs but infer that modern high temperature (T) hydrothermal–seawater interactions constitute < 0.1% and < 1%, and low T hydrothermal inputs comprise < 1% and < 10% of the Re and Mo modern riverine fluxes, respectively. Therefore, total hydrothermal fluxes for Re and Mo constitute 1.1% and 11% of the modern riverine fluxes, respectively. The hydrothermal fluxes are poorly constrained and based on their minor contribution to source flux compared to riverine input are not a component of F_{in} within the published models.

A seawater Sr isotope ($^{87}Sr/^{86}Sr$) excursion to less radiogenic values is reported from the Pliensbachian–Toarcian (Pl–To) boundary to the onset of the T-OAE (Jones & Jenkyns, 2001). The shift to less radiogenic $^{87}Sr/^{86}Sr$ suggests decreased continental granitic or carbonate (more radiogenic) weathering, increased continental flood basalt (less radiogenic) eruption and weathering, and/or increased submarine hydrothermal activity (less radiogenic) (Jones & Jenkyns, 2001). Jones and Jenkyns (2001) discuss the relative importance of each process to the Early Jurassic $^{87}Sr/^{86}Sr$ excursion. They suggest that a global sea level rise could decrease land area and as a result, produce lower continental weathering rates. However, a sea level transgression (Toarcian) post-dates the excursion, thus, decreased continental weathering

was likely not an important factor in producing the excursion (Jones & Jenkyns, 2001). The emplacement of the Karoo–Ferrar LIP flood basalts (~183 Ma) also postdates the $^{87}Sr/^{86}Sr$ excursion (191–187 Ma), so increased Sr flux from subaerial basalt weathering and runoff is also unlikely (Jones & Jenkyns, 2001). Jones and Jenkyn's (2001) numerical models demonstrated that the $^{87}Sr/^{86}Sr$ excursion could be caused solely by an 8% to 86% increase of ocean ridge hydrothermal activity. Their model assumes that riverine flux and $^{87}Sr/^{86}Sr$ remained constant through the excursion. The wide range in the model results are mainly due to the dependence on initial high T hydrothermal Sr flux and the ratio of low T to high T hydrothermal Sr input.

If the Re and Mo hydrothermal fluxes respond similarly to the Sr flux during enhanced seafloor hydrothermal fluxes, then their total hydrothermal fluxes for the modern ocean underestimate the fluxes leading up to the T-OAE. If the hydrothermal components are doubled (rounded up from a maximum hydrothermal Sr flux increase of +86%), then the hydrothermal fluxes for Re and Mo become 2.2% (9.44×10^3 mol Re yr^{-1}) and 22% (6.79×10^7 mol Mo yr^{-1}) of their riverine input flux. If riverine flux in the Early Jurassic is assumed to be the same as modern, the new total F_{in} becomes 4.38×10^5 mol Re yr^{-1} and 3.77×10^8 mol Mo yr^{-1}. For Re, the change in flux is minor (figure not shown; A_{anoxic} is the same as no hydrothermal increase as in **Figure 25**) but for Mo the flux increases enough that a new model provides slightly modified results (**Figure 27**). The local depositional BMAR calculated in **section 7.4.3** was applied in this model.

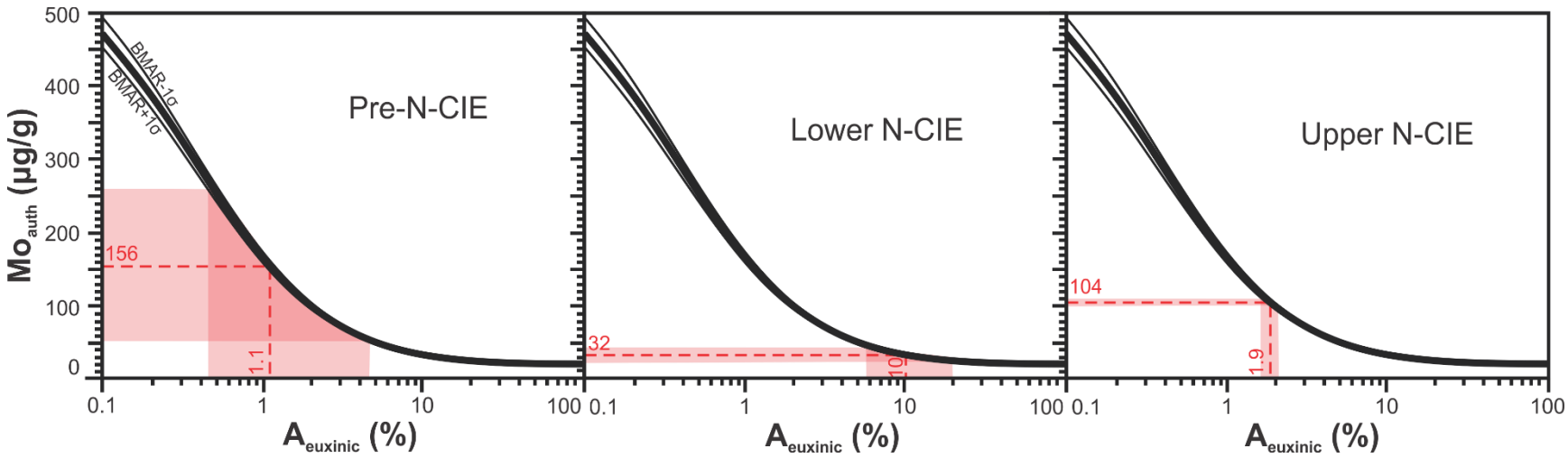

Figure 27. **Mo$_{auth}$ vs. A$_{euxinic}$ modified to reflect a 2× increase in hydrothermal activity.** The mass balance model of Reinhard et al. (2013) is modified to account for the local depositional BMAR of 4.6×10^{-3} g cm^{-2} yr^{-1} calculated for the N-CIE interval, and is plotted as the central thick black line. One standard deviation (1s) above and below local BMAR ($\pm 0.2 \times 10^{-3}$ g cm^{-2} yr^{-1}) are plotted as thin black lines. Dashed red lines are the mean Mo$_{auth}$ for the groups and corresponding A$_{euxinic}$; red boxes are ±1s.

The $A_{euxinic}$ attained by the sample groups in the hydrothermal model in **Figure 27** (1.1–10% $A_{euxinic}$) are greater than those attained with the assumed modern riverine flux alone (as in **Figure 26**; 0.89–7% $A_{euxinic}$). The trend of increasing $A_{euxinic}$ between the Pre-N-CIE and lower N-CIE and decrease from the upper to lower N-CIE is still observed.

Others have suggested that the switch to radiogenic seawater $^{87}Sr/^{86}Sr$ ratios coinciding with the N-CIE is indicative of higher (or greater relative proportion of) riverine flux to the oceans during the T-OAE (Jenkyns, 2010). This is matched by a positive sedimentary Os isotope ($^{187}Os/^{188}Os$) excursion from low background (~0.4) to a peak (~1.0) at the onset of the N-CIE (Them II, et al., 2017b; Percival, et al., 2016; Cohen, et al., 2004), and a negative Ca isotope ($\delta^{44/40}Ca$) excursion in foraminifera shells from background (~0‰) to low values (~ –1.6‰) at the onset of the N-CIE (Brazier, et al., 2015). Both Sr and Ca have long seawater residence times (5.1 Myr and 1.1 Myr, respectively; Broecker & Peng, 1982), so are slower to respond to environmental perturbations compared to Os which has a shorter residence time (1 to 10 kyr; Rooney, et al., 2016). Numerical models of the $^{187}Os/^{188}Os$ and $\delta^{44/40}Ca$ excursions have yielded estimated continental weathering rate increases of 3× to 6× (Them II, et al., 2017b), 5× to 9× (Cohen, et al., 2004) and 5× (Brazier, et al., 2015). The upper ranges of the estimated weathering rate increases are extreme scenarios (Cohen, et al., 2004) or an effect of local environmental changes (Jenkyns, 2010), so the moderate 3× continental input from the $^{187}Os/^{188}Os$ model by Them et al. (2017b) is applied to the F_{in} term in the Re and Mo mass balance models (**Figure 28** and **Figure 29**).

The increased continental weathering event occurred over 100 to 200 kyr (Them II, et al., 2017b), less than the assumed residence times of Mo (440 kyr; Miller, et al., 2011), meaning that the seawater Mo reservoir (and thus recorded sedimentary Mo_{auth}) may not be fully equilibrated in the study core section with respect to the new input. The Re residence time is shorter (128 kyr; Miller, et al., 2011), so it is likely that the seawater Re reservoir equilibrated by the end of the weathering event. It is assumed that an increase in weathering rate corresponds to an equivalent increase in riverine sediment mass flux to the oceans. Additionally, it is also assumed that trace metal riverine mass flux increased proportionally to sediment mass flux so the new Re and Mo F_{in} are 1.29×10^6 mol and 9.26×10^9 mol per year, respectively.

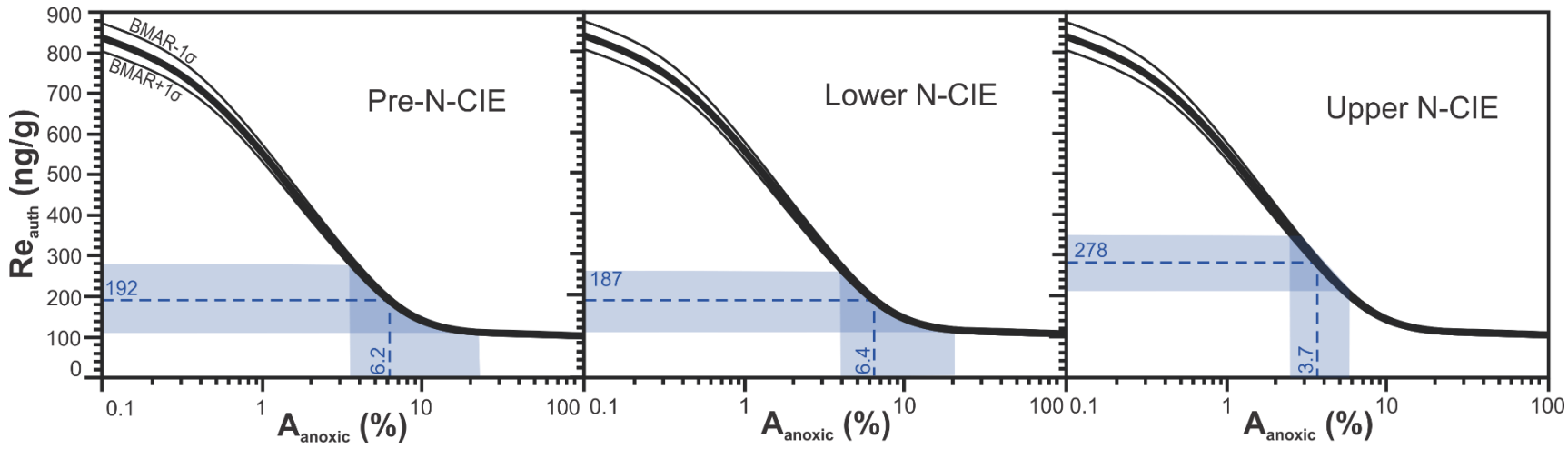

Figure 28. **Re_{auth} vs. A_{anoxic} reflecting a 3× increase in riverine F_{in}.** The mass balance model after Sheen et al. (2018) accounting for local depositional BMAR of 4.6×10^{-3} g cm^{-2} yr^{-1} as calculated for the N-CIE interval is plotted as the central thick black line. One standard deviation (1s) above and below local BMAR ($\pm 0.2 \times 10^{-3}$ g cm^{-2} yr^{-1}) are plotted as thin black lines. Dashed blue lines are the mean Re_{auth} for the groups and corresponding A_{anoxic}; blue boxes are ±1s.

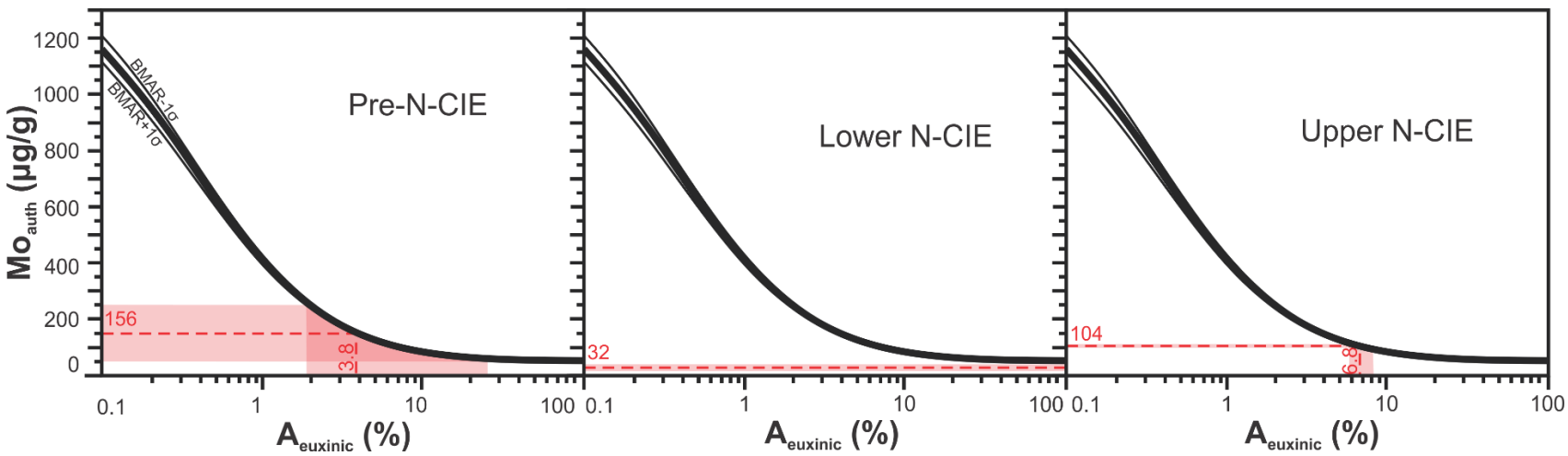

Figure 29. **Mo_{auth} vs. $A_{euxinic}$ modified to reflect a 3× increase in riverine F_{in}.** The mass balance model after Reinhard et al. (2013) accounting for local depositional BMAR of 4.6×10^{-3} g cm^{-2} yr^{-1} as calculated for the N-CIE interval is plotted as the central thick black line. One standard deviation (1s) above and below local BMAR ($\pm 0.2 \times 10^{-3}$ g cm^{-2} yr^{-1}) are plotted as thin black lines. Dashed red lines are the mean Mo_{auth} for the groups and corresponding $A_{euxinic}$; red boxes are ±1s.

An increased riverine flux boosts the authigenic enrichments attainable in the models. The trend of increasing A_{anoxic} from Pre-N-CIE to lower N-CIE (+0.2%), and a decreasing A_{anoxic} from lower N-CIE to upper N-CIE (–2.7%) is observed in **Figure 28**. This trend is only partially observed in **Figure 29**, as lower N-CIE mean Mo_{auth} does not plot on the euxinic model because it is below the minimum Mo_{auth} of 52 µg/g. A relative increase in $A_{euxinic}$ from Pre-N-CIE to lower N-CIE and relative decrease in $A_{euxinic}$ from lower to upper N-CIE can be inferred from the relative decrease and increase in group mean Mo_{auth}, respectively.

7.4.5. Addressing Model Parameters 3: Sink Areas

In Sheen et al. (2018) and Reinhard et al. (2013), a constant, modern $A_{suboxic}$ of 4.67% and 1.92%, respectively, was used to simplify modelling with three unknown sink areas. A constant $A_{suboxic}$ has been assumed through the previous sections. With $A_{suboxic}$ held constant, A_{anoxic} increases only at the expense (a loss) of A_{oxic}. In this section, an alternative scenario is presented to address the intermediate suboxic sink. This scenario assumes an expansion of suboxia proportionally to an expansion of anoxia/euxinia until the point where A_{oxic} (and the neutral bottom water area) is 0%, after which $A_{suboxia}$ contracts relative to the continued expansion of $A_{anoxic/euxinic}$ (i.e. as the difference between global seafloor area and $A_{anoxic/euxinic}$) (**Figure 30** and **Figure 31**, green line).

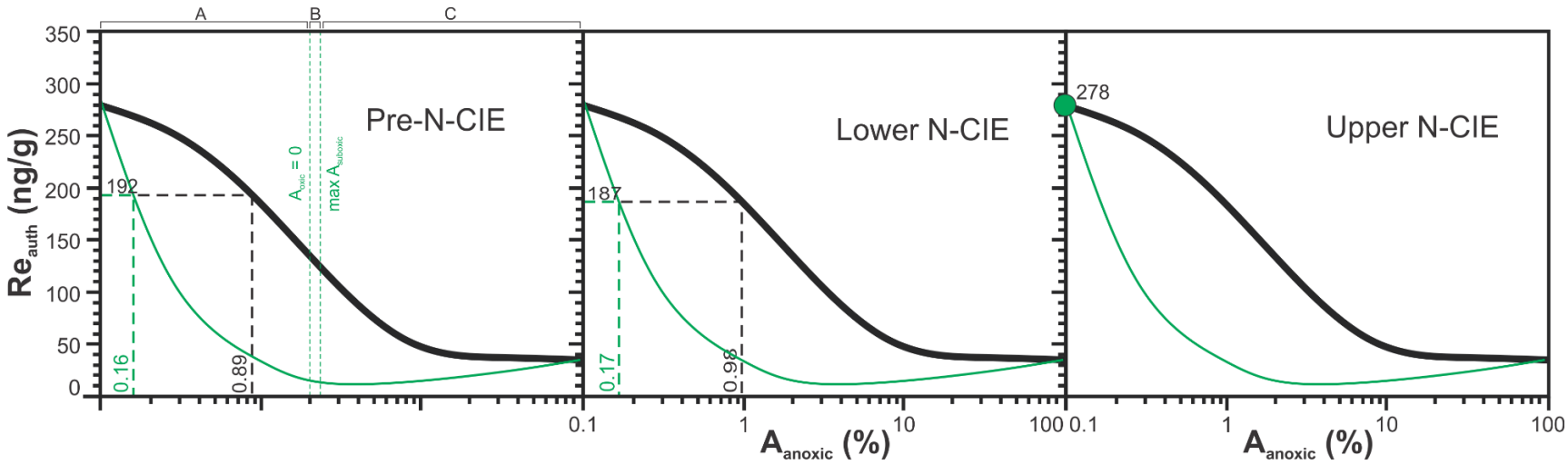

Figure 30. **Re_{auth} vs. A_{anoxic} modified to reflect variations in $A_{suboxic}$.** Thick black line represents the model based on Sheen et al. (2018) with BMAR changed to local depositional and $A_{suboxic}$ remaining constant. Green line represents a scenario where (**A**) $A_{suboxic}$ increases proportionally to increasing A_{anoxic} until A_{oxic} decreases to 0, at which point (**B**) $A_{suboxic}$ increases until $A_{suboxic} + A_{anoxic} = 100\%$ ($A_{oxic} + A_{neutral} = 0\%$), then (**C**) $A_{suboxic}$ decreases relative to increasing A_{anoxic} with their sum constant at 100%. Black dashed line is the mean Re_{auth} corresponding to an A_{anoxic} for the model with constant $A_{suboxic}$ (see also **Figure 25**). Green dashed line is the mean Re_{auth} corresponding to an A_{anoxic} for the scenario described with varying $A_{suboxic}$.

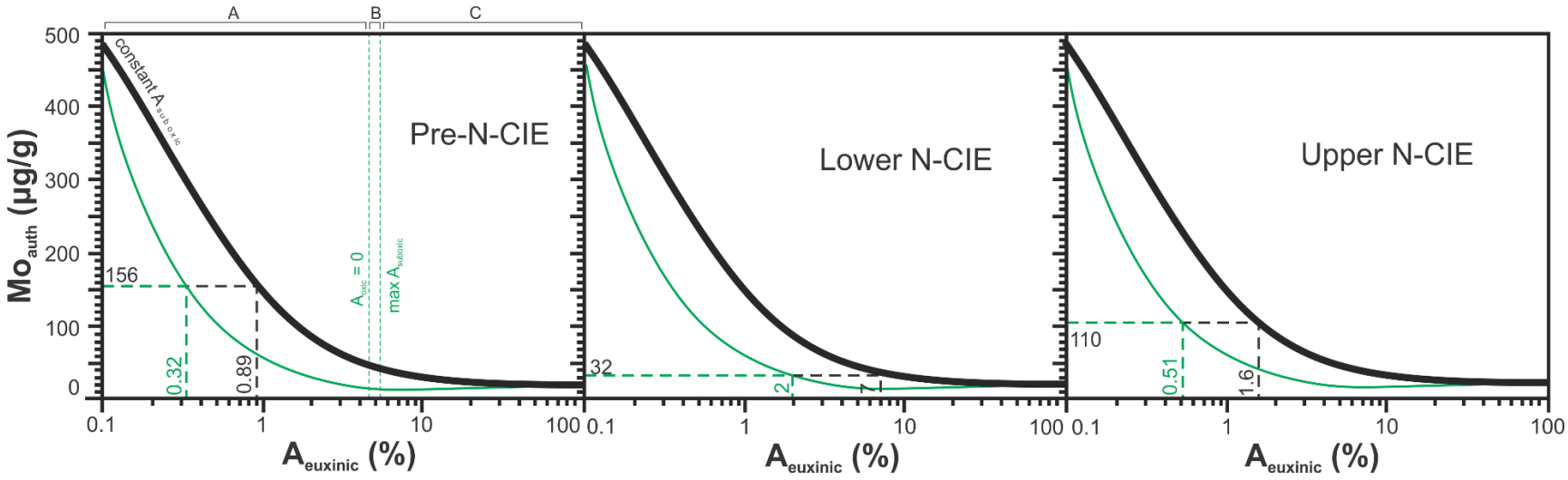

Figure 31. **Mo_{auth} vs. $A_{euxinic}$ modified to reflect variations in $A_{suboxic}$.** Thick black line represents the model based on Reinhard et al. (2013) with BMAR changed to local depositional and $A_{suboxic}$ remaining constant. Green line represents a scenario where (**A**) $A_{suboxic}$ increases proportionally to increasing A_{anoxic} until A_{oxic} decreases to 0, at which point (**B**) $A_{suboxic}$ increases until $A_{suboxic} + A_{euxinic} = 100\%$ ($A_{oxic} + A_{neutral} = 0\%$), then (**C**) $A_{suboxic}$ decreases relative to increasing $A_{euxinic}$ with their sum constant at 100%. Black and green dashed lines are the mean Mo_{auth} corresponding to an $A_{euxinic}$ for the corresponding models.

The scenario where $A_{suboxia}$ initially increases proportionally to A_{anoxic} and $A_{euxinic}$ creates a steeper initial drawdown of Re and Mo because the burial rate of the suboxic seafloor ($b_{suboxic}$) is more efficient than oxic seafloor (less than b_{anoxic} or $b_{euxinic}$, but more than b_{oxic}). Thus, as both A_{anoxic} or $A_{euxinic}$ *and* $A_{suboxic}$ increase, the overall burial of Re and Mo increases and seawater becomes depleted more rapidly, resulting in lower authigenic enrichments with each model iteration. No statistical change in A_{anoxic} is observed between the Pre-N-CIE (0.16%) and lower N-CIE (0.17%), which is anticipated based on minimal variation of Re_{auth} between sample groups. However, a minor contraction from lower to upper N-CIE groups is inferred as the upper N-CIE A_{anoxic} decreases to 0.10% from the lower N-CIE A_{anoxic} of 0.17%. For $A_{euxinic}$, an increase from Pre-N-CIE to lower N-CIE (+1.7%) and decrease from lower to upper N-CIE (–1.5%) is observed here as it has been in previous model cycles.

7.4.6. Addressing Model Assumptions: Steady-state versus Non-steady-state

In the **section 7.4.4**, the hypothesis was presented that a Pliensbachian hydrothermal flux increase (based on a negative Sr isotope excursion) was followed by an increase in continental weathering flux (based on positive Sr and Os, and negative Ca isotope excursions) during the Toarcian. The models in that section treated each situation independently, i.e. model scenarios with a hydrothermal *or* riverine flux increase were applied to all intervals (Pre-N-CIE, lower and upper N-CIE) and comparisons were made within each scenario. However, based on the Sr (plus Os and Ca) isotope excursions, the hydrothermal and continental weathering flux increases are temporally-exclusive phenomena in the Early Jurassic. The switch from increased hydrothermal flux to increased weathering flux occurs broadly across the onset of the N-CIE. Therefore, it is more fitting to compare the Pre-N-CIE increased hydrothermal model scenario (**Figure 25** and **Figure 27**) with the lower N-CIE increased riverine model scenario (**Figure 28** and **Figure 29**). The lower and upper N-CIE intervals are compared within the increased riverine flux model (**Figure 28** and **Figure 29**) because they both occurred within the N-CIE and continental weathering Sr, Os and Ca isotope excursions. This model therefore mimics an instantaneous increase in riverine flux at the N-CIE boundary, rather than a gradual onset over 100–200 kyr (Them et al., 2017b).

The same trends observed in the previous model cycles are observed here, however the changes are more dramatic due to the larger A_{anoxic} and $A_{euxinic}$ attained from the increased

continental weathering/riverine input scenario. The A_{anoxic} increases by ~7× from Pre-N-CIE (0.89%) to lower N-CIE (6.4%) and decreases by ~½ in the upper N-CIE (3.7%). The $A_{euxinic}$ from Pre-N-CIE to lower N-CIE and lower to upper N-CIE is not quantified because the Mo_{auth} of the lower N-CIE fell below plottable values, but a relative increase followed by a relative decrease are inferred from a relative decrease and increase of Mo_{auth}, respectively.

7.4.7. Discussion of Mass Balance Modelling Results

Several models with parameter variations have been presented in the previous sections, the results of which are summarized in **Table 8**. Sensitivity testing in the previous sections has illustrated the qualitative competence of the models through consistent interpretation of expansion or contraction between intervals in all model scenarios. An expansion of A_{anoxic} and $A_{euxinic}$ is observed between the Pre-N-CIE and lower N-CIE, followed by a contraction from the lower to upper N-CIE. This trend is supported by Tl isotope work on another WCSB section suggesting that the greatest A_{anoxic} occurred at the onset of the N-CIE, although development of anoxia likely began before the N-CIE (Them II, et al., 2018). From the results of the Re mass balance modelling in this study, the expansions and contractions of A_{anoxic} are limited. The exception to the minor increases from Pre-N-CIE to lower N-CIE is in the non-steady state model scenario (#4), where a large A_{anoxic} increase between the intervals is observed due to the modelled influx of weathered continental material in the lower N-CIE, but not the Pre-N-CIE. Much greater expansions and contractions of $A_{euxinic}$ are observed from the Mo mass balance models.

Table 8. **Variations in A_{anoxic} and $A_{euxinic}$ from Pre-N-CIE to lower N-CIE, and lower to upper N-CIE intervals during several model cycles.** Model scenarios are those presented in **sections 7.4.2** to **7.4.6** where model components are altered. From scenarios 1 to 4, model parameters are listed if they vary from the published model. Round-bracketed values are the modelled A_{anoxic} or $A_{euxinic}$ in % total seafloor area. Square-bracketed +/– are inferred from relative authigenic enrichment changes when Mo concentrations fell below model solutions.

Scenario	Model Parameters	Pre-N-CIE → lower N-CIE		lower N-CIE → upper N-CIE	
		A_{anoxic}	$A_{euxinic}$	A_{anoxic}	$A_{euxinic}$
Published models after Sheen et al. (2018) and Reinhard et al. (2013)	F_{in} = modern riverine (Riv_M) $A_{suboxic}$ = constant modern $A_{oxic} = A_{total} - A_{anoxic} - A_{suboxic}$ $b_{oxic,suboxic}$ = modern $b_{anoxic,euxinic}$ = modern, scaled **BMAR** = ± 1.5 × Cariaco	×1.3 (0.12→0.16)	×18 (0.18→3.2)	[–] (0.16→"0")	$\times 5.8^{-1}$ (3.2→0.55)
1) Local BMAR	**BMAR** = Calculated local	×1.1 (0.89→0.98)	×7.8 (0.89→7)	$\times 8.2^{-1}$ (0.98→0.12)	$\times 4.4^{-1}$ (7.0→1.6)
2a) Increasing F_{in} (Hydrothermal)	F_{in} = Riv_M + 2× modern hydrothermal **BMAR** = Calculated local	×1.1 (0.89→0.98)	×9.1 (1.1→10)	$\times 8.2^{-1}$ (0.98→0.12)	$\times 5.6^{-1}$ (10→1.8)
2b) Increasing F_{in} (Riverine)	F_{in} = 3×Riv_M **BMAR** = Calculated local	×1.03 (6.2→6.4)	[+] (3.8→"100")	$\times 1.7^{-1}$ (6.4→3.7)	[–] ("100"→6.8)
3) Increasing $A_{suboxic}$	$A_{suboxic}$ = ↑ ∝ ↑$A_{anoxic/euxinic}$, ↓$A_{suboxic}$ when $A_{suboxic} + A_{anoxic} \geq 100\%$ **BMAR** = Calculated local	×1.1 (0.16→0.17)	×6.3 (0.32→2)	$\times 1.7^{-1}$ (0.17→0.10)	$\times 3.9^{-1}$ (2.0→0.51)
4) Non-steady state F_{in}	F_{in} (Pre-N-CIE) = Riv_M + 2× hydrothermal F_{in} (N-CIE, lower & upper) = 3×Riv_M **BMAR** = Calculated local	×7.2 (0.89→6.4)	[+] (1.1→"100")	$\times 1.7^{-1}$ (6.4→3.7)	[–] ("100"→6.8)
General Variation in A_{anoxic} and $A_{euxinic}$		**Expansion**		**Contraction**	

The sensitivity testing completed on the models examined the effect of parameter variation on the general results of the model. Using the local BMAR from model scenarios #1 to #4 should increase the accuracy of the modelled A_{anoxic} and $A_{euxinic}$ for the sample intervals. Model scenarios #2a and #2b assume increases in hydrothermal and riverine inputs, respectively, which are likely to have occurred based on variations in Sr, Os and Ca isotope profiles of coeval sections (Them II, et al., 2017b; Percival, et al., 2016; Brazier, et al., 2015; Cohen, et al., 2004; Jones & Jenkyns, 2001). Model scenario #4 addresses the asynchrony between the hydrothermal versus riverine flux increases by observing a hydrothermal increase during the Pre-N-CIE interval, followed by the instantaneous application of a riverine increase for the lower and upper N-CIE intervals. A caveat of quantifying the A_{anoxic} and $A_{euxinic}$ from the model scenarios where input fluxes increase is that they are based on increases from an initial input equivalent to modern riverine flux, which may be an overestimate based on generally lower $^{87}Sr/^{86}Sr$ and $^{187}Os/^{188}Os$ Jurassic seawater ratios compared to modern (Them II, et al., 2017b; Jones & Jenkyns, 2001; Burton, et al., 1999). The accuracy of the A_{anoxic} and

$A_{euxinic}$ derived from model scenario #3 are difficult to assess as it is not documented how the suboxic sink reacts during anoxic/euxinic expansion and contraction.

An issue arises in the quantitative comparison of the anoxic and euxinic sinks, where the estimated $A_{euxinic}$ typically exceeds A_{anoxic}, especially in the lower N-CIE interval. This is problematic because the anoxic sink area is the sum of the ferruginous ($A_{ferruginous}$) and euxinic sinks, therefore $A_{euxinic} > A_{anoxic}$ is not possible. For example, in model scenario #2a, $A_{euxinic} > A_{anoxic}$ by ~9% in the lower N-CIE. Mathematically $A_{ferruginous}$ is therefore –9% to fulfill the summation, however a negative area is not physically possible. It is still likely that the extent of $A_{ferruginous}$ was limited during the T-OAE because reducing ocean conditions have produced euxinia, rather than ferruginous anoxic, since the mid-Paleozoic (Lenton, et al., 2018). However, minor episode of ferruginous anoxia in mid-depth waters is inferred in some locations by marine red bed deposition in association with OAEs, including in the European Middle Toarcian sequences following the T-OAE (Song, et al., 2017; Cecca, et al. 1992).

The extreme inferred expansion of $A_{euxinic}$ is a function of low Mo_{auth} in the lower N-CIE interval (32 ± 14 μg/g). While the lower N-CIE Mo_{auth} is representative of samples that passed filters for euxinia, it is possible that the relatively low values do not equate to an extreme global $A_{euxinic}$ expansion. I suggest that because the Mo residence time (τ_{Mo}) is longer than the continental weathering event occurring at the onset of the T-OAE, the Mo_{auth} is not responding as quickly to the influx of Mo from rivers and remains at non-steady state longer than Re_{auth} with a shorter residence time.

The τ_{Mo} of 440 kyr is longer than the estimated 100–200 kyr increase in continental weathering rate, therefore the initially low Mo_{auth} in the lower N-CIE may represent a non-equilibration of the Mo reservoir with respect to an influx of weathered continental material. The shorter τ_{Re} of 128 kyr (Miller, et al., 2011) may have allowed Re to respond more rapidly to a perturbation such as an influx of weathered continental material. This imbalance between the equilibration of the Mo and Re seawater reservoirs would ultimately affect the authigenic enrichments recorded in the sediments. The Mo_{auth} would be initially slow to respond to the influx and would record the more drawn-down seawater reservoir, producing an artificially-high $A_{euxinic}$ until the increased riverine flux could equilibrate with the sediment sink. The Re_{auth} may respond within the time frame of the continental weathering influx, so should be

recording near-equilibrium conditions, at least towards the latter half of the rate increase. It should be noted that residence time varies as a function of the seawater metal reservoir and its input fluxes, thus the modern τ_{Mo} and τ_{Re} may not be representative of those during the T-OAE. However, if Re and Mo seawater reservoirs and input fluxes change proportionally to each other (as they do within the models used here), then τ_{Re} will remain shorter than τ_{Mo}.

A second factor which may have affected the outcome of the mass balance models is that the samples are thermally overmature. In overmature environments, loss of organic carbon and retention of trace metals in the sediment phase may exaggerate the trace metal concentrations, and thus Re_{auth} and Mo_{auth} may have been artificially elevated. If this is the case, then the resulting A_{anoxic} and $A_{euxinic}$ from the modeled authigenic enrichments are underestimates. Riediger (1991) documented C_{org} up to 28 wt% in immature Gordondale Member cores, while the overmature samples in the study core contain maximum C_{org} content of 12 wt%. Thus, a potential organic matter loss of up to 60% is approximated. Using **Equation 15** (where Re and Mo are measured in ng/g and µg/g, respectively, and C_{org} is measured in wt% or g per 100 g), estimated pre-maturation Re and Mo concentrations can be calculated for each sample.

(15)
$$[Re\ or\ Mo]_{pre-maturation} = \frac{[Re\ or\ Mo]_{measured} \times 1g}{1g + {([C_{org}]_{measured} \times \frac{1}{100g})(0.60)}/{0.40}}$$

New mean Re and Mo concentrations for each model interval are calculated as follows: Pre-N-CIE, 162 ng/g Re and 140 µg/g Mo; Lower N-CIE, 166 ng/g Re and 30 µg/g Mo; Upper N-CIE, 247 ng/g Re and 97 µg/g Mo. These new values represent concentrations ~8% lower than measured concentrations and correspond to A_{anoxic} or $A_{euxinic}$ ~1 to 4% greater than those derived from measured values.

Finally, based on the assumption that low Mo_{auth} and therefore high $A_{euxinic}$ were exaggerated within the lower N-CIE, when $A_{euxinic} > A_{anoxic}$ for a given interval in a model scenario, the A_{anoxic} replaces the $A_{euxinic}$ because A_{anoxic} represents a maximum for $A_{euxinic}$. A new summary for model scenarios #2a, #2b and #4 is listed in **Table 9**, which highlights the more conservative estimates of changes in $A_{euxinic}$ versus the non-corrected values in **Table 8**.

Table 9. **Seafloor anoxic and euxinic areas updated to reflect $A_{anoxic} \geq A_{euxinic}$.** The original results presented in **Table 8** indicate $A_{euxinic} > A_{anoxic}$ in some cases, which is physically impossible. Based on the arguments discussed in the text, it is more suitable to assume that in the case where $A_{euxinic}$ was reported as greater than A_{anoxic}, the A_{anoxic} can be used in lieu. Bolded values are the new $A_{euxinic}$ for given intervals based on the A_{anoxic} for that interval.

Scenario	Pre-N-CIE → lower N-CIE		lower N-CIE → upper N-CIE	
	A_{anoxic}	$A_{euxinic}$	A_{anoxic}	$A_{euxinic}$
2a) Increasing F_{in} (Hydrothermal)	×1.1 (0.89→0.98)	**×1.1** (**0.89→0.98**)	×8.2^{-1} (0.98→0.12)	**×8.2^{-1}** (**0.98→0.12**)
2b) Increasing F_{in} (Riverine)	×1.03 (6.2→6.4)	**×1.7** (3.8→**6.4**)	×1.7^{-1} (6.4→3.7)	**×1.7^{-1}** (**6.4→3.7**)
4) Non-steady state F_{in}	×7.2 (0.89→6.4)	×7.2 (**0.89→6.4**)	×1.7^{-1} (6.4→3.7)	**×1.7^{-1}** (**6.4→3.7**)
General Variation in A_{anoxic} /$A_{euxinic}$	**Expansion**		**Contraction**	

In summary, the results of the mass balance models have illustrated that the T-OAE likely contained a period of moderate expansion of A_{anoxic} and $A_{euxinic}$ at the onset of the N-CIE interval, followed by a moderate contraction of these sink areas near the end of the N-CIE. Scenario #4 is the most probable, based on the changes to weathering rate inferred from Sr, Os, and Ca isotope studies. The anoxic sink area, which is a combination of the ferruginous and euxinic sinks was likely dominated by euxinia based on similar A_{anoxic} and $A_{euxinic}$ from the models. Therefore, seafloor A_{anoxic} and $A_{euxinic}$ ranged from less than 1% to a maximum of ~6% across the T-OAE.

The modern continental shelf and slope account for ~3.6% and ~5.6% of the global ocean area, a total of ~9.2% of the ocean floor area (Drake & Burk, 1974). If the area of the Toarcian continental shelf and slope were not substantially different than today, then the models suggest that expansion of anoxia and euxinia did not extend into the deep ocean but remained within the shallow continental margins, intracontinental basins and epicontinental seas. The deep oceans likely remained predominantly oxygenated.

The results of the Re and Mo mass balance models in this study are broadly consistent with estimations of an increase in euxinic seafloor area from ~0.6% (Early Toarcian 'Normal' conditions) to ~4% (T-OAE globally reducing conditions) based on Mo isotope variations (Pearce, et al., 2008). Thallium isotope variations have also been used to estimate the global area of bottom water anoxia based on a relative decrease in well-oxygenated bottom waters where Mn oxides are buried (Them II, et al., 2018). The Tl isotope model deviates from the Re and Mo models by the indication of a two-step deoxygenation through the T-OAE, with the

first instance requiring a 50% decrease in well-oxygenated seafloor area, and the second instance a further 25% decrease in well-oxygenated seafloor area. This variation between a single deoxygenation (Re and Mo models) and the two-step deoxygenation is likely caused by the different residence times of Re and Mo (both > 100 kyr) versus Tl (~ 20 kyr; Them II, et al., 2018). In Sheen et al. (2018) and Reinhard et al. (2013), the oxic seafloor sink (~84% of global seafloor area) is defined as the seafloor area where Mn oxides are permanently buried and O_2 penetration reaches sediment depths > 1 cm. The modern oxic sink includes both continental margin and abyssal plain areas of the ocean, while the modern suboxic (4.67%, Sheen, et al., 2018; 1.92%, Reinhard, et al., 2013) and anoxic (0.11%; Sheen, et al., 2018; Reinhard, et al., 2013) sinks are limited to the continental margins. It is unlikely that the 50% and 25% decrease in well-oxygenated seafloor occurred across the entire oxic sink area as classified by the Sheen et al. (2018) and Reinhard et al. (2013) models. Owens et al. (2018) describe a similar reduction of well-oxygenated seafloor (65-75%) from Tl isotopes during OAE2 (Cretaceous), which they infer to coincide with an increase of poorly-oxygenated to anoxic bottom waters across ~2× the continental margin area during OAE2. If it is assumed that the continental margin area during the T-OAE was equivalent to the modern (~9%), and the estimate of 2× continental margin is used to infer the expanded area of suboxia + anoxia/euxinia, this may correspond to an area of ~18%. With suboxia held constant as it was in the Re and Mo models, this equates to an anoxic/euxinic expansion between ~13–16%. The estimate from Them II et al. (2018) is greater than the estimate from the Re and Mo models, however, this may be linked to the shorter τ_{Tl} which can respond to anoxic expansion more rapidly.

7.5. Cause of Global Anoxic/Euxinic Expansion

The T-OAE is defined by abundant organic-rich black shale hosting a N-CIE embedded in a broader P-CIE (Jenkyns, 2010). The event is typically accompanied by redox-sensitive metal enrichments, featuring a drawn-down (less enriched) segment indicating potential expansion of anoxic or euxinic bottom waters (e.g. Them II, et al., 2018). In the previous section, mass balance models were applied to the study core hosting the T-OAE to determine if, and to what extent, ocean anoxia/euxinia expanded, contracted or remained constant. The model revealed a moderate expansion of anoxia and euxinia at the onset of the N-CIE,

followed by a minor contraction during the later part of the N-CIE. While the models illustrate the occurrence of the variations in bottom water anoxia and euxinia, they do not point to the cause of the event.

Many authors have used the synchrony of the Karoo–Ferrar LIP (~183–181 Ma; Burgess, et al., 2015; Sell, et al., 2014) with the onset of the T-OAE (~183 Ma) as evidence for its role in triggering the event. Geochronological overlap between the LIP and OAE events is enough to demonstrate their relationship, but some authors have suggested the use of a sedimentary Hg paleoproxy as direct evidence for volcanogenic input to the ocean water–sediment system at the global scale during the T-OAE (Them II, et al., 2019; Percival, et al., 2015; Sanei, et al., 2012). These studies have provided evidence that enhanced Hg deposition may have coincided with pulses of LIP activity or periods when LIP emplacement interacted with coals or organic-rich rocks (Percival, et al., 2015). Interaction with coals and organic-rich rocks would not only release Hg necessary for ocean sediment enrichment but would also inject thermogenic methane into the atmosphere, which is thought to be a factor producing the N-CIE signature of the T-OAE (Percival, et al., 2015; Kemp, et al., 2005; Hesselbo, et al., 2000). The first pulse of Hg enrichment occurred as early as the Pl–To boundary, which also coincides with a relatively negative $\delta^{13}C$ signature (Percival, et al., 2015).

In the study core, sediment Hg concentrations are normalised to C_{org} and S_{TOT} to account for host phase control on Hg deposition (**Figure 32**). Mercury deposition is typically mediated by organic matter so given a similar seawater Hg concentration, sediments in organic-rich environments will be more enriched versus organic-poor environments (Sanei, et al., 2012); thus, a C_{org} normalisation is warranted. Sanei et al. (2012) note a decoupling of Hg–C_{org} in their Permian section when euxinia is prevalent. Additionally, because Hg is often associated with thiol groups in organic matter as well as sulfide minerals, the sediment Hg concentration here is also normalised to S_{TOT}.

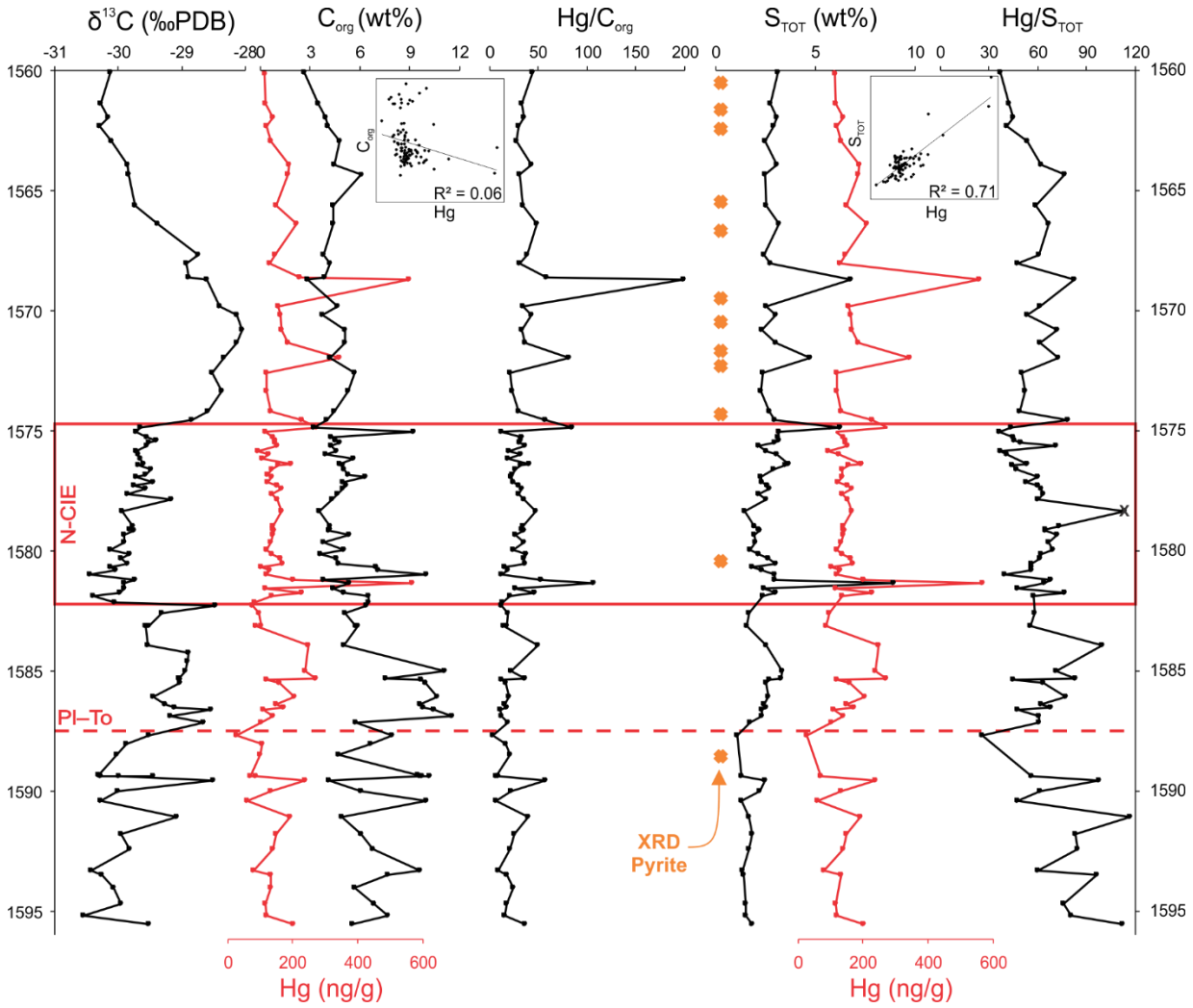

Figure 32. **Sediment Hg profiles.** The approximate Pliensbachian–Toarcian (Pl–To) boundary and N-CIE are assigned based on the $\delta^{13}C_{org}$ profile. Sediment Hg is normalised to C_{org} and S_{TOT} to account for host phase abundance. Based on the good Hg–S_{TOT} and poor Hg–C_{org} correlation, Hg deposition was most likely controlled by sulfides, not organic matter. X-ray diffraction evidence for pyrite is shown to demonstrate occurrence of pyrite with spikes in S_{TOT} (and Hg). An outlier resulting from turbidite deposition (see **section 7.4.1**) is marked by an 'X' and represents a low S_{TOT}, not a peak in Hg.

The Hg–C_{org} correlation is negligible (r^2 = 0.06), while the Hg–S_{TOT} correlation is good (r^2 = 0.71). As discussed in **section 7.1**, most metal–C_{org} correlations in the study core are poor likely from loss of organic mass during thermal maturation (Dickson, et al., 2019). It is probable that thermal maturation has affected the Hg–C_{org} correlation. Study of chemical equilibrium of Hg in solution with sulfide have shown that increasing dissolved sulfide content reduces Hg bioavailability, and thus in these environments Hg tends to complex with sulfides (Benoit, et al., 1999). The study core is greatly enriched in S_{TOT} (1 to 9 wt%), indicating that

there was likely an abundance of dissolved sulfide in the water column or pore water inhibiting Hg complexation with organic matter. Thus, the Hg–S_{TOT} normalisation is the best option in considering sediment Hg variations in response to volcanic activity.

Intervals of elevated Hg/S_{TOT} with respect to the mean for the core (62 ppb/wt%; n = 82) are observed below the Pl–To boundary and between the Pl–To boundary and the onset of the N-CIE. The outlier sample (1578.34 m) was likely affected by turbidite deposition—as was discussed for Re and Mo in **section 7.4.1—**and shows an elevated Hg/S_{TOT}, however no variation in Hg concentration from the surrounding samples is observed and both S_{TOT} and C_{org} are lower than the surrounding samples, so it is neglected as an indication of volcanic activity. The peak in sediment Hg and Hg/S_{TOT} near the Pl–To boundary is similar to observations in Them II et al. (2019) and Percival et al. (2015), however those studies typically observe greater enrichments within the N-CIE interval, rather than leading up to it.

Them II et al. (2019) link proximity of the study site to the ancient coast line as a control on sediment Hg enrichment. Of five distal cores examined in their compilation, none exhibited Hg/C_{org} anomalies. This study core is more seaward in relation to two “distal” Alberta cores studied in Them II et al. (2019), and along with overmaturity and complication in determining what phase the Hg resides (organic, sulfidic, or neither), the sediment Hg proxy for volcanic activity is deemed inconclusive for the study core. However, based on the synchrony of the Karoo–Ferrar LIP and the T-OAE supported by sediment Hg enrichments in proximal settings, and no other extreme perturbation (e.g. meteorite impact) recorded at the time, volcanic activity likely played a role in producing the T-OAE.

8. Conclusions

The Early Jurassic study core from northeastern British Columbia contains the Gordondale Member, overlain by the Poker Chip Shale (PCS). Both members are organic-rich (C_{org} up to 11.5 wt%) and overmature (Tmax > 470°C) in the study core. The Gordondale Member was divided into a Lower Unit which was euxinic (Mo and V up to 370 µg/g and 2237 µg/g, respectively), and an Upper Unit which had variably anoxic (non-sulfidic) and euxinic intervals (Mo and V up to 165 µg/g and 2166 µg/g, respectively; U and Re up to 33 µg/g and 878 ng/g, respectively). The Upper Unit contained the N-CIE of the T-OAE, exhibiting a –2‰ shift in the $\delta^{13}C_{org}$ signature. The PCS was mainly suboxic (U and Re up to 13 µg/g and 456 ng/g, respectively), however, pore waters may have remained sulfidic given moderate Mo and V enrichments (up to 40 µg/g and 606 µg/g, respectively) and its pyritic mineralogy.

Covariations of Mo–U and Cd–Mo indicated that the Gordondale and PCS were deposited in an open-marine environment where deep water mass exchange could occur regularly, and upwelling was a likely feature of this environment. Given this hydrographic configuration, the basin is suitable for trace metal mass balance modelling to determine the global extent of seafloor anoxia and euxinia. The Re and Mo mass balance models focused on anoxic and euxinic samples from the Gordondale Member, as the PCS was deemed suboxic. The Gordondale samples were divided into three groups relative to the occurrence of the N-CIE: (1) Pre-N-CIE, (2) lower N-CIE, and (3) upper N-CIE. The Pre-N-CIE group exhibited moderate authigenic Re and the highest Mo enrichments (192 ± 86 ng/g and 156 ± 104 µg/g, respectively). The lower N-CIE group had the lowest Re and Mo authigenic enrichments (187 ± 74 ng/g and 32 ± 14 µg/g, respectively), however, the Re content was not statistically different from the Pre-N-CIE group (p-value = 0.83). The upper N-CIE group had the highest Re and moderate Mo authigenic enrichments (278 ± 70 ng/g and 104 ± 9 µg/g, respectively).

Based solely on these enrichments, a minor expansion in the anoxic and euxinic seafloor areas between the Pre-N-CIE and lower N-CIE (from ~0.9% to ~1% total seafloor area), and a contraction from the lower to upper N-CIE (from ~1% to ~0.1% total seafloor area) are inferred. However, that is assuming that the trace metal ocean reservoir (and thus the authigenic enrichments) are responding only to changes in the anoxic and euxinic sediment sinks. The T-OAE was accompanied by > 3× increase in continental weathering rate which

occurred over the first 100 to 200 kyr of the 300 to 500 kyr N-CIE (Them II, et al., 2017b). This meant that a variation of the riverine input flux accompanied the expansion of the anoxic/euxinic seafloor sinks, thus a perturbation to the input flux by a factor-of-3 increase was applied to the lower and upper N-CIE intervals. This resulted in a corresponding increase in the anoxic/euxinic seafloor area necessary to produce the Re and Mo enrichments in the lower N-CIE (~6% total seafloor area) and upper N-CIE (~4% total seafloor area) sediments.

The scenario with the input flux increase was assumed to be the most representative of the Early Jurassic system, however, one issue arose due to the residence times of Re and Mo with respect to the timing of the weathering rate increase. Mo and Re have modern oceanic residence times of ~440 kyr and ~130 kyr, respectively (Miller, et al., 2011), while the weathering rate increase occurred over 100 to 200 kyr. The longer residence times of the trace metals means that they likely exhibit a delayed response to the perturbation, and thus may not have fully equilibrated during the event. This is most apparent for Mo, as the very low authigenic enrichments in the lower N-CIE interval are likely lagging relative to the new riverine Mo input. Still, the results of the mass balance models led to the conclusion that the T-OAE was a period of expanded anoxic/euxinic seafloor area, at least in part. The maximum 6% total seafloor area covered by anoxia/euxinia was most likely located along the continental margins, thus oceanic deep waters likely remained oxygenated.

Finally, an attempt to link the expansion of anoxic and euxinic seafloor areas to Karoo–Ferrar large igneous province activity was made using a sedimentary Hg proxy. No significant trends or peak were observed using the typical Hg/C_{org} normalisation (e.g. Them II, et al., 2019), and an attempted Hg/S_{TOT} normalisation was also inconclusive. A previous study indicated that the utility of the proxy may decrease with increasingly distal (deeper waters, farther offshore) marine deposition (Them II, et al., 2019). The study core is located more distally than the “distal” cores of the Them II, et al. (2019) study, which may be the reason why a clear trend was not observed.

The findings of this study have demonstrated that while the T-OAE was a minor anoxic expansion (maximum ~6% total seafloor area) relative to the well-known “Big 5” mass extinctions (e.g. Permian–Triassic: 70-95% species loss and anoxia expanded across ~20% of the seafloor; Lau, et al., 2016), it still produced a minor mass extinction. Continuing to study

oceanic anoxia during past OAEs may help put modern climate changes into context. Future study should include monitoring changes to the modern areal extents of seafloor anoxia and euxinia to compare to anoxic/euxinic expansions during mass extinctions associated with LIP-driven OAE events (Clapham & Renne, 2019; Bond & Wignall, 2014).

References

ActLabs. (2019). *Carbon/Sulphur/Nitrogen Species*. Retrieved from ActLabs.com: http://www.actlabs.com/page.aspx?menu=74&app=244&cat1=600&tp=2&lk=no

Algeo, T. J., & Lyons, T. W. (2006). Mo–total organic carbon covariation in modern anoxic marine environments: Implications for analysis of paleoredox and paleohydrographic conditions. *Paleoceanography*, 21, PA1016, 23p.

Algeo, T. J., & Rowe, H. (2012). Paleoceanographic applications of trace-metal concentration data. *Chemical Geology*, 324-325, 6-18.

Algeo, T. J., & Tribovillard, N. (2009). Environmental analysis of paleoceanographic systems based on molybdenum-uranium covariation. *Chemical Geology*, 268, 211-225.

Al-Suwaidi, A. H., Angelozzi, G. N., Baudin, F., Damborenea, S. E., Hesselbo, S. P., Jenkyns, H. C., . . . Riccardi, A. C. (2010). First record of the Early Toarcian Oceanic Anoxic Event from the Southern Hemisphere, Neuquen Basin, Argentina. *Journal of the Goelogical Society*, 167(4), 633-636.

Amante, C., & Eakins, B. W. (2009). ETOPO1 1 arc-minute global relief model: procedures, data sources and analysis. NOAA Technical Memorandum NESDIS NGDC-24. Boulder, CO.

Anbar, A. D., Creaser, R. A., Papanstassiou, D. A., & Wasserburg, G. J. (1992). Rhenium in seawater: Confirmation of generally conservative behaviour. *Geochimica et Cosmochimica Acta*, 56(11), 4099-4103.

Arthur, M. A., & Sageman, B. B. (1994). Marine Black Shales: Depositional mechanisms and environments of ancient deposits. *Annual Reviews in Earth and Planetary Sciences*, 22, 499-551.

Asgar-Deen, M., Hall, R., Craig, J., & Riediger, C. (2003). New biostratigraphic data from the Lower Jurassic Fernie Formation in the subsurface of west-central Alberta and their stratigraphic implications. *Canadian Journal of Earth Science*, 40, 45-63.

Asgar-Deen, M., Riediger, C., & Hall, R. (2004). The Gordondale Member: designation of a new member in the Fernie Formation to replace the informal "Nordegg Member"

nomeclature of the subsurface of west-central Alberta. *Bulletin of Canadian Petroleum Geology*, 52(3), 201-214.

Bacon, K. L., & Swindles, G. T. (2016). Could a potential Anthropocene mass extinction define a new geological period? *The Anthropocene Review*, 3(3), 208-217.

Beldowski, J., & Pempkowiak, J. (2009). Mercury concentration and solid phase speciation changes in the course of early diagenesis in marine coastal sediments (Southern Baltic Sea). *Marine and Freshwater Research*, 60, 745-757.

Benoit, J. M., Gilmour, C. C., Mason, R. P., & Heyes, A. (1999). Sulfide controls on mercury speciation and bioavailability to methylating bacteria in sediment pore waters. *Environmental Science and Technology*, 33, 951-957.

Bertine, K. K., & Turekian, K. K. (1973). Molybdenum in marine deposits. *Geochimica et Cosmochimica Acta*, 37, 1415-1434.

Boggs, S. (2006). *Principles of Sedimentology and Stratgraphy, Fourth Ed.* Upper Saddle River, NJ: Pearson Prentice Hall.

Bond, D. P., & Wignall, P. B. (2014). Large Igneous Provinces and mass exctintions: An update. In G. Keller, & A. C. Kerr, *Volcanism, Impacts, and Mass Extinctions: Causes and Effects* (pp. 29-55). Geological Society of America Special Paper 505.

Boulila, S., Galbrun, B., Huret, E., Hinnov, L. A., Rouget, I., Gardin, S., & Bartolini, A. (2014). Astronomical calibration of the Toarcian Stage: Implications for sequence stratigraphy and duration of the early Toarcian OAE. *Earth and Planetary Science Letters*, 386, 98-111.

Boutton, T. W. (1991). Stable Carbon Isotope Ratios of Natural Materials: II. Atmospheric, Terrestrial, Marine, and Freshwater Environments. In D. C. Coleman, & B. Fry, *Carbon Isotope Techniques* (p. 273). San Diego, CA: Academic Press, Inc.

Boyle, E. A. (1992). Cadmium and δ13C paleochemical ocean distributions during the Stage 2 Glacial Maximum. *Annual Review of Earth and Planetary Sciences*, 20, 245-287.

Brazier, J.-M., Suan, G., Tacail, T., Simon, L., Martin, J. E., Mattioli, E., & Balter, V. (2015). Calcium isotope evidence for dramatic increase of continental weathering during the

Toarcian oceanic anoxic event (Early Jurassic). *Earth and Planetary Science Letters*, 411, 164-176.

Breitburg, D., Levin, L. A., Oschlies, A., Grégoire, M., Chavez, F. P., Conley, D. J., . . . Zhang, J. (2018). Declining oxygen in the global ocean and coastal waters. *Science*, 359(6371), 11p.

Broecker, W. S., & Peng, T.-H. (1982). *Tracers in the Sea.* Palisades, NY: Columbia University Lamont-Doherty Geological Observatory.

Brown, S. T., Basu, A., Ding, X., Christensen, J. N., & DePaolo, D. J. (2018). Uranium isotope fractionation by abiotic reductive precipitation. *Proceedings of the National Academy of Sciences of the United States of America*, 115, 8688-8693.

Brumsack, H.-J. (1986). The inorganic geochemistry of Cretaceous black shales (DSDP Leg 41) in comparison to modern upwelling sediments from the Gulf of California. *Geological Society of London*, Special Publication 21(1), 447-462.

Bryan, S. E., Ukstins Peate, I., Peate, D. W., Self, S., Jerram, D. A., Mawby, M. R., . . . Miller, J. A. (2010). The largest volcanic eruptions on Earth. *Earth-Science Reviews*, 102(3-4), 207-229.

Burgess, S. D., Bowring, S. A., Fleming, T. H., & Elliott, D. H. (2015). High-precision geochronology links the Ferrar large igneous province with early-Jurassic ocean anoxia and biotic crisis. *Earth and Planetary Science Letters*, 415, 90-99.

Burton, K. W., Bourdon, B., Birck, J.-L., Allegre, C. J., & Hein, J. R. (1991). Osmium isotope variations in the oceans recorded by Fe-Mn crusts. *Earth and Planetary Science Letters*, 171, 185-197.

Calvert, S. E., & Pedersen, T. F. (1993). Geochemistry of Recent oxic and anoxic marine sediments: Implications for the geological record. *Marine Geology*, 113, 67-88.

Calvert, S. E., & Pedersen, T. F. (1996). Sedimentary geochemistry of manganese: Implications for the environment of formation of manganiferous black shales. *Economic Geology*, 36-47.

Canfield, D. E. (1998). A new model for Proterozoic ocean chemistry. *Nature*, 396, 450-453.

Canfield, D. E., Lyons, T. W., & Raiswell, R. (1996). A model for iron deposition to euxinic Black Sea sediments. *American Journal of Science*, 296, 818-834.

Canfield, D. E., Poulton, S. W., Knoll, A. H., Narbonne, G. M., Ross, G., Goldberg, T., & Strauss, H. (2015). Ferruginous conditions dominated Later Neoproterozoic deep-water chemistry. *Science*, 321(5891), 949-952.

Caruthers, A. H., Gröcke, D. R., & Smith, P. L. (2011). The significance of an Early Jurassic (Toarcian) carbon-isotope excursion in Haida Gwaii (Queen Charlotte Islands), British Columbia, Canada. *Earth and Planetary Science Letters*, 307(1-2), 19-26.

Ceballos, G., Ehrlich, P. R., Barnosky, A. D., Garcia, A., Pringle, R. M., & Palmer, T. M. (2015). Accelerated modern human-induced species losses: Entering the sixth mass extinction. *Science Advances*, 1(5), 5p.

Cecca, F., Fourcade, E., & Azema, J. (1992). The disappearance of the "Ammonitico Rosso" . *Palaeoceanography, Palaeoclimatology, Palaeoecology*, 99, 55-70.

Clarkson, M. O., Poulton, S. W., & Wood, R. A. (2014). Assessing the utility of Fe/Al and Fe-speciation to record water column redox conditions in carbonate-rich sediments. *Chemical Geology*, 382, 111-122.

Cohen, A. S., Coe, A. L., Harding, S. M., & Schwark, L. (2004). Osmium isotope evidence for the regulation of atmospheric CO2 by continental weathering. *Geology*, 32, 157-160.

Collier, R. W. (1984). Particulate and dissolved vanadium in the North Pacific Ocean. *Nature*, 309, 441-444.

Collier, R. W. (1985). Molybdenum in the Northeast Pacific Ocean. *Limnology and Oceanography*, 30(6), 1351-1354.

Colodner, D., Sachs, J., Ravizza, G., Turekian, K., Edmond, J., & Boyle, E. (1993). The geochemical cycle of rhenium: A reconnaissance. *Earth and Planetary Science Letters*, 117, 205-221.

Creaney, S., & Allan, J. (1990). Hydrocarbon generation and migration in the Western Canada sedimentary basin. In J. Brooks, *Classic Petroleum Provinces* (pp. 189-202). Calgary, AB: Geological Society Special Publication.

Creaser, R. A., Sannigrahi, P., Chacko, T., & Selby, D. (2002). Further evaluation of the Re-Os geochronometer in organic-rich sedimentary rocks: a test of hydrocarbon maturation effects in the Exshaw Formation, Western Canada Sedimentary Basin. *Geochimica et Cosmochimica Acta*, 66(19), 3441-3452.

Crusius, J., Calvert, S., Pedersen, T., & Sage, D. (1996). Rhenium and molybdenum enrichments in sediments as indicators of oxic, suboxic and sulfidic conditions of deposition. *Earth and Planetary Science Letters*, 145, 65-78.

Dean, W. E., & Arthur, M. A. (1989). Iron-sulfur-carbon relationships in organic-carbon-rich sequences I: Cretaceous Western Interior Seaway. *American Journal of Science*, 289, 708-743.

Dellisanti, F., Pini, G. A., & Baudin, F. (2010). Use of Tmax as a thermal maturity indicator in orogenic successions and comparison with clay mineral evolution. *Clay Minerals*, 45(1), 115-130.

Dera, G., & Donnadieu, Y. (2012). Modeling evidences for global warming, Arctic seawater freshening, and sluggish oceanic circulation during the Early Toarcian anoxic event. *Paleoceanography and Paleoclimatology*, 27(2), 15p.

Dickson, A. J., Idiz, E., Porcelli, D., & van den Boorn, S. H. (2019). The influence of thermal maturity on the stable isotope compositions and concentrations of molybdenum, zinc and cadmium in organic-rich marine mudrocks. *Geochimica et Cosmochimica Acta*, in Press.

Drake, C. L., & Burk, C. A. (1974). Geological Significance of Continental Margins. In C. A. Burk, & C. L. Drake, *The Geology of Continental Margins* (pp. 3-10). New York, NY: Springer-Verlag.

Driscoll, C. T., Mason, R. P., Chan, H. M., Jacob, D. J., & Pirrone, N. (2013). Mercury as a Global Pollutant: Sources, Pathways, and Effects. *Environmnetal Science and Technology*, 47(10), 4967-4983.

Eltra. (2019). *Elementrac CS-d Carbon/Sulfur Analyzer*. Retrieved from Eltra Element Analyzers: https://www.eltra.com/products/chs-analyzers/cs-d/function-features

Emerson, S. R., & Huested, S. S. (1991). Ocean anoxia and the concentrations of molybdenum and vanadium in seawater. *Marine Chemistry*, 34, 177-196.

Erickson, B. E., & Helz, G. R. (2000). Molybdenum(VI) speciation in sulfidic waters: Stability and lability of thiomolydates. *Geochimica et Cosmochimica Acta*, 64(7), 1149-1158.

Eyles, N., & Miall, A. (2007). *Canada Rocks: The Geologic Journey.* Markham, ON: Fitzhenry and Whiteside.

Fantasia, A., Follmi, K. B., Adatte, T., Bernardez, E., Spangenberg, J. E., & Mattioli, E. (2018). The Toarcian Oceanic Anoxic Event in southwestern Gondwana: an example from the Andean Basin, northern Chile. *Journal of the Geological Society*, 175, 883-902.

Faure, G. (1991). *Principles and Applications of Inorganic Geochemistry.* New York, NY: Macmillan Publishing Company.

Fitzgerald, W. F., & Lamborg, C. H. (2005). Geochemistry of Mercury in the Environment. In H. D. Holland, B. Sherwood Lollar, & K. K. Turekian, *Environmental Geochemistry: Treatise on Geochemistry Vol. 9* (pp. 107-148). Oxford, UK: Elsevier.

Follmi, K. B. (1996). The phosphorus cycle, phosphogenesis and marine phosphate-rich deposits. *Earth Science Reviews*, 40, 55-124.

Frebold, H. (1969). Subdivision and facies of Lower Jurassic rocks in the southern Canadian rocky mountains and foothills. *Proceedings of the Geological Association of Canada*, 20, 76-89.

Fuex, A. N. (1977). The use of stable carbon isotopes in hydrocarbon exploration. *Journal of Geochemical Exploration*, 7, 155-188.

Grasby, S. E., Them II, T. R., Chen, Z., Yin, R., & Ardakani, O. H. (2019). Mercury as a proxy for volcanic emissions in the geological record. *Earth-Science Reviews*, 196, 16p.

Gröcke, D. R., Hori, R. S., Trabucho-Alexandre, J., Kemp, D. B., & Schwark, L. (2011). An open ocean record of the Toarcian oceanic anoxic event. *Solid Earth*, 2, 245-257.

Hall, R. L., Kendall, D. R., Taylor, D. G., & Craig, J. (2000). A new ammonite and coccolith fauna from the lowermost Fernie Formation (Hettangian) in northwestern Alberta. *Canadian Journal of Earth Sciences*, 37, 1373-1376.

Hall, R., & Pitaru, S. (2004). New Hettangian ammonite faunas and a Triassic-Jurassic boundary succession, Fernie Formation, Williston Lake, British Columbia. *Rivista Italiana di Paleontologia e Stratigrafia*, 110(1), 53-60.

Hall, R., McNicoll, V., Grocke, D., Craig, J., & Johnston, K. (2004). Integrated stratigraphy of the Lower and Middle Fernie Formation in Alberta and British Columbia, Western Canada. *Rivista Italiana di Paleontologia e Stratigrafia*, 110(1), 62-68.

Hardisty, D. S., Lyons, T. W., Riedinger, N., Isson, T. T., Owens, J. D., Aller, R. C., . . . Johnston, D. T. (2018). An evaluation of sedimentary molybdenum and iron as proxies for pore fluid paleoredox conditions. *American Journal of Science*, 318, 527-556.

Helz, G. R., & Dolor, M. K. (2012). What regulates rhenium deposition in euxinic basins? *Chemical Geology*, 304/305, 131-141.

Helz, G. R., Bura-Nakić, E., Mikac, N., & Ciglenečki, I. (2011). New model for molybdenum behaviour in euxinic waters. *Chemical Geology*, 284(3-4), 323-332.

Henderson, R. A. (2004). A Mid-Cretaceous Association of Shell Beds and Organic-rich Shale: Bivalve Exploitation of a Nutrient-rich, Anoxic Sea-floor Environment. *Palaios*, 19(2), 156-169.

Hesselbo, S. P., Gröcke, D. R., Jenkyns, H. C., Bjerrum, C. J., Farrimond, P., Morgans Bell, H. S., & Green, O. R. (2000). Massive dissociation of gas hydrate during a Jurassic oceanic anoxic event. *Nature*, 406, 392-395.

Hesselbo, S. P., Jenkyns, H. C., Duarte, L. V., & Oliveira, L. C. (2007). Carbon-isotope record of the Early Jurassic (Toarcian) Oceanic Anoxic Event from fossil wood and marine carbonate (Lusitanian Basin, Portugal). *Earth and Planetary Science Letters*, 253(3-4), 455-470.

Higgins, J. A., & Schrag, D. P. (2006). Beyond methane: towards a theory for the Paleocene-Eocene Thermal Maximum. *Earth and Planetary Science Letters*, 245, 523-537.

Homewood, P. (1982). Palaeogeography of alpine flysch. *Palaeogeography, Palaeoclimatology, Palaeoecology*, 44(3-4), 169-184.

Homewood, P., & Lateltin, O. (1988). Classic swiss clastics (flysch and molasse): The alpine connection. *Geodinamica Acta*, 2(1), 1-11.

Ibrahimbas, A., & Riediger, C. (2004). Hydrocarbon source rock potential as determined by Rock-Eval 6/TOC pyrolysis, northeastern British Columbia and northwest Alberta. *Resource Development and Geoscience Branch, Summary of Activities*, 7-18.

International Union of Pure and Applied Chemistry (IUPAC). (2018, December 1). *IUPAC Periodic Table of the Elements.* Retrieved from iupac.org: https://iupac.org/wp-content/uploads/2018/12/IUPAC_Periodic_Table-01Dec18.jpg

Jahren, A. H., Arens, N. C., Sarmiento, G., Guerrero, J., & Amundson, R. (2001). Terrestrial record of methane hydrate dissociation in the Early Cretaceous. *Geology*, 29(2), 159-162.

Jenkyns, H. C. (1988). The Early Toarcian (Jurassic) anoxic event: stratigraphic, sedimentary, and geochemical evidence. *American Journal of Science*, 288, 101-151.

Jenkyns, H. C. (2010). Geochemistry of oceanic anoxic events. *Geochemistry, Geophysics, Geosystems*, 11(3), 30p.

Jenkyns, H. C., & Clayton, C. J. (1986). Black shales and carbon isotopes in pelagic sediments from the Tethyan Lower Jurassic. *Sedimentology*, 33, 87-106.

Jones, C. E., & Jenkyns, H. C. (2001). Seawater strontium isotopes, ocean anoxic events and seafloor hydrothermal activity in the Jurassic and Cretaceous. *American Journal of Science*, 301, 112–149.

Keller, G., Mateo, P., Punekar, J., Khozyem, H., Gertsch, B., Spangenberg, J., . . . Adatte, T. (2018). Environmental changes during the Cretaceous-Paleogene mass extinction and Paleocene-Eocene Thermal Maximum: Implications for the Anthropocene. *Gondwana Research*, 56, 69-89.

Kemp, D. B., Coe, A. L., Cohen, A. S., & Schwark, L. (2005). Astronomical pacing of methan release in the Early Jurassic period. *Nature*, 437, 396-399.

Kendall, B., Dahl, T. W., & Anbar, A. D. (2017). Good Golly, Why Moly? The Stable Isotope Geochemistry of Molybdenum. *Reviews in Mineralogy and Geochemistry*, 82, 683-732.

Klinkhammer, G. P., & Palmer, M. R. (1991). Uranium in the oceans: Where it goes and why. *Geochimica et Cosmochimica Acta*, 55, 1799-1806.

Kondla, D., Sanei, H., Clarkson, C. R., & Goodarzi, F. (2017). High resolution characterization of a core from the Lower Jurassic Gordondale Member, Western Canada Sedimentary Basin. *Marine and Petroleum Geology*, 83, 50-59.

Kunert, A., Kendall, B., Moslow, T. F., Nyberg, G., Pedersen, B., & Smith, C. (2019). Preliminary Characterization of Early Jurassic Source Rocks and Ocean-Redox Conditions Based on Trace-Metal and Organic Geochemistry of the Gordondale and Poker Chip Shale Members, Fernie Formation, Northeastern British Columbia. *Geoscience BC Summary of Activities 2018: Energy and Water, Geoscience BC Report 2019-2*, 29-42.

Kuroda, J., Ogawa, N. O., Tanimizu, M., Coffin, M. F., Tokuyama, H., Kitazato, H., & Ohkouchi, N. (2007). Contemporaneous massive subaerial volcanism and Late Cretaceous Oceanic Anoxic Event 2. *Earth and Planetary Science Letters*, 256, 211-223.

Kuspert, W. (1982). Environmental changes during oil shale deposition as deduced from stable isotope ratios. In G. Einsele, & A. Seilacher, *Cyclic and Event Stratification* (pp. 482-501). Heidelburg, Germany: Springer.

LaGrange, M. T., Brette, S. H., & Gingras, M. K. (2019). Building a Sequence Stratigraphic Framework using Chemostratigraphy: An Example from the Devonian Canol Formation, Northwest Territories. *GeoConvention.* Calgary, AB.

Lau, K. V., Maher, K., Altiner, D., Kelley, B. M., Kump, L. R., Lehrmann, D. J., . . . Payne, J. L. (2016). Marine anoxia and delayed Earth system recovery after the end-Permain extinction. *Proceedings of the National Academy of Sciences of the United States of America*, 113(9), 2360-2365.

Lenton, T. M., Daines, S. J., & Mills, B. J. (2018). COPSE reloaded: An improved model of biogeochemical cycling over Phanerozoic time. *Earth-Science Reviews*, 178, 1-28.

Lindqvist, O., & Rodhe, H. (1985). Atmopsheric mercury - a review. *Tellus B: Chemical and Physical Meteorology*, 37(3), 136-156.

Lyons, T. W., & Severmann, S. (2006). A critical look at iron paleoredox proxies: New insights from modern euxinic marine basins. *Geochimica et Cosmochimica Acta*, 70, 5698-5722.

Martin, J.-M., & Meybeck, M. (1979). Elemental mass-balance of material carried by major world rivers. *Marine Chemistry*, 7(3), 173-206.

Mason, R. P., Fitzgerald, W. F., & Morel, F. M. (1994). The biogeochemical cycling of elemental mercury: Anthropgoenic influences. *Geochimica et Cosmochimica Acta*, 58(15), 3191-3198.

McArthur, J. M. (2019). Early Toarcian black shales: A response to an oceanic anoxic event or anoxia in marginal basins? *Chemical Geology*, 522, 71-83.

McArthur, J. M., Donovan, D. T., Thirlwall, M. F., Fouke, B. W., & Mattey, D. (2000). Strontium isotope profile of the Early Toarcian (Jurassic) oceanic anoxic event, the duration of ammonite biozones, and belemnite palaeotemperatures. *Earth and Planetary Science Letters*, 179, 269-285.

McElwain, J. C., Wade-Murphy, J., & Hesselbo, S. P. (2005). Changes in carbon dioxide during an oceanic anoxic event linked to intrusion into Gondwana coals. *Nature*, 435, 479-482.

McKay, J. L., & Pedersen, T. F. (2014). Geochemical response to pulsed sedimentation: Implications for the use of Mo as a paleo-proxy. *Chemical Geology*, 382, 83-94.

McLennan, S. M. (2001). Relationship between the trace element composition of sedimentary rocks and upper continental crust. *Geochemistry, Geophysics, Geosystems*, 2, 24p.

McManus, J., Berelson, W. M., Klinkhammer, G. P., Hammond, D. E., & Holm, C. (2005). Authigenic uranium: relationship to oxygen penetration depth and organic carbon rain. *Geochimica et Cosmochimica Acta*, 69, 95-108.

Meyer, K. M., & Kump, L. R. (2008). Oceanic Euxinia in Earth History: Causes and Consequences. *Annual Reviews in Earth and Planetary Sciences*, 36, 251-288.

Miller, C. A., Peucker-Ehrenbrink, B., Walker, B. D., & Marcantonio, F. (2011). Re-assessing the surface cycling of molybdenum and rhenium. *Geochimica et Cosmochimica Acta*, 75, 7146-7179.

Mishra, B., Shoenfelt, E., Yu, Q., Yee, N., Fein, J. B., & Myneni, S. C. (2017). Stoichiometry of mercury-thiol complexes on bacterial cell envelopes. *Chemical Geology*, 137-146.

Moslow, T. F. (2016, October 20). Clastic Core Logging Form: c-B006-A/94-B-8. *Unpublished*. Calgary, AB: Petronas Canada.

Ostrander, C. M., Sahoo, S. K., Kendall, B., Jiang, G., Planavsky, N. J., Lyons, T. W., . . . Anbar, A. D. (2019). Multiple negative molybdenum isotope excursions in the Doushantuo Formation (South China) fingerprint compex redox-related processes in the Ediacaran Nanhua Basin. *Geochimica et Cosmochimica Acta*, 261, 191-209.

Owens, J. D., Lyons, T. W., & Lowery, C. M. (2018). Quantifying the missing sink for global organic carbon burial during a Cretaceous oceanic anoxic event. *Earth and Planetary Science Letters*, 499, 83-94.

Pálfy, J., & Smith, P. L. (2000). Synchrony between Early Jurassic extinction, oceanic anoxic event, and the Karoo-Ferrar flood basalt volcanism. *Geology*, 28(8), 747-750.

Pană, D. I., Creaser, R. A., Toma, J., Playter, T. L., Corlett, H. J., Hauck, T. E., . . . Poulton, T. (2018a). *Geochronology in Support of the Alberta Table of Formations: Rhenium-Osmium Isotope Dating of Selected Devonian and Jurassic Core Samples from Central and Northern Alberta.* Open File Report 2018-06, Edmonton, AB: Alberta Energy Regulator/Alberta Geological Survey.

Pană, D. I., Poulton, T. P., & DuFrane, A. (2017). *U-Pb Detrital Zircon Geochronology of the Jurassic Through Lower Cretaceous Strata of the Rocky Mountains, Southwestern Alberta.* Open File Report 2017-01, Edmonton, AB: Alberta Energy Regulator/Alberta Geological Survey.

Pană, D. I., Poulton, T. P., & Heaman, L. M. (2018b). U-Pb zircon ages of volcanic ashes integrated with ammonite biostratigraphy, Fernie Formation (Jurassic), Western Canada, with implications for Cordilleran-Foreland basin connection snd comments on the Jurassic time scale. *Bulletin of Canadian Petroeum Geology*, 66(3), 595-622.

Paquette, K., & Helz, G. (1995). Solubility of cinnabar (red HgS) and implications for mercury speciation in sulfidic waters. *Water, Air and Soil Pollution*, 80, 1053-1056.

Partin, C. A., Bekker, A., Planavsky, N. J., Scott, C. T., Gill, B. C., Li, C., . . . Lyons, T. W. (2013). Large-scale fluctuations in Precambrian atmospheric and oceanic oxygen levels from the record of U in shales. *Earth and Planetary Science Letters*, 360-370, 284-293.

Pearce, C. R., Cohen, A. S., Coe, A. L., & Burton, K. W. (2008). Molybdenum isotope evidence for global ocean anoxia coupled with perturbations to the carbon cycle during the Early Jurassic. *Geology*, 36(3), 231-234.

Percival, L. M., Cohen, A. S., Davies, M. K., Dickson, A. J., Hesselbo, S. P., Jenkyns, H. C., . . . Xu, W. (2016). Osmium isotope evidence for two pulses of increased continental weathering linked to Early Jurassic volcanism and climate change. *Geology*, 44(9), 759-762.

Percival, L. M., Witt, M. L., Mather, T. A., Hermoso, M., Jenkyns, H. C., Hesselbo, S. P., . . . Ruhl, M. (2015). Globally enhanced mercury deposition during the end-Pliensbachian extinction and Toarcian OAE: A link to the Karoo-Ferrar Large Igneous Province. *Earth and Planetary Science Letters*, 428, 267-280.

Peters, K. E., Walters, C. C., & Moldowan, J. M. (2005). *The biomarker guide, Vol. 1.* Cambridge, UK: Cambridge University Press.

Pogge con Strandmann, P. A., Jenkyns, H. C., & Woodfine, R. G. (2013). Lithium isotope evidence for enhanced weathering during Oceanic Anoxic Event 2. *Nature Geoscience*, 6, 668-672.

Poulton, S. W., & Canfield, D. E. (2011). Ferruginous Conditions: A Dominant Feature of the Ocean through Earth's History. *Elements*, 7, 107-112.

Poulton, T. P. (1991). Upper Devonian to Middle Jurassic assemblages Part A: Ancestral North America: Lower and Middle Jurassic strata of the Foreland Belt. In H. Gabrielse, & C. J. Yorath, *Geology of the Cordilleran Orogen in Canada, Geology of Canada Series no. 4* (pp. 276-281). Geological Survey of Canada.

Poulton, T. P., Christopher, J. E., Hayes, B. J., Losert, J., Tittemore, J., Gilchrist, R. D., . . . McCabe, H. R. (1994). Chapter 18 - Jurassic and Lowermost Cretaceous Strata of the

Western Canada Sedimentary Basin. In G. Mossop, & I. Shetsen, *Atlas of the Western Canada Sedimentary Basin* (pp. 297-316). Calgary, AB: Canadian Society of Petroleum Geologists.

Poulton, T. P., Tittemore, J., & Dolby, G. (1990). Jurassic strata of northwestern (and west-central) Alberta and northeastern British Columbia. *Bulletin of Canadian Petroleum Geology*, 38A, 159-175.

Price, R. A. (1994). Chapter 2 - Cordilleran Tectonics and the Evolution of the Western Canada Sedimentary Basin. In G. Mossop, & I. Shetsen, *Atlas of the Western Canada Sedimentary Basin* (pp. 13-24). Calgary, AB: Canadian Society of Petroleum Geologists.

Prokoph, A., Ernst, R. E., & Buchan, K. L. (2004). Time-series analysis of Large Igneous Provinces: 3500 Ma to Present. *The Journal of Geology*, 112(1), 1-22.

Pyle, D. M., & Mather, T. A. (2003). The importance of volcanic emissions for the global atmospheric mercury cycle. *Atmospheric Environment*, 37(36), 5115-5124.

Quinby-Hunt, M. S., & Wilde, P. (1994). Thermodynamic zonation in the black shale fcies based on iron-manganese-vanadium content. *Chemical Geology*, 113, 297-317.

Raiswell, R., & Canfield, D. E. (1996). Rates of reaction between silicate iron and dissolved sulfide in Peru Margin sediments. *Geochimica et Cosmochimica Acta*, 60(15), 2777-2787.

Redfield, A. C. (1934). On the proportions of organic derivatives in sea water and their relationship to the composition of plankton. *James Johnstone Memorial Volume, University of Liverpool*, 176-192.

Reinhard, C. T., Planavsky, N. J., Robbins, L. J., Partin, C. A., Gill, B. C., Lalonde, S. V., . . . Lyons, T. W. (2013). Proterzoic ocean redox and biogeochemical stasis. *Proceedings of the National Academy of Sciences of the United States*, 110(14), 5357-5362.

Retallack, G. J., & Jahren, A. H. (2008). Methane release from igneous intrusion of coal during Late Permian extinction events. *Journal of Geology*, 116, 1-20.

Riediger, C. L. (1990). *Rock-Eval/TOC data from the Lower Jurassic "Nordegg Member", and the Lower and Middle Triassic Doig and Montney formations, Western Canada Sedimentary Basin, Alberta and British Columbia.* Calgary, AB: Geological Survey of Canada, Open File, Report No. 2308.

Riediger, C. L. (1991). *Lower Mesozoic hydrocarbon source rocks, Western Canada Sedimentary Basin.* Waterloo, ON: University of Waterloo [Unpublished PhD Dissertation].

Riediger, C. L. (1994). Migration of "Nordegg" oil in the Western Canada Basin. How much and how far? *Bulletin of Canadian Petroleum Geology*, 42(1), 63-73.

Riediger, C. L. (2002). Hydrocarbon source rock potential and comments on correlation of the Lower Jurassic Poker Chip Shale, west-central Alberta. *Bulletin of Canadian Petroleum Geology*, 50(2), 263-276.

Riediger, C. L., & Bloch, J. D. (1995). Depositional and diagenetic controls on source-rock charateristics of the Lower Jurassic "Nordegg Member", Western Canada. *Journal of Sedimentary Research*, A65(1), 112-126.

Riediger, C. L., & Coniglio, M. (1992). Early diagenetic calcites and associated bitumens in the "Nordegg Member": implications for Jurassic paleogeography of the Western Canada Sedimentary Basin. *Bulletin of Canadian Petroleum Geology*, 40(4), 381-394.

Rio Segade, S., Dias, T., & Ramalhosa, E. (2010). Mercury methylation versus demethylation: Main processes involved. In A. P. Clampet, *Methylmercury: Formation, Sources and Health Effects* (p. 32p.). New York, NY: Nova Science Publishers.

Rogers, J. J., & Santosh, M. (2004). *Continents and Supercontinents.* New York, NY: Oxford University Press.

Rooney, A. D., Selby, D., Lloyd, J. M., Roberts, D. H., Luckge, A., Sageman, B. B., & Prouty, N. G. (2016). Tracking millenial-scale Holocene glacial advance and retreat using osmium isotopes: Insights from the Greenland ice sheet. *Quaternary Science Reviews*, 138, 49-61.

Ross, D. J. (2004). *Sedimentology, geochemistry and gas shale potential of the Early Jurassic Nordegg Member, northeastern British Columbia.* Vancouver, BC: The University of British Columbia [MSc Thesis].

Ross, D. J., & Bustin, R. M. (2006). Sediment geochemistry of the Lower Jurassic Gordondale Member, northeastern British Columbia. *Bulletin of Canadian Petroleum Geology*, 54(4), 337-365.

Ross, D. J., & Bustin, R. M. (2007). Shale gas potential of the Lower Jurassic Gordondale Member, northeastern British Columbia, Canada. *Bulletin of Canadian Petroleum Geology*, 55(1), 51-75.

Ross, D. K. (n.d.).

Ruban, D. A. (2015). Mesozoic long-term eustatic cycles and their uncertain hierarchy. *Geoscience Frontiers*, 6(4), 503-511.

Sageman, B. (2009). Ocean Anoxic Events. In V. Gornitz, *Encyclopedia of Paleoclimatology and Ancient Environments. Encyclopedia of Earth Sciences Series* (pp. 625-628). Dordrecht: Springer.

Sanei, H., Grasby, S. E., & Beauchamp, B. (2012). Latest Permian mercury anomalies. *Geology*, 40(1), 63-66.

Schlanger, S. O., & Jenkyns, H. C. (1976). Cretaceous Oceanic Anoxic Events: Causes and Consequences. *Geologie en Mijnbouw*, 55(3-4), 179-184.

Scholz, F., Siebert, C., Dale, A. W., & Frank, M. (2017). Intense molybdenum accumulation in sediments underneath a nitrogenous water column and implications for the reconstruction of paleo-redox conditions based on molybdenum isotopes. *Geochimica et Cosmochimica Acta*, 213, 400-417.

Schouten, S., Van Kaam-Peters, H. M., Rijpstra, W. I., Schoell, M., & Sinninghe Damste, J. S. (2000). Effects of an oceanic anoxic event on the stable carbon isotopic composition of Early Toarcian carbon. *American Journal of Science*, 300, 1-22.

Scotese, C. (2013). Map Folio 39 Early Jurassic Toarcian, 179.3 Ma. *PALEOMAP PaleoAtlas for ArcGIS, Vol. 3: Triassic and Jurassic Paleogeographic, Paleoclimatic and Plate Tectonic Reconstructions*. Evanston, IL: PALEOMAP Project.

Scott, C., & Lyons, T. W. (2012). Contrasting molybdenum cycling and isotopic properties in euxinic verusus non-euxinic sediments and sedimentary rocks: Refining the paleoproxies. *Chemical Geology*, 324-325, 19-27.

Scott, C., Slack, J. F., & Kelley, K. D. (2017). The hyper-enrichment of V and Zn in black shales of the Late Devonian-Early Mississippian Bakken Formation (USA). *Chemical Geology*, 452, 24-33.

Selby, D., & Creaser, R. A. (2003). Re-Os geochronology of organic rich sediments: an evaluation of organic matter analysis methods. *Chemical Geology*, 200, 225-240.

Selby, D., & Creaser, R. A. (2005). Direct radiometric dating of the Devonian-Mississippian time-scale boundary using the Re-Os geochronometer. *Geology*, 33(7), 545-548.

Sell, B., Ovtcharova, M., Guex, J., Bartolini, A., Jourdan, F., Spangenger, J. E., . . . Schaltegger, U. (2014). Evaluating the temporal link between the Karoo LIP and climatic-biologic events of the Toarcian Stage with high-precision U-Pb geochronology. *Earth and Planetary Science Letters*, 408, 48-56.

Sheen, A. I., Kendall, B., Reinhard, C. T., Creaser, R. A., Lyons, T. W., Bekker, A., . . . Anbar, A. D. (2018). A model for the oceanic mass balance of rhenium and implications for the extent of Proterozoic ocean anoxia. *Geochimica et Cosmochimica Acta*, 227, 75-95.

Song, H., Jiang, G., Poulton, S. W., Wignall, P. B., Tong, J., Song, H., . . . Wang, C. (2017). The onset of widespread marine red beds and the evolution of ferruginous oceans. *Nature Communications*, 8, article 399.

Spivak, J. (1949). Jurassic sections in foothills of Alberta and northeastern British Columbia. *Bulletin of the American Association of Petroleum Geologists*, 32, 533-546.

Stefani, V. (2017). *X-ray Diffraction Report on the c-B006-A/094-B-08.* Calgary, AB: Argile Analytica Inc.

Suan, G., Mattioli, E., Pittet, B., Mailliot, S., & Lecuyer, C. (2008). Evidence for major environmental perturbation prior to and during the Toarcian (Early Jurassic) oceanic anoxic event from the Lusitanian Basin, Portugal. *Paleoceanography*, 23(1), 14p.

Sweere, T., van den Boorn, S., Dickson, A. J., & Reichart, G.-J. (2016). Definition of new trace-metal proxies for the controls on organic matter enrichment in marine sediments based on Mn, Co, Mo and Cd concentrations. *Chemical Geology*, 441, 235-245.

Tagliabue, A., Mtshali, T., Aumont, O., Bowie, A. R., Klunder, M. B., Roychoudhury, A. N., & Swart, S. (2012). A global compilation of dissolved iron measurements: focus on distributions and processes in the Southern Ocean. *Biogeosciences*, 9, 2333-2349.

Them II, T. R. (2016). *Biogeochemical cycling and paleoenvironmental reconstructions of the Toarcian Oceanic Anoxic Event from western North America.* Blackburg, VA: Virginia Polytechnic Institute and State University [PhD Dissertation].

Them II, T. R., Gill, B. C., Caruthers, A. H., Gerhardt, A. M., Grocke, D. R., Lyons, T. W., . . . Owens, J. D. (2018). Thallium isotopes reveal protracted anoxia during the Toarcian (Early Jurassic) associated with volcanism, carbon burial, and mass extinction. *Proceedings of the National Academy of Science of the United States*, 115(26), 6596-6601.

Them II, T. R., Gill, B. C., Caruthers, A. H., Grocke, D. R., Tulsky, E. T., Martindale, R. C., . . . Smith, P. L. (2017a). High-resolution carbon isotope records of the Toarcian Oceanic Anoxic Event (Early Jurassic) from North America and implications for the global drivers of the Toarcian carbon cycle. *Earth and Planetary Science Letters*, 459, 118-126.

Them II, T. R., Gill, B. C., Selby, D., Grocke, D. R., Friedman, R. M., & Owens, J. D. (2017b). Evidence for rapid weathering response to climatic warming during the Toarcian Oceanic Anoxic Event. *Nature Scientific Reports*, 7, 10p.

Them II, T. R., Jagoe, C. H., Caruthers, A. H., Gill, B. C., Grasby, S. E., Grocke, D. R., . . . Owens, J. D. (2019). Terrestrial sources as the primary delivery mechanism of mercury to the oceans across the Toarcian Oceanic Anoxic Event (Early Jurassic). *Earth and Planetary Science Letters*, 507, 62-72.

Tribovillard, N., Algeo, T. J., Lyons, T., & Riboulleau, A. (2006). Trace metals as paleoredox and paleoproductivity proxies: An update. *Chemical Geology*, 232, 12-32.

Truesdale, G. A., & Downing, A. L. (1954). The solubility of oxygen in water. *Nature*, 173, 1236.

Turgeon, S., & Brumsack, H.-J. (2006). Anoxic vs dysoxic events reflected in sediment geochemistry during the Cenomanian–Turonian Boundary Event (Cretaceous) in the Umbria–Marche Basin of central Italy. *Chemical Geology*, 234, 321-339.

Tyson, R. V., & Pearson, T. H. (1991). Modern and ancient continental shelf anoxia: an overview. In R. V. Tyson, & T. H. Pearson, *Modern and Ancient Continental Shelf Anoxia, Geological Society Special Publication Volume 58* (pp. 1-26). London, UK: Geological Society London.

Ullmann, C. V., Thibault, N., Ruhl, M., Hesselbo, S. P., & Korte, C. (2014). Effect of a Jurassic oceanic anoxic event on belemnite ecology and evolution. *Proceedings of the National Academy of Sciences of the United States of America*, 111(28), 10073-10076.

van Andel, T. H. (1975). Mesozoic/Cenozoic calcite compensation depth and the global distribution of calcareous sediments. *Earth and Planetary Science Letters*, 26, 187-194.

van de Schootbrugge, B., McArthur, J. M., Bailey, T. R., Rodenthal, Y., Wright, J. D., & Miller, K. G. (2005). Toarcian oceanic anoxic event: An assessment of global causes using belemnite C isotope records. *Paleoceanography*, 20, 10p.

van Hindsbergen, D. J., de Groot, L. V., van Schaik, S. J., Spakman, W., Bijl, P. K., Sluijs, A., . . . Brinkhuis, H. (2015). A Paleolatitude calculator for paleoclimate studies. *PLoS ONE*, 10(6), 21p.

Wang, S. (2018). *Development of molybdenum isotopes as petroleum tracers: the Phosphoria petroleum system, Bighorn Basin, USA.* Waterloo, ON: University of Waterloo [MSc Thesis].

Watson, E. B., Cherniak, D. J., Hanchar, J. M., Harrison, T. M., & Wark, D. A. (1997). The incorporation of Pb into zircon. *Chemical Geology*, 141, 19-31.

Weatherford Laboratories Canada Ltd. (2017). *Petrophysics, Geochemistry, and Rock Mechanics Study, Well: Progress HZ Altares c-B006-A/094-B-08.* Calgary, AB: Weatherford.

Werner, R. A., & Brand, W. A. (2001). Referencing strategies and techniques in stable isotope ratio analysis. *Rapid Communications in Mass Spectrometry*, 15(7), 501-519.

West, J. B., Bowen, G. J., Cerling, T. E., & Ehlering, J. R. (2006). Stable isotopes as one of nature's ecological recorders. *Trends in Ecology and Evolution*, 21(7), 408-414.

Wignall, P. B., Sun, Y., Bond, D. P., Izon, G., Newton, R. J., Vedrine, S., . . . Bottrell, S. H. (2009). Volcanism, mass extinction, and carbon isotope fluctuations in the Middle Permian of China. *Science*, 324(5931), 1179-1182.

Wilson, J. L. (1975). *Carbonate Facies in Geologic History.* Berlin: Springer-Verlag.

Yang, S. (2019). *Reconstruction of local and global marine paleoredox conditions during deposition of the Devonian-Mississippian Exshaw Formation (Black Shale Member) and the Evaluation of hydrocarbon maturation effects.* Waterloo, ON. [MSc Thesis]: University of Waterloo.

Appendices

Appendix 1: Carbon Geochemistry and Pyrolysis Data

Depth (m)	C_{org} (wt%)	$\delta^{13}C$ (‰)	Tmax (°C)	Oxygen Index	Hydrogen Index
1560.06	2.59	-30.1			
1560.51				3	67
1561.36	3.47	-30.3			
1561.60			472	2	84
1561.91	3.94	-30.2			
1562.27	4.04	-30.3			
1562.40			476	2	90
1562.93	4.77	-30.1			
1563.32			478	4	54
1563.90	4.42	-29.9			
1564.28	6.06	-29.9			
1564.67			478	2	85
1565.46			477	3	87
1565.61	4.39	-29.7			
1566.37	4.38	-29.4			
1566.68			476	3	60
1567.47			469	4	101
1567.66	3.78	-28.7			
1568.01	4.18	-28.9			
1568.41			479	4	65
1568.60	3.84	-28.9			
1568.68	2.80	-28.6			
1569.47			478	4	74
1569.77	4.59	-28.4			
1570.15	3.75	-28.1			
1570.48			474	2	96
1570.76	5.07	-28.0			
1571.33	5.04	-28.1			
1571.66			473	2	93
1571.92	4.2	-28.3			
1572.31			475	2	104
1572.58	5.64	-28.5			
1573.31	5.27	-28.4	478	3	77
1574.17	4.43	-28.6			
1574.29			474	4	80
1574.53	3.99	-28.9			
1574.85	3.20	-29.7			
1575.00	9.18	-29.7			
1575.25	4.24	-29.6			

1575.35	4.51	-29.4			
1575.46	4.78	-29.5			
1575.50			479	5	70
1575.61	4.24	-29.6			
1575.82	4.57	-29.7			
1575.93	3.91	-29.7			
1576.11	5.60	-29.7			
1576.29			475	4	70
1576.37	4.76	-29.6			
1576.41	4.93	-29.7			
1576.59	5.03	-29.5			
1576.82	5.24	-29.6			
1576.91	6.31	-29.7			
1577.11	4.97	-29.4			
1577.24	5.14	-29.8			
1577.36	4.93	-29.6			
1577.61	4.63	-29.9			
1577.65			473	5	62
1577.84	4.31	-29.2			
1578.34	3.53	-29.9			
1578.50			471	20	24
1578.93	4.14	-29.8			
1579.06	4.15	-29.8			
1579.10	4.12	-29.8			
1579.32	5.35	-29.9			
1579.57			483	4	88
1579.61	3.79	-29.9			
1579.93	4.99	-30.1			
1580.09	3.61	-29.8			
1580.27	4.53	-30.0			
1580.41			481	3	99
1580.51	4.69	-29.9			
1580.62	6.96	-30.1			
1580.76	7.05	-30.0			
1580.94	9.995	-30.5			
1581.17	3.79	-29.8			
1581.26			478	2	105
1581.33	5.31	-29.9			
1581.52	4.38	-29.9			
1581.71	5.02	-30.0			
1581.85	6.49	-30.4			
1582.10	6.52	-30.1			
1582.23	6.35	-28.5			
1582.42			478	6	95
1582.55	5.1	-29.3			
1583.08	5.73	-29.5			
1583.08	5.87	-29.6			

1583.25			476	5	108
1583.89	4.99	-29.5			
1584.23	5.5	-28.9			
1584.38			475	4	103
1584.58	5.42	-28.9			
1584.95	11.05	-28.9			
1585.28	7.54	-29.1	476	3	101
1585.35	9.63	-29.0			
1585.46	9.92	-29.0			
1585.97			476	3	95
1586.05	10.60	-29.5			
1586.36	9.56	-29.3			
1586.47	9.81	-29.1			
1586.60	10.45	-28.5			
1586.84	11.5	-29.2			
1587.10	5.74	-28.7			
1587.64	7.91	-29.5			
1587.99	6.60	-29.9			
1588.30			469	5	45
1588.47	4.67	-30.0			
1589.25			474	3	125
1589.32	9.44	-30.3			
1589.33	9.74	-30.3			
1589.34	10.2	-29.5			
1589.35	9.57	-30.0			
1589.52	4.11	-28.5			
1589.96	6.05	-30.0			
1590.05			477	6	57
1590.38	10	-30.3			
1591.05	4.88	-29.1			
1591.32			474	5	78
1591.74	6.01	-30.0			
1592.29			479	8	78
1592.37	6.77	-29.8			
1593.14			480	7	82
1593.27	9.57	-30.4			
1593.44	7.66	-30.3			
1594.00	5.64	-30.1			
1594.30			478	6	81
1594.66	6.81	-30.0			
1595.17	7.63	-30.6			
1595.35			481	10	61
1595.51	5.52	-29.5			

Appendix 2: X-ray Diffraction Data

ND = Not Detected (reported as 0)

Depth (m)	Qtz (wt%)	Carb (wt%)	Clay (wt%)	Ap (wt%)	Py (wt%)
1560.51	9.4	ND	87	ND	3.8
1561.60	14	0.50	69	ND	3.9
1562.40	55	1.9	40	ND	2.9
1563.32	59	11	25	ND	ND
1564.67	50	ND	48	ND	ND
1565.46	27	ND	69	ND	2.4
1566.68	28	ND	66	ND	4.2
1567.47	61	ND	34	ND	ND
1568.41	76	6.2	11	ND	ND
1569.47	38	ND	54	ND	1.2
1570.48	54	1.6	37	ND	2.1
1571.66	57	3.3	32	ND	2.5
1572.31	62	0.80	8.9	ND	0.30
1573.31	36	ND	63	ND	ND
1574.30	54	2.8	37	ND	2.4
1575.51	70	30	ND	ND	ND
1576.30	6.7	24	69	ND	ND
1577.66	34	29	37	ND	ND
1578.52	32	34	35	ND	ND
1579.57	39	32	ND	26	ND
1580.42	44	42	6.9	ND	2.6
1581.50	74	16	ND	ND	ND
1582.67	19	31	22	28	ND
1583.50	24	56	ND	20	ND
1584.63	87	7.0	ND	4	ND
1585.53	81	16	ND	ND	ND
1586.22	40	43	16	ND	ND
1587.65	11	31	ND	59	ND
1588.56	12	23	46	ND	4.8
1589.51	87	13	ND	ND	ND
1590.33	44	43	9.2	ND	ND
1591.58	22	75	ND	ND	ND
1592.54	17	83	ND	ND	ND
1593.40	15	85	ND	ND	ND
1594.55	14	58	ND	28	ND
1595.64	16	76	ND	8.3	ND

Appendix 3: Major Element Data

NA = Not Analysed

Depth (m)	Al (wt%)	Ca (wt%)	C_{inorg} (wt%)	P (wt%)	Fe (wt%)	S (wt%)
1560.06	8.1	1.9	0.78	0.04	3.0	3.1
1561.36	6.9	1.2	0.54	0.06	2.5	2.7
1561.91	8.9	1.7	0.32	0.04	2.7	3.1
1562.27	8.9	0.92	0.31	0.03	2.5	2.9
1562.93	6.1	1.2	0.50	0.05	2.1	2.5
1563.90	7.9	1.2	0.28	0.21	2.7	3.0
1564.28	6.4	0.93	0.23	0.11	1.9	2.4
1565.61	5.8	0.50	0.20	0.07	2.1	2.5
1566.37	7.2	0.67	0.29	0.04	2.6	3.2
1567.66	6.9	0.49	0.15	0.04	2.0	2.4
1568.01	8.5	0.57	0.19	0.06	2.3	2.7
1568.60	6.1	0.66	0.21	0.03	2.5	NA
1568.68	12.3	0.39	0.17	0.07	7.5	6.8
1569.77	5.4	1.9	1.0	0.07	1.7	2.5
1570.15	8.6	0.34	0.28	0.04	2.5	3.0
1570.76	5.3	0.78	0.36	0.04	2.0	2.3
1571.33	6.2	0.71	0.22	0.09	2.5	3.0
1571.92	7.8	0.48	0.15	0.05	3.6	4.7
1572.58	4.9	1.4	0.67	0.07	1.8	2.4
1573.31	5.6	0.72	0.24	0.07	1.6	2.3
1574.17	6.7	0.34	0.18	0.04	2.5	2.7
1574.53	7.0	1.0	0.69	0.05	2.5	2.9
1574.85	8.4	1.0	0.31	0.71	7.2	6.2
1575.00	2.7	1.2	0.56	0.04	2.2	3.2
1575.25	5.3	1.2	0.48	0.06	2.4	3.1
1575.35	6.8	1.3	0.60	0.07	2.7	3.1
1575.46	6.2	2.7	1.1	0.08	2.4	2.9
1575.61	7.9	3.8	1.3	0.13	3.4	2.1
1575.82	4.4	4.6	1.6	0.09	1.9	2.5
1575.93	10.1	3.1	1.2	0.10	3.1	3.1
1576.11	3.4	4.9	1.6	0.11	1.7	NA
1576.37	10.6	2.7	1.0	0.16	4.1	3.7
1576.41	4.7	6.7	2.3	0.18	2.6	3.5
1576.59	6.1	3.9	1.3	0.12	2.5	2.9
1576.82	4.5	5.5	1.8	0.12	1.9	NA
1576.91	4.3	8.2	1.9	1.2	1.8	2.3
1577.11	6.2	4.4	1.4	0.36	2.1	2.3
1577.24	4.3	6.4	2.2	0.08	1.8	2.6
1577.36	5.1	6.5	2.3	0.13	2.1	2.7
1577.61	4.0	10	4.4	0.04	1.7	2.1
1577.84	8.5	2.8	1.1	0.14	3.3	2.5
1578.34	7.3	10	3.7	0.22	3.8	1.5

1578.93	4.9	3.4	1.2	0.32	1.7	1.9
1579.06	4.0	6.4	2.0	0.15	1.7	2.1
1579.10	4.6	6.8	2.5	0.31	1.8	2.2
1579.32	4.6	4.0	1.2	0.24	1.7	1.9
1579.61	6.7	5.5	1.5	1.8	2.3	2.0
1579.93	3.5	8.0	1.4	2.0	1.3	1.7
1580.09	5.6	5.0	1.4	0.83	2.0	2.2
1580.27	4.1	7.9	2.8	0.17	2.1	2.6
1580.51	5.0	7.9	1.3	2.2	2.4	3.0
1580.62	2.8	8.2	1.2	1.8	1.1	1.8
1580.76	3.4	5.3	1.2	1.3	1.4	2.3
1580.94	2.6	19	0.21	14.9	2.6	3.0
1581.17	9.9	1.7	0.36	0.58	2.8	3.0
1581.33	4.6	8.7	1.3	4.0	9.3	8.9
1581.52	3.4	8.5	2.2	0.87	2.0	2.4
1581.71	6.1	4.3	1.3	0.73	2.9	3.0
1581.85	2.1	15	3.3	2.5	1.6	2.4
1582.10	2.1	8.3	2.1	1.2	4.9	NA
1582.23	2.8	16	2.0	4.3	1.0	NA
1582.55	4.3	14	2.7	3.2	1.3	1.6
1583.08	2.5	18	4.6	1.3	1.0	NA
1583.08	2.6	23	4.7	2.5	1.0	1.6
1583.89	2.8	18	5.8	0.02	2.0	2.5
1584.23	5.1	14	3.4	0.40	2.4	2.9
1584.58	2.1	10	3.1	0.26	0.70	NA
1584.95	3.6	19	5.6	0.53	2.0	3.3
1585.28	3.6	11	2.7	1.1	2.6	3.3
1585.35	3.4	17	4.5	1.0	1.6	2.7
1585.46	2.6	19	5.7	0.51	1.4	2.5
1586.05	1.9	17	4.8	0.31	1.2	2.6
1586.36	2.6	23	6.0	0.55	1.5	2.4
1586.47	2.2	18	5.5	0.14	1.4	2.5
1586.60	3.6	22	5.5	1.2	1.6	2.3
1586.84	1.5	20	5.9	0.49	0.92	2.3
1587.10	4.2	14	4.1	0.59	1.1	1.7
1587.64	1.0	7.8	2.5	0.20	0.29	1.0
1587.99	1.9	12	3.5	0.22	0.73	NA
1588.47	1.8	18	4.8	0.55	0.69	NA
1589.32	0.91	8.1	2.2	0.66	0.41	NA
1589.33	0.86	7.3	2.3	0.08	0.37	NA
1589.34	1.0	8.3	2.4	0.64	0.41	1.3
1589.35	1.1	8.8	2.7	0.29	0.46	NA
1589.52	3.5	15	4.9	0.38	1.8	2.4
1589.96	2.3	20	4.1	3.0	1.0	2.2
1590.38	0.65	7.7	2.4	0.10	0.28	1.3
1591.05	2.6	17	5.0	0.50	1.1	1.6
1591.74	1.7	20	6.3	0.25	0.95	1.8

1592.37	1.6	27	7.2	0.58	0.92	1.7
1593.27	1.2	27	6.8	0.19	0.65	1.3
1593.44	1.7	27	7.8	0.36	0.80	1.4
1594.00	1.9	17	5.3	0.48	0.91	NA
1594.66	2.1	25	6.5	3.7	1.2	1.5
1595.17	1.5	14	4.4	0.18	0.62	1.5
1595.51	3.4	14	4.0	0.67	1.1	1.8

Appendix 4: Trace Metal Data

NA = Not Analysed

Depth (m)	Mo (µg/g)	V (µg/g)	U (µg/g)	Re (ng/g)	Cd (µg/g)	Hg (ng/g)
1560.06	8.9	133	4.4	41	0.64	113
1561.36	9.3	183	3.2	70	1.5	114
1561.91	19	341	3.5	152	4.6	136
1562.27	17	380	2.8	125	2.6	118
1562.93	40	470	6.6	236	17	132
1563.90	18	477	13	159	2.2	187
1564.28	40	606	7.4	291	21	184
1565.61	12	168	2.6	49	1.3	146
1566.37	15	228	4.2	83	1.7	210
1567.66	8.9	156	3.2	47	0.93	145
1568.01	16	370	6.3	86	2.7	128
1568.60	11	186	3.6	65	1.4	221
1568.68	21	248	5.0	28	1.8	555
1569.77	7.0	165	7.2	57	0.91	155
1570.15	11	209	2.6	116	1.7	159
1570.76	33	487	5.2	313	51	163
1571.33	7.8	142	5.7	96	0.66	183
1571.92	12	343	3.4	33	1.5	340
1572.58	4.3	149	3.9	34	0.39	119
1573.31	7.8	221	5.0	119	1.5	118
1574.17	11	258	4.8	96	2.0	130
1574.53	52	728	9.3	456	91	228
1574.85	26	455	12	41	1.0	271
1575.00	115	447	6.7	257	12	114
1575.25	108	931	7.3	220	24	139
1575.35	108	1191	9.3	261	22	143
1575.46	104	1169	18	225	14	144
1575.61	137	1684	18	220	13	152
1575.82	86	884	15	283	17	91
1575.93	76	1533	10	201	14	125
1576.11	111	929	17	275	22	104
1576.37	166	2166	14	458	32	194
1576.41	108	1100	18	280	32	154
1576.59	102	1210	16	307	21	134
1576.82	54	912	10	184	19	122
1576.91	48	950	17	196	28	135
1577.11	30	609	9.1	166	3.0	120
1577.24	48	940	7.4	169	39	152
1577.36	51	1014	9.3	204	38	164
1577.61	29	575	5.2	111	6.6	135
1577.84	73	1527	10	428	39	149
1578.34	103	1112	28	878	9.2	164

1578.93	14	199	5.2	124	1.6	138
1579.06	33	381	6.7	245	8.9	138
1579.10	29	392	7.1	288	7.9	142
1579.32	10	201	5.0	99	1.3	139
1579.61	14	262	8.8	108	1.4	132
1579.93	12	257	11	140	8.2	117
1580.09	15	387	10	111	1.8	133
1580.27	44	461	12	373	16	160
1580.51	33	624	18	239	4.4	169
1580.62	15	331	9.4	96	5.9	102
1580.76	16	222	9.1	188	2.8	127
1580.94	36	199	33	190	2.4	117
1581.17	18	708	13	144	3.1	201
1581.33	53	289	29	287	2.8	566
1581.52	27	228	14	268	3.3	114
1581.71	10	232	13	73	1.4	228
1581.85	12	100	19	152	1.0	135
1582.10	3.9	78	6.8	83	0.39	82
1582.23	7.3	118	10	119	0.9	77
1582.55	18	178	17	189	2.3	94
1583.08	30	199	11	180	3.7	100
1583.08	25	219	10	190	3.7	85
1583.89	12	100	4.5	61	0.90	247
1584.23	40	104	11	123	1.8	NA
1584.58	14	76	4.4	41	1.2	NA
1584.95	295	1282	25	146	45	235
1585.28	370	1984	36	241	40	270
1585.35	128	846	22	126	6.2	119
1585.46	189	1152	25	155	21	158
1586.05	268	1415	23	211	40	202
1586.36	231	1049	20	160	23	149
1586.47	267	1168	20	353	26	171
1586.60	87	626	13	236	5.3	108
1586.84	247	1054	24	210	18	139
1587.10	199	2237	14	238	19	103
1587.64	21	262	3.5	54	1.3	26
1587.99	59	540	7.2	90	8.5	104
1588.47	127	864	14	21	26	97
1589.32	76	481	10	149	16	NA
1589.33	64	454	4.1	140	15	NA
1589.34	64	508	10	133	13	70
1589.35	82	540	7.3	176	17	86
1589.52	292	2262	21	364	55	236
1589.96	76	718	34	142	10	132
1590.38	70	671	5.8	110	17	60
1591.05	177	988	19	303	39	191
1591.74	321	2188	27	390	45	149

1592.37	216	1591	36	261	32	139
1593.27	186	1168	25	201	11	79
1593.44	289	2757	27	267	33	130
1594.00	122	1322	16	195	32	132
1594.66	115	1295	19	239	8.7	115
1595.17	217	1182	11	212	35	119
1595.51	205	1128	19	325	50	201